

NONLINEAR TRANSMISSION STUDIES IN GLASSES  
AND SEMICONDUCTORS OF THERMAL  
AND ELECTRONIC ORIGIN

By

WARREN DOYLE ST. JOHN

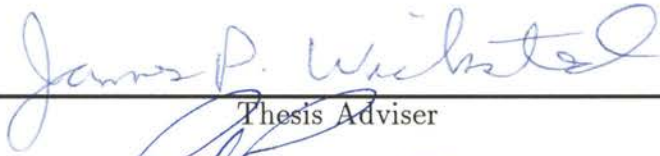
Bachelor of Science  
Tulsa University  
Tulsa, Oklahoma  
1986

Master of Science  
Oklahoma State University  
Stillwater, Oklahoma  
1988

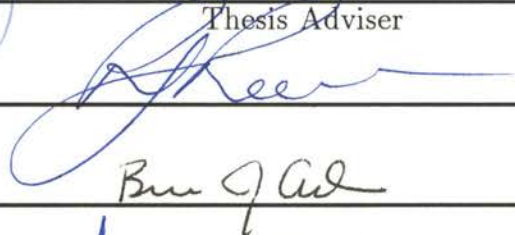
Submitted to the Faculty of the  
Graduate College of the  
Oklahoma State University  
in partial fulfillment of  
the requirements for  
the Degree of  
DOCTOR OF PHILOSOPHY  
May, 1993

NONLINEAR TRANSMISSION STUDIES IN GLASSES  
AND SEMICONDUCTORS OF THERMAL  
AND ELECTRONIC ORIGIN

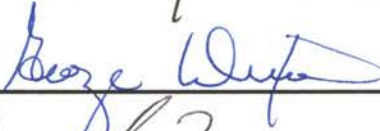
Thesis Approved:

  
\_\_\_\_\_

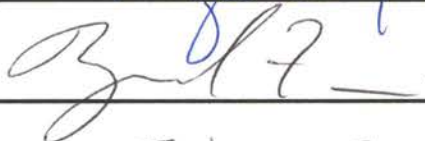
Thesis Adviser

  
\_\_\_\_\_

Bill Keen

  
\_\_\_\_\_

George W. Winters

  
\_\_\_\_\_

  
\_\_\_\_\_

Dean of the Graduate College

## ACKNOWLEDGEMENTS

I wish to endorse a great many individual of whom either taught, bolstered, amused, confused, or otherwise inspired me over the years. As this acknowledgment should not be a chapter in itself I have refined the list and sincerely hope those not mentioned realize it is only by necessity.

I am certainly indebted to my principle advisor Dr. James P. Wicksted. Dr. Wicksted began as my "advisor" and is now in addition my mentor and friend. I would also like to thank Carol Wicksted for her always supportive and helpful demeanor.

I have benefited immensely from a number of wonderful teachers. I would like to particularly recognize Dr. Larry Scott, Dr. Paul Westhaus, Dr. Dixon, and Dr. Nandi. Although at times I felt their tactics cruel their foresight is certainly impeccable. Although never a formal instructor I wish to thank Dr. Bruce Ackerson for his always helpful and sincere guidance. I would also like to thank Dr. Richard Powell for his generous, fruitful, and experienced insight. Consistent with that I would like to thank Dr. Roger Reeves for suitably replacing Dr. Powell, upon his departure, on my graduate committee. Finally I would like to thank Dr. Ray Zanoni for serving on my committee.

I would also like to thank the myriad of fellow students of whom I shared some form of working environment with over the years for tolerating my sometimes erratic and always impatient nature. The medley of personalities, cultures, and wit of these characters has always brewed a rich and pleasant atmosphere.

Additionally I am grateful to my family. If there was ever anybody of whom instilled confidence and spirituality in myself, well I have to blame it on Mumz, Dad, Mike, Tad, and Kevin.

I would also like to thank my old nutty friend John Kosir. The many demented and always odd adventures we have shared have always raised my spirit and questioned my character.

Lastly I acknowledge my four oldest and dearest comrades, Mr. Iommi, Mr. Butler, Mr. Ward, and Mr. Osbourne.

## TABLE OF CONTENTS

Chapter	Page
I. INTRODUCTION . . . . .	1
II. OPTICAL BISTABILITY IN BULK ZnSe . . . . .	4
Introduction . . . . .	4
Experiment . . . . .	7
Theory I . . . . .	9
Theory II.A. . . . .	11
Introduction . . . . .	11
Solution to Internal Fields . . . . .	13
Propagation of External Fields . . . . .	17
Finite Difference Schemes . . . . .	19
Stability of Numerical Schemes . . . . .	21
Conclusion . . . . .	28
Theory II.B. . . . .	28
Results and Discussion . . . . .	40
Absorptive Switching . . . . .	40
Transverse Structures . . . . .	44
Regenerative Pulsations . . . . .	50
Conclusion . . . . .	58
III. THERMAL LENSING IN A LEAD SILICATE GLASS . . . . .	66
Introduction . . . . .	66
Thermo-optic Effect . . . . .	67
Gaussian Beams in Quadratic Index Media . . . . .	70
Experiment . . . . .	71
Results and Discussion . . . . .	73
Conclusion . . . . .	78
IV. NONLINEAR TRANSMISSION IN CdS . . . . .	84
Introduction . . . . .	84
Experiment . . . . .	84
Theory . . . . .	86
Results and Discussion . . . . .	89

Chapter	Page
Conclusion . . . . .	95
V. SUMMARY AND FUTURE WORK . . . . .	97
BIBLIOGRAPHY . . . . .	102
APPENDIX . . . . .	107
A - PROGRAM FOR THEORY II.A., CHAPTER II . . . . .	108
B - PROGRAM FOR THEORY II.B., CHAPTER II . . . . .	114

## LIST OF FIGURES

Figure	Page
1. Optical Bistability Hysteresis Curve . . . . .	5
2. Experimental Arrangement for Optical Bistability in ZnSe . . . . .	8
3. Absorption Spectra for ZnSe as a Function of Temperature. . . . .	12
4. Absorption Spectra for ZnSe as a Function of Temperature and a Theoretical Fit Using a Quantum Mechanical Model . . . . .	34
5. Index of Refraction Spectra for ZnSe as a Function of Tem- perature and the Resonant Enhancement of the Refractive Index at 476.5nm . . . . .	35
6. Theoretical Absorption Spectra for ZnSe as a Function of e-h Density .	36
7. Index of Refraction Spectra for ZnSe as a Function of e-h Den- sity and the Resonant Enhancement of the Refractive Index at 476.5nm . . . . .	38
8. 3-d View of the Absorption Spectra for ZnSe as a Function of Temperature and e-h Density at 476.5nm . . . . .	39
9. Absorptive Switching in ZnSe . . . . .	41
10. Absorptive Switching Characteristics in ZnSe as a Function of Key Parameters . . . . .	42
11. Time of Switching as a Function of Input Power . . . . .	45
12. Output Beam Profiles During Switching . . . . .	46
13. Comparison of Experimental and Theoretical Beam Profiles . . . . .	48
14. Intensity Profile Throughout the Bulk as a Function of Transmittivity	49
15. Temperature Profile Throughout the Bulk as a Function of Transmittivity . . . . .	51

Figure	Page
16. e-h Density Profile Throughout the Bulk as a Function of Transmittivity	52
17. Transmission and Reflection Showing (Absorptive) Regenerative Pulsations . . . . .	54
18. Example Cases of Experimental Regenerative Pulsations Illustrating the Near Square Top and Sawtooth Type Structures . . . . .	55
19. Example of Regenerative Pulsations Using a 3.5cm Focal Length Lens . . . . .	60
20. Comparison of Experimental and Theoretical Regenerative Pulsations .	61
21. (Radial) Intensity Profile at the Surface as a Function of Time . . . . .	62
22. (Radial) Temperature Profile as the Surface as a Function of Time . .	63
23. (Radial) e-h Density Profile at the Surface as a Function of Time . . .	64
24. Results of Side Beam Experiment . . . . .	65
25. Temporal Profile of YAG Laser Pulse . . . . .	69
26. Experimental Arrangement for Thermal Lensing in a Lead Silicate Glass . . . . .	72
27. Millisecond Temporal Results . . . . .	80
28. Z-scan and Transmission Results . . . . .	81
29. Theoretical Z-scans and Beam Undulations . . . . .	82
30. Results of Nanosecond Experiments . . . . .	83
31. Experimental Arrangement for Transmission Studies in CdS . . . . .	85
32. Experimental Transmission Profiles in CdS . . . . .	90
33. Theoretical Transmission Profiles in CdS . . . . .	91
34. Absorption Spectra for CdS as a Function of Temperature . . . . .	93
35. Theoretical Refractive Index Spectra for CdS as a Function of Temperature . . . . .	94



# CHAPTER I

## INTRODUCTION

The principle aim of this research has been to characterize and investigate the nonlinear optical behavior of various semiconductors and modified silicate glasses. These materials possess particularly interesting as well as potentially exploitable optical properties and as such have recently attracted a great deal of attention from both a pure research standpoint as well as the basis for new device technologies. Because of this potential for practical applications it is necessary that their properties be thoroughly examined so as to quantify their nature and limits of operation.

Because our goal has been to research the optical properties of various materials, the principle method of experiment relies on optical sources (lasers), related optical measurement devices (spectrographs, detectors, ect.), and the associative electronics. Once the experimental findings have been identified, a theory is originated to hopefully explain these findings, and finally the theory is simulated by computer modeling.

This work is divided into three parts covering three separate projects. Each component stands on its own and has little relation to its neighbors. As such there is little importance as to the organization of these respective chapters, thus arbitrarily they have been arranged in reverse chronological order.

An important and exciting technology beginning to realize itself is that of optical computing. Here the goal is to replace all existing electronic components with an optical analog. The benefits of such a leap are immense; an increase in computational speed and bandwidth in orders of magnitude. A key component in this technology is the switch. Specifically one requires a stable and fast all optical bistable device capable of residing in two optically unique states. This is the

subject matter of optical bistability and is a huge field in itself. In Chapter II we investigate the bistable behavior in bulk ZnSe. The form of bistability is resonatorless absorptive bistability. Here the feedback mechanism stimulating the bistable property occurs through a temperature dependent absorption and an absorption dependent temperature mediated by a temperature dependent band gap. We use a relatively simple single beam transmission type geometry. The transmitted and reflected power are monitored on a microsecond to  $\sim$  CW time scale. In addition we have measured beam profiles. In most cases we see an eventual switching to an off-state (one of low transmission) and subsequent damage. However in some samples a rare form of bistable behavior, regenerative pulsations, has been identified and a possible explanation, including simulation, has been put forth. This phenomenon seems to be very rare as only a few other authors have reported on such findings however without any quantitative explanation. We have made such an analysis and hope that this reveals new insight into optical switching, thermal wave motion, and the role of electronic/thermal surface effects on the bistable behavior of semiconductors. As this phenomenon is seemingly rare it is likely our understanding has only begun. Many questions still exist and the possibility of controlling and stabilizing this effect is certainly an intriguing one.

In addition to such phenomenon as optical bistability there has been a huge push for all optical limiting devices. This is essentially the optical analog of the zener diode, a voltage clamping device. This was the motivation for the work presented in Chapter III. In particular we characterize the thermal lensing behavior of a lead oxide modified silicate glass. We report on such measurements as the popular Z-scan and optical limiting scans. We carry out these measurements on both a millisecond and nanosecond time scale. On a millisecond time scale beam undulations have been experimentally and theoretically seen to manifest themselves in a new way (i.e. via Z-scans).

Lastly we report on the transmission characteristics in bulk CdS (Chapter IV). This project was originally initiated as an investigation of the thermo-optic character of CdS on a long time scale (seconds). We use a relatively simple two

beam (pump-probe) transmission type geometry. The results indicate the presence of thermal lensing and interference (Fabry-Perot) effects.

Finally we summarize all of our results and offer suggestions for future work.

## CHAPTER II

### OPTICAL BISTABILITY IN BULK ZnSe

#### Introduction

Optical bistability has received a great deal of interest because of its potential for all-optical logic elements as well as being a fundamentally interesting phenomenon. A common definition of optical bistability is offered by Figure 1. A system having such a transmission curve is said to be optically bistable between the light intensities  $i_{\downarrow}$  and  $i_{\uparrow}$ . This definition of bistability is restricted in that the hysteresis is controlled by the light intensity, as opposed to some other parameter. It may be that the hysteresis is a function of, for example, temperature, but the temperature is a function of the light intensity. Such feedback is an inherent property of all bistable systems. Optical bistable systems are generally classified as dispersive or absorptive and intrinsic or hybrid. A bistable system is dispersive if the feedback results from an intensity dependent refractive index (light interference), while absorptive bistability occurs when the feedback is supplied by an intensity dependent absorption. It may be that both mechanisms are present in a given system thus this distinction is not always clear. Intrinsic systems possess some feedback mechanism which is completely controlled by the light intensity. These systems rely strictly on the light-matter interaction. Because this form of bistability is intrinsic this can result from a single pass of the light beam through the system, that is it does not require any interference. Such systems have been referred to in the literature as mirrorless, cavityless, or resonatorless. (We will use the latter name.) Hybrid systems rely on some form of external electronics as the feedback mechanism. These systems sample the output light intensity and then

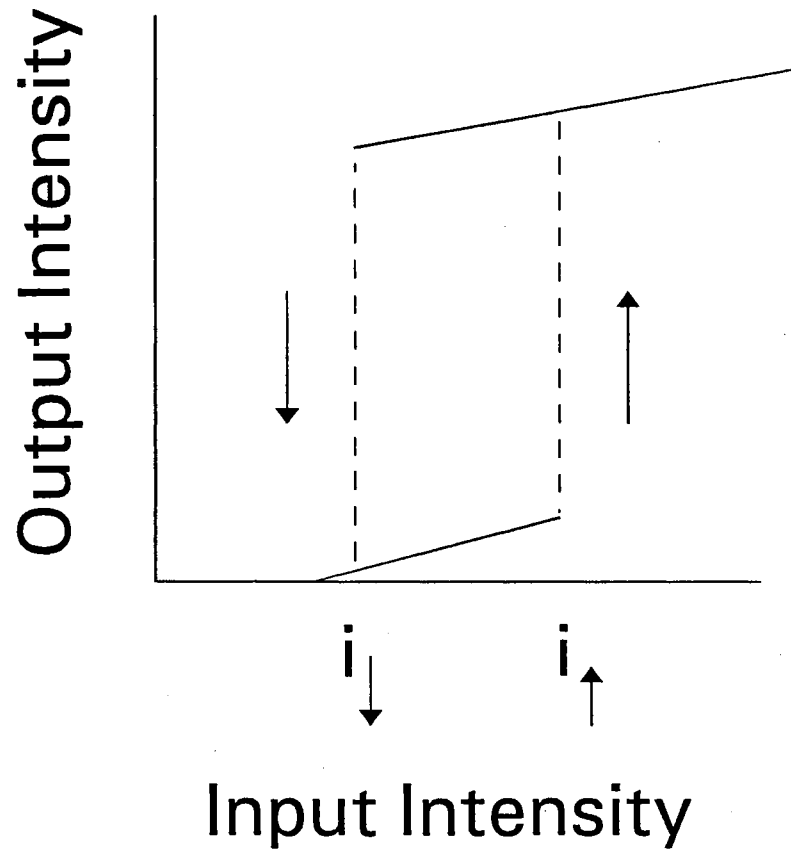


Figure 1. Optical bistability hysteresis curve.

adjust some external parameter, for example the strength of an applied electric field, which changes the material properties.

The form of bistability of interest here is resonatorless absorptive bistability. Such bistability may result from the thermal properties of the band gap[1–3] or the various effects resulting from the creation of an electron-hole plasma such as band filling, plasma screening, or resonance broadening[4–7]. This form of bistability has been investigated by numerous workers (see H. M. Gibbs[8] (1985) for an extensive review). As a result of increasing absorptive bistability, such phenomenon as kinks in the transmitted power have been observed[9] and the formation and motion of high absorption domains[10–14]. In addition to the bistable switching, transverse effects become important due to the non-plane wave nature of any excitation source. Such beam distortions resulting from increasing absorptive bistability may form rings in the intensity profile[8,15].

In this chapter we present theoretical and experimental results of absorptive switching, the formation of transverse structures, and regenerative pulsations in 1mm thick samples of ZnSe at room temperature. The first part discusses the results of absorptive switching. Here, with a constant input, the sample switches to an off-state and subsequently damages. The off-state implies that the transmission has dropped to less than a few percent of the maximum. Here we show the results of switching on a time scale spanning microseconds to seconds. In addition we show theoretical simulations showing the effect of various parameters, such as sample thickness or ambipolar diffusion, on the switching characteristics. In the second part we discuss transverse structures. Here we show theoretical and experimental beam profiles. At low input intensities, when the time for switching is on the order of  $\sim 1$ sec, we observe through computer simulation that during switching either longitudinal or transverse heat diffusion allows the formation of a local minima on axis (hole). However heat diffusion in all three dimensions is necessary for the further development of a local maxima on axis with a local minima off axis (rings). At higher input intensities more complex transverse structures result whereby multiple rings may be identified. In all cases such beam distortions

resemble switching waves[16]. Lastly we discuss regenerative pulsations. Here instead of immediately damaging upon switching to the off-state the transmission will pulse, meaning the output will repeatedly switch between an off-state and an on-state. The off-state is typically less than 5% the maximum while the on-state ranges from ~ 30%-80% the maximum. We will show a variety of example output along with our theoretical results, including beam profiles. Our theory of this phenomenon is essentially identical to that concerning the absorptive switching alone however with the further stipulation that the thermal conductivity be enhanced at the surface. We note that this phenomenon seems extremely rare as few authors have reported on such results.

As a final comment, the theory section has been divided into three parts. The first part, Theory I, is essentially a succinct version of the much more detailed version in Theory II.A. and Theory II.B.. Much of Theory II.A. is an analysis of the numerical technique employed in solving a system of couple partial differential equations (PDE's). Section Theory II.B. is a quantum mechanical theory for the absorption spectra and the effects of temperature and electron-hole density. Thus the detail of Theory II.A. and Theory II.B. is not essential to understanding the model and thus Theory I was included merely as a convenience to the reader.

## Experiment

Our experiment consists of a very simple transmission type geometry (see Figure 2). We use the 476.5nm output of a CW Ar<sup>+</sup>-ion laser operating in the TEM<sub>00</sub> mode. The light is switched on (and at some time later, switched off) via an acousto-optic modulator (AOM) and focused along the optical axis on to the front face of the sample using a 5cm focal length lens, L1 (although later we give an example of regenerative pulsations using a 3.5cm lens). All the transmitted light is collected. We use a beam splitter prior to the focusing lens to measure the reflection off the front face. Additionally we focus a 543.5nm HeNe laser through the sides of the sample such that the two beams cross in the interior. The results of three types of experiments are discussed. 1) The total transmitted power as a

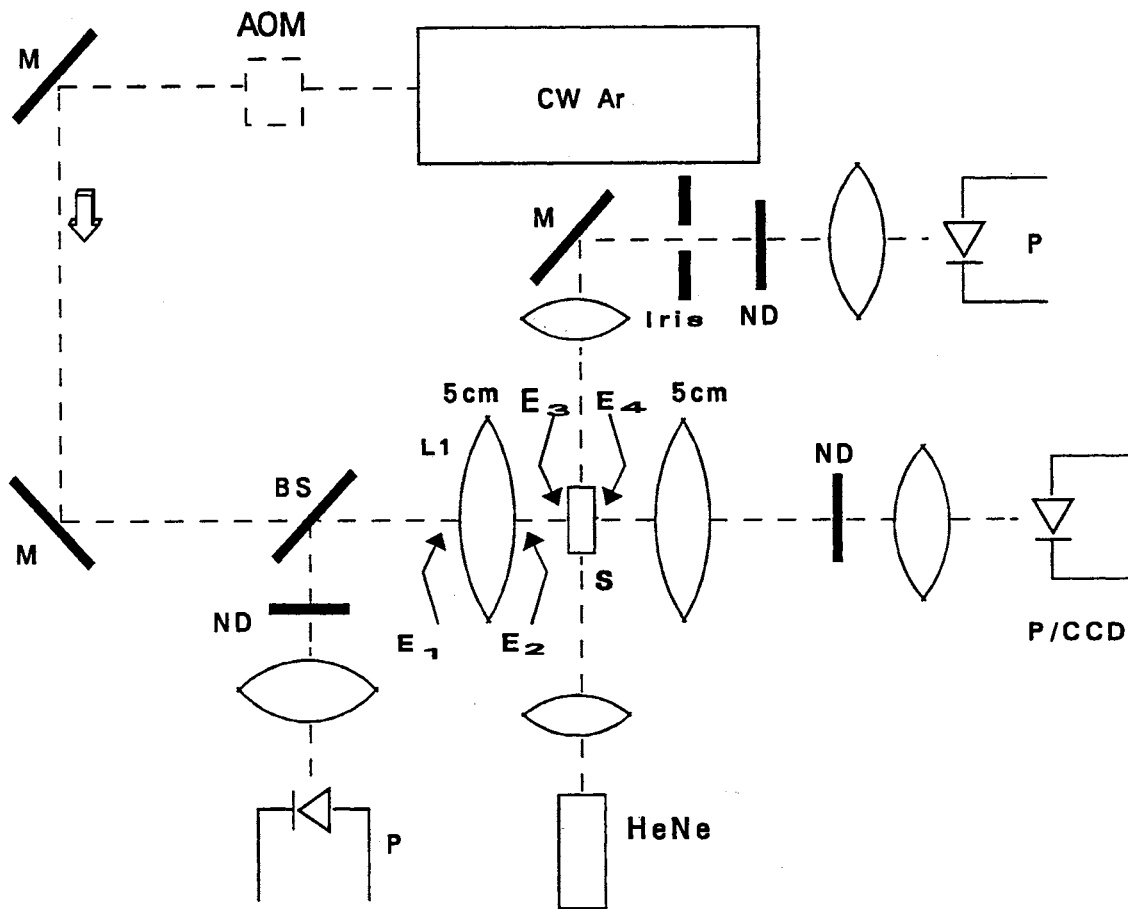


Figure 2. Experimental arrangement for optical bistability in ZnSe. AOM-acousto-optic-modulator, M-mirror, ND-neutral density filter, BS-beam splitter, P-photodiode, L1-focusing lens, CCD-charge coupled device. E1, E2, E3, and E4 refer to the electric field at the indicated regions.



function of time. Here detection is accomplished via a fast photodiode and digital storage oscilloscope. 2) Beam profiles. Here a 120x120 pixel CCD array and beam profiler are used in place of the photodiode (in the case of the transmitted light). 3) Side beam experiment. We monitor the transmission of the side (HeNe) beam beyond an iris simultaneously with the Ar<sup>+</sup>-ion beam. The labels E<sub>1</sub>-E<sub>4</sub> identify the electric fields at the respective locations. These are simply convenient markers for the discussion of section Theory II.A..

## Theory I

In this section we offer a succinct version of the more detailed outline of Theory II.A. and Theory II.B. The purpose of this section is to establish the basic idea of the theory so that one may understand our approach to the problem and move on to the results and discussion section, and then if interested seek the more detailed version of the theory afterwards. This is merely offered as a matter of convenience as it makes this chapter somewhat more readable.

We know from an analysis of the transmission and reflection as a function of time that the solution to the problem lies in finding the absorption coefficient in space and time. The time scale of the results is conducive to a thermal effect. We also know the band gap is temperature dependent. In addition we know the temperature change results from the radiationless relaxation of induced electron-hole pairs, of which are a function of the light intensity and the absorption. Thus the problem is modeled as a thermal and e-h density transport process coupled with a light diffraction process. Thus the governing equations are the wave equation for the electric field, heat flow equation for the temperature, and rate equation for the e-h density. We prefer to know these quantities in three dimensions (or four including time). Due to the high nonlinearity of our system and the preference for multidimensionality, we have sought a numerical solution.

The wave equation is,

$$\nabla^2 E + k_0^2 n^2 E = 0 \tag{1}$$

where  $E$  is the complex electric field strength,  $k_o$  the wavevector in vacuum, and  $n$  the complex refractive index. The heat flow equation is,

$$\frac{1}{\eta_{th}} \frac{\partial T}{\partial t} = \nabla^2 T + q_{eff} \frac{N \hbar \omega}{\tau k_{th}} \quad (2)$$

where  $T$  is the temperature,  $\eta_{th}$  is the thermal diffusivity,  $k_{th}$  the thermal conductivity,  $q_{eff}$  the percent of e-h recombination events which are radiationless,  $N$  the e-h density,  $\hbar\omega$  the photon energy, and  $\tau$  the e-h pair recombination time. Finally the rate equation for the e-h density is given by,

$$\frac{\partial N}{\partial t} = D_a \nabla^2 N - \frac{N}{\tau} + \frac{\alpha I}{\hbar \omega} \quad (3)$$

where  $D_a$  is the ambipolar diffusion coefficient,  $\alpha$  the coefficient of linear absorption, and  $I$  the light intensity. Again, Eq.1, Eq.2, and Eq.3 will be solved numerically. This is the content of section Theory II.A..

The following values for ZnSe have been used:  $D_a = 10^{-4} \text{m}^2 \text{sec}^{-1}$  [17],  $\tau = 10 \text{ns}$  [17],  $k_{th} = 6.3 \text{Wm}^{-1} \text{K}^{-1}$  [18],  $\eta_{th} = 10^{-5} \text{m}^2 \text{sec}^{-1}$  [11], and  $q_{eff} = 1$ .

In Eq.1 the refractive index is written as,

$$n = n_o + \delta n = n_o + \Delta n - i \frac{\alpha}{2k_o} \quad (4)$$

where  $n_o$  is the background dielectric constant and  $\Delta n$  is given by,

$$\Delta n = \left( \frac{\partial n}{\partial T} \right)_{off} \Delta T + (\Delta n)_{on} \quad (5)$$

The *off* term is a background (off-resonant) change in the index of refraction due to a change in temperature while the *on* term is a resonant enhancement due to changes in the band gap (and is a function of temperature). The *off* term was used as a fitting parameter while the *on* term was determined by a kramers-Kronig transformation of the absorption spectra as a function of temperature. The *on* term is determined in section Theory II.B. and is given by,

$$(\Delta n)_{on} = \left[ 1.546 - \frac{2.571}{\cosh \left( \frac{\Delta T - 36.79}{32.45} \right)} \right] \times 10^{-3} \quad (6)$$

The expression for the absorption coefficient found in Theory II.B. could not be used for the simulation when solving these equations. It was only used for calculating the absorption spectra, of which was only used to identify the above on-resonant contribution to the change in the refractive index. The reason for not using that expression is simply because the computational effort would have slowed the program run time from, for example, five minutes to five weeks. Thus in solving the above equations we have used the simple closed form expression known as Urbach's rule for the absorption coefficient. The expression is,

$$\alpha = \alpha_o \exp \left[ \frac{\sigma}{k_B T} \left( \hbar\omega + E_x - E_{g_o} - \frac{\partial E_g}{\partial T} \Delta T \right) \right] \quad (7)$$

where  $\alpha_o = 293/m$ ,  $\sigma = 2.108$ ,  $E_x = 64\text{meV}$ ,  $E_{g_o} = 2.67\text{ev}$  (energy gap at room temperature),  $\partial E_g/\partial T = -.85\text{meV/K}$ , and  $k_B$  is Boltzmann's constant. The constants  $\alpha_o$ ,  $\sigma$ ,  $E_x$ , and  $\partial E_g/\partial T$  were essentially used as fitting parameters however we attempted to find values consistent with literature values[19]. In Figure 3 we show the temperature dependent absorption spectra and the theoretical fit.

## Theory II.A.

### Introduction

As discussed in Theory I the essential problem of our model is to solve the three governing equations, namely the wave equation, heat flow equation, and electron-hole density, or rate equation. The difficulty of this task is that these equations are all coupled, nonlinear, and multidimensional. One could relax some of these requirements (e.g. the number of dimensions) but with a proper numerical scheme such restrictions are unnecessary. We have sought a very general multi-dimensional solution whereby few approximations are invoked. This numerical procedure is however only applied to the contents of this chapter. In later chapters, where similar transmission type studies are undertaken, the nature of the experiment was such that either the time scale was too great and/or the spatial extent (computational grid size) was such that this technique was computationally inefficient.

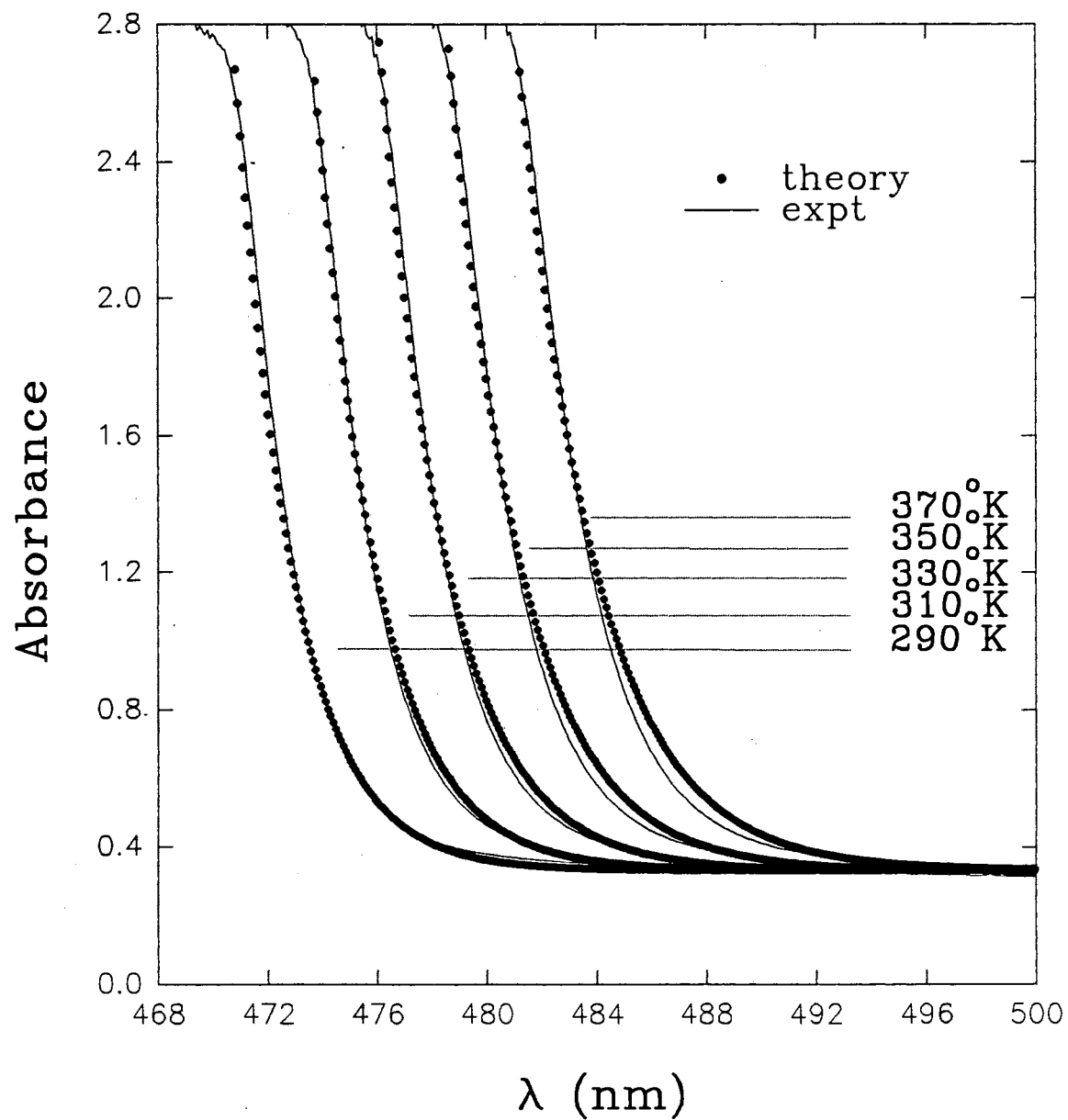


Figure 3. Absorption spectra for ZnSe. The filled circles are theoretical fit using Urbach's rule while the solid lines are experimental data.

In what follows we first outline our solution to the wave equation inside the sample (internal fields). This will give an expression for the real and imaginary part of the electric field of which must be solved numerically. Such a numerical technique is then used to propagate this field from immediately within the front face of the sample to immediately beyond the back interface. Next we show how to find the fields external to the sample (external fields). This essentially begins with a gaussian TEM<sub>00</sub> incident beam of which is focused into the sample. The third section discusses the numerical scheme which is used to solve the three governing equations. Finally we derive some stability conditions for the numerical approximations.

### Solution to Internal Fields

Beginning with Maxwell's Equations and invoking the following approximations: 1) zero free volumetric charge, 2) linear polarization, and 3)  $\omega E \gg \frac{\partial E}{\partial t}$  (slowly varying envelope approximation), we arrive at the scalar Helmholtz Equation,

$$\frac{\partial^2 E}{\partial x^2} + \frac{\partial^2 E}{\partial y^2} + \frac{\partial^2 E}{\partial z^2} + k_o^2 n^2 E = 0 \quad (8)$$

where  $k_o = \omega/c$ ,  $\omega$  is the radiation frequency,  $c$  is the speed of light in a vacuum,  $n = n_o + \delta n$ ,  $n_o$  is the linear index of refraction and  $\delta n$  is the complex nonlinear component of the index of refraction. In this particular application of the Helmholtz equation  $\delta n$  is coupled to the heat flow equation and thus depends on three spatial variables as well as time. Thus a numerical technique is used to propagate the fields. A variety of solution techniques have been attempted. The following technique, which proved to be most accurate in our computational model, is as follows.

The method of solution for the scalar Helmholtz equation for some arbitrary  $\delta n$  follows that of the split-operator scheme[20,21] for solving the paraxial equation but then rather than invoking a fast Fourier transform technique[22-24], a common approach, we use a simple explicit finite difference technique. The following

operators are introduced,

$$P = \frac{\partial}{\partial z} \quad (9)$$

$$Q = (\nabla_{\perp}^2 + k_o^2 n^2)^{\frac{1}{2}}, \quad (10)$$

where  $\nabla_{\perp}^2 = \frac{\partial^2}{\partial x^2} + \frac{\partial^2}{\partial y^2}$ . Eq.8 may now be written as,

$$(P^2 + Q^2)E = 0, \quad (11)$$

which can further be written as,

$$\{(P + iQ)(P - iQ) + i[P, Q]\}E = 0, \quad (12)$$

where  $[P, Q] = PQ - QP$ . If  $[P, Q] = 0$ , then Eq.12 has the solutions,

$$\frac{\partial E}{\partial z} = \pm iQE. \quad (13)$$

The approximation  $[P, Q] = 0$  is good if the variation in  $\delta n$  along the z-axis is sufficiently weak. The solution to Eq.13 represents a wave propagating along the z-axis. For a wave propagating in the positive z-direction over some small z increment,  $\Delta z$ , is,

$$E(x, y, \Delta z) = \exp \left[ -i \int_0^{\Delta z} (\nabla_{\perp}^2 + k_o^2 n^2)^{\frac{1}{2}} dz \right] E(x, y, 0). \quad (14)$$

For  $\Delta z$  sufficiently small and the fluctuation in  $\delta n$  along the z-axis sufficiently weak, the integral in Eq.14 may be approximated and Eq.14 becomes,

$$E(x, y, \Delta z) = \exp \left[ -i \Delta z (\nabla_{\perp}^2 + k_o^2 n^2)^{\frac{1}{2}} \right] E(x, y, 0). \quad (15)$$

We now use the following "trick" to rewrite the expression  $(\nabla_{\perp}^2 + k_o^2 n^2)^{\frac{1}{2}}$  which operates on  $E(x, y, 0)$ . We make the following substitution,

$$A^2 = \nabla_{\perp}^2 + k_o^2 n^2 = \nabla_{\perp}^2 + k_o^2 n_o^2 \left(1 + \frac{\delta n}{n_o}\right)^2. \quad (16)$$

Now, we wish to replace  $A$  with the approximation,

$$A_1 = (\nabla_{\perp}^2 + k_o^2 n_o^2)^{\frac{1}{2}} + k_o \delta n. \quad (17)$$

We may test this approximation by operating on  $E(x, y, 0)$  with both  $A^2$  and  $A_1^2$  and comparing. First we express  $E(x, y, 0)$  in a 2-dimensional Fourier series,

$$E(x, y, 0) = \sum_m \sum_n E_{mn}(0) e^{i(k_x x + k_y y) n_o}. \quad (18)$$

Operating on  $E(x, y, 0)$  by  $A^2$  is equivalent to rewriting  $A^2$  as,

$$A^2 = -(k_x^2 + k_y^2) n_o^2 + k_o^2 n_o^2 \left( 1 + \frac{\delta n}{n_o} \right)^2. \quad (19)$$

For the operator  $A_1$  we first square and then use the expansion

$$\left( \nabla_{\perp}^2 + k_o^2 n_o^2 \right)^{\frac{1}{2}} = k_o n_o \left( 1 + \frac{\nabla_{\perp}^2}{2k_o^2 n_o^2} - \frac{\nabla_{\perp}^4}{8k_o^4 n_o^4} + \dots \right) \quad (20)$$

giving,

$$A_1^2 = -(k_x^2 + k_y^2) n_o^2 \left( 1 + \frac{\delta n}{n_o} - \frac{(k_x^2 + k_y^2) \delta n}{k_o^2 4n_o} + \dots \right) + k_o^2 n_o^2 \left( 1 + \frac{\delta n}{n_o} \right)^2 \quad (21)$$

where (...) signifies the higher order terms in the expansion given by Eq.20 We thus see that as long as  $\frac{\delta n}{n_o} \ll 1$  the replacement of  $A$  by  $A_1$  is justified. Note, for  $k_z$  real, that is a propagating field,  $k_x^2 + k_y^2 < k_o^2$ . Our solution for the electric field at  $z = \Delta z$  becomes,

$$E(x, y, \Delta z) = e^{-i\Delta z (\nabla_{\perp}^2 + k_o^2 n_o^2)^{\frac{1}{2}}} E(x, y, 0) e^{-i\Delta z k_o \delta n}. \quad (22)$$

This final form states that the solution is given by propagating the field through the linear medium ( $\delta n = 0$ ) and then updating the phase by the nonlinearity,  $-\Delta z k_o \delta n$ . Computationally this is very significant.

The remaining portion of this development is then to decide how to propagate the fields through the linear medium. It was found, essentially by trial and error, that a straight forward explicit finite difference technique worked best. Other methods, such as the fast Fourier transform technique, implicit methods, ect. were attempted, however they were either too computationally time consuming, required too much memory storage, or simply were numerically inaccurate. Recall that the equation for the electric field is coupled with either the rate equation for the electron-hole density, the heat flow equation, or both. Thus the implicit schemes which may otherwise be preferred, in this system are not.

Eq.22 is rewritten as,

$$E(x, y, \Delta z) = E^o(x, y, \Delta z)e^{-i\Delta z k_o \delta n} \quad (23)$$

where  $E^o(x, y, \Delta z)$  represents the field propagated through the linear medium. For  $E^o(x, y, \Delta z)$  we have again the scalar Helmholtz equation,

$$\left( \nabla_{\perp}^2 + \frac{\partial^2}{\partial z^2} \right) E^o + k_o^2 n_o^2 E^o = 0. \quad (24)$$

We assume the following solution,

$$E^o = \Psi e^{-ik_o n_o z} \quad (25)$$

where  $\Psi$  is complex. Inserting Eq.25 into Eq.24 we arrive at,

$$-2ik_o n_o \frac{\partial \Psi}{\partial z} + \nabla_{\perp}^2 \Psi = 0 \quad (26)$$

where the slowly varying envelope approximation has been assumed, namely,

$$k_o n_o \frac{\partial \Psi}{\partial z} \gg \frac{\partial^2 \Psi}{\partial z^2} \quad (27)$$

We have chosen cylindrical coordinates with azimuthal symmetry as this is conducive with the experimental geometry whereby a TEM<sub>00</sub> gaussian beam has been used. First we separate  $\Psi$  into its real and imaginary components,  $\Psi^R$  and  $\Psi^I$  respectively, and upon substitution into Eq.26 and identifying the real and imaginary parts we obtain,

$$k_o n_o \frac{\partial \Psi^R}{\partial z} = \nabla_{\perp}^2 \Psi^I \quad (28)$$

$$k_o n_o \frac{\partial \Psi^I}{\partial z} = -\nabla_{\perp}^2 \Psi^R \quad (29)$$

The transverse laplacian is written as,

$$\nabla_{\perp}^2 = \frac{1}{r} \frac{\partial}{\partial r} + \frac{\partial^2}{\partial r^2} \quad (30)$$

Eq.28 and Eq.29 are then solved numerically. This is discussed in a later section.



## Propagation of External Fields

In this section we establish an expression for the electric field profile immediately within the front face of the sample. Referring to Figure 2 we wish to propagate some incident field through a focusing lens, some distance  $Z_{sample}$  in vacuum and then through some dielectric interface. ( $Z_{sample}$  is not explicitly identified in Figure 2 due to congestion. It is simply the distance between the sample front face and the principle plane of lens L1.)

The electric field profile incident on the lens L1,  $E_1(r, 0)$ , is transformed in the thin lens approximation to  $E_2(r, 0)$ , by a phase factor expressed as,

$$E_2(r, 0) = E_1(r, 0)e^{i\frac{k_0 r^2}{2f}} \quad (31)$$

where  $k_0 = \frac{2\pi}{\lambda_0}$ ,  $\lambda_0$  is the free space wavelength and  $f$  is the focal length.  $E_1(r, 0)$  is determined by the mode of the incident laser light and is assumed to be a perfectly collimated gaussian TEM<sub>00</sub> mode. Thus we have that,

$$E_1(r, 0) = E_o e^{-\frac{r^2}{w_o^2}} \quad (32)$$

where  $E_o$  is the magnitude of the incident field and  $w_o$  the characteristic waist size (spot size).

The incident field magnitude,  $E_o$ , is found by knowing the incident power,  $P_{in}$ , namely,

$$P_{in} = \int_S \frac{\langle |E_1(r, 0)|^2 \rangle_{time}}{\eta_o} dS \quad (33)$$

where  $\eta_o = \sqrt{\frac{\mu_o}{\epsilon_o}} \cong 377\Omega$  and is the impedance in a vacuum. Substituting in Eq.32 and integrating over all space in cylindrical coordinates we arrive at,

$$|E_o| = \sqrt{\frac{4P_{in}\eta_o}{\pi w_o^2}} \quad (34)$$

We find the electric field immediately within the sample,  $E_3(r, z_{sample})$ , located a distance  $z_{sample}$  from the focusing lens, by propagating  $E_2(r, 0)$  using the Huygen-Fresnel diffraction integral[25]. Namely,

$$E_3(r, z_{sample}) = -i \frac{k_o}{z_{sample}} e^{-i\frac{k_o r^2}{2z_{sample}}} \int_0^\infty E_2(r_o, 0) e^{-i\frac{k_o r_o^2}{2z_{sample}}} J_0\left(\frac{k_o r r_o}{z_{sample}}\right) r_o dr_o \quad (35)$$

where we have used cylindrical coordinates and the azimuthal integration has already been carried out. Using Eq.31 and Eq.32, we obtain,

$$E_3(r, z_{samp}) = \Psi_o e^{i\Phi} \quad (36)$$

where,

$$\Psi_o = \frac{E_o}{\xi \sqrt{1 + \gamma^2}} \exp \left[ -\frac{\theta^2}{\xi^2 (1 + \gamma^2)^{\frac{3}{2}}} \right] \quad (37)$$

$$\Phi = \frac{\theta^2 \gamma}{\xi^2 (1 + \gamma^2)^{\frac{3}{2}}} - \tan^{-1}(\gamma) - \frac{\theta^2}{\xi} - \frac{\pi}{2} \quad (38)$$

$$\theta = \frac{r}{w_o} \quad (39)$$

$$\xi = \frac{2z_{samp}}{k_o w_o^2} \quad (40)$$

$$\gamma = \frac{1 - \frac{z_{samp}}{f}}{\xi} \quad (41)$$

To find the field immediately inside the sample medium,  $\Psi(r, z_{samp})$ , we multiply  $E_3(r, z_{samp})$  by the transmittance,  $t_1$ , given by,

$$t_1 = \frac{2}{\tilde{n} + 1} \quad (42)$$

Here  $n$  is given by,

$$n = n_o + \delta n \cong n_o - i \frac{\alpha}{2k_o} \quad (43)$$

and the transmittance becomes,

$$t_1 = \frac{2}{\sqrt{(n_o + 1)^2 + \left(\frac{\alpha}{2k_o}\right)^2}} \exp \left[ i \tan^{-1} \left( \frac{\alpha}{2(n_o + 1)k_o} \right) \right] \quad (44)$$

where  $\alpha = \alpha(r, z_{samp})$ . The time averaged power density immediately inside the sample,  $I(r, z_{samp})$ , is given by,

$$I(r, z_{samp}) = \frac{|\Psi(r, z_{samp})| n_o}{2\eta_o} \quad (45)$$

The fields are then propagated to the back side of the sample numerically. The field then emerging out the back interface,  $E_4(r, z_{samp} + L_o)$ , where  $L_o$  is the sample

thickness, is given by multiplying the field at the back interface  $\Psi(r, z_{samp} + L_o)$  by the transmittance,  $t_2$  where,

$$t_2 = \frac{2\sqrt{\tilde{n}}}{\tilde{n} + 1} \quad (46)$$

which becomes,

$$t_2 = 2 \frac{\left[ n_o^2 + \left( \frac{\alpha}{2k_o} \right)^2 \right]^{\frac{1}{4}}}{\left[ (n_o + 1)^2 + \left( \frac{\alpha}{2k_o} \right)^2 \right]^{\frac{1}{2}}} \exp \left( i \left[ \tan^{-1} \left( \frac{\alpha}{2(n_o + 1)k_o} \right) - \frac{1}{2} \tan^{-1} \left( \frac{\alpha}{2k_o} \right) \right] \right) \quad (47)$$

and  $\alpha = \alpha(r, z_{samp} + L_o)$ . The total power transmitted out the sample,  $T_{out}$ , is determined by integrating over the transmitted time averaged power density,

$$T_{out} = 2\pi \int_0^{\infty} \frac{\langle |E_4(r, z_{samp} + L_o)| \rangle_{time} r dr}{\eta_o} \quad (48)$$

In Eq.35 the bessel function is approximated as [26],

$$J_0(x) \cong 1 - 2.2499997 \left( \frac{x}{3} \right)^2 + 1.2656208 \left( \frac{x}{3} \right)^4 - .3163866 \left( \frac{x}{3} \right)^6 + .04444479 \left( \frac{x}{3} \right)^8 - .0039444 \left( \frac{x}{3} \right)^{10} + .0002100 \left( \frac{x}{3} \right)^{12} \quad (49)$$

for  $0 \leq x \leq 3$  and,

$$J_0(x) \cong \sqrt{\frac{2}{\pi x}} \cos \left( x - \frac{\pi}{4} \right) \quad (50)$$

for  $x > 3$ .

### Finite Difference Schemes

In this section the explicit finite difference technique[27] is established for the heat flow equation, rate equation for the electron-hole density, and the real and imaginary components of the wave equation, previously separated. Cylindrical coordinates are used in order to take advantage of azimuthal symmetry.

The heat flow equation is,

$$\frac{1}{\eta_{th}} \frac{\partial(\Delta T)}{\partial t} = \frac{1}{r} \frac{\partial(\Delta T)}{\partial r} + \frac{\partial^2(\Delta T)}{\partial r^2} + \frac{\partial^2(\Delta T)}{\partial z^2} + \frac{N\hbar\omega}{\tau k_{th}} \quad (51)$$

where  $\eta_{th}$  is the thermal diffusivity,  $\Delta T$  is the change in temperature (from room temperature),  $N$  is the electron-hole density,  $\hbar\omega$  is the photon energy,  $\tau$  is the electron-hole recombination time, and  $k_{th}$  is the thermal conductivity. For the electron-hole density we use the following rate equation,

$$\frac{\partial N^{(ns)}}{\partial t} = D_a \left( \frac{1}{r} \frac{\partial N^{(ns)}}{\partial r} + \frac{\partial^2 N^{(ns)}}{\partial r^2} + \frac{\partial^2 N^{(ns)}}{\partial z^2} \right) - \frac{N^{(ns)}}{\tau} + \frac{\alpha I}{\hbar\omega} \quad (52)$$

where  $D_a$  is the ambipolar diffusion coefficient,  $\alpha$  is the linear absorption coefficient, and  $I$  the intensity. Here the superscript  $(ns)$  will be used to indicate a nonstationary solution for the electron-hole density. In order to isolate the carrier dynamics we will also have occasion to use the steady-state, diffusion free electron-hole density, indicated by  $N^{(s)}$ , which can be seen to be,

$$N^{(s)} = \frac{\alpha I \tau}{\hbar\omega} \quad (53)$$

Numerically, we use an explicit finite difference technique. For the electric field we use the following approximations,

$$\frac{\partial \Psi^\xi}{\partial z} \cong \frac{\Psi^\xi(i, j+1) - \Psi^\xi(i, j-1)}{2\Delta z}, j > 1 \quad (54)$$

$$\frac{\partial \Psi^\xi}{\partial z} \cong \frac{\Psi^\xi(i, j+1) - \Psi^\xi(i, j)}{\Delta z}, j = 1 \quad (55)$$

where  $\xi$  stands for R or I. For the wave equation, heat flow equation, and electron-hole density we have that,

$$\frac{1}{r} \frac{\partial \Xi}{\partial r} \cong \frac{\Xi(i+1, j, k) - \Xi(i-1, j, k)}{2(i-1)\Delta r^2}, i > 1 \quad (56)$$

$$\frac{1}{r} \frac{\partial \Xi}{\partial r} = \frac{\partial^2 \Xi}{\partial r^2}, i = 1 \quad (57)$$

$$\frac{\partial^2 \Xi}{\partial r^2} \cong \frac{\Xi(i+1, j, k) - 2\Xi(i, j, k) + \Xi(i-1, j, k)}{\Delta r^2}, i > 1 \quad (58)$$

$$\frac{\partial^2 \Xi}{\partial r^2} \cong 2 \frac{\Xi(i+1, j, k) - \Xi(i, j, k)}{\Delta r^2}, i = 1 \quad (59)$$

$$\frac{\partial \Xi}{\partial t} \cong \frac{\Xi(i, j, k+1) - \Xi(i, j, k)}{\Delta t} \quad (60)$$

where  $\Xi$  may be  $\Psi^R$ ,  $\Psi^I$ ,  $\Delta T$ , or  $N$ . For the heat flow equation and electron-hole density,

$$\frac{\partial^2 \Xi}{\partial z^2} \cong \frac{\Xi(i, j+1, k) - 2\Xi(i, j, k) + \Xi(i, j-1, k)}{\Delta z^2}, 1 < j < j_{\max} \quad (61)$$

where  $\Xi$  may be either  $\Delta T$  or  $N$ . At the boundaries  $j = 1$  and  $j = j_{\max}$  we have for the change in temperature the following expressions,

$$\frac{\partial^2(\Delta T)}{\partial z^2} \cong \frac{\Delta T(i, j+1, k) - \Delta T(i, j, k)}{\Delta z^2} - \frac{H\Delta T(i, j, k)}{k_{th}\Delta z}, j = 1 \quad (62)$$

$$\frac{\partial^2(\Delta T)}{\partial z^2} \cong \frac{\Delta T(i, j-1, k) - \Delta T(i, j, k)}{\Delta z^2} - \frac{H\Delta T(i, j, k)}{k_{th}\Delta z}, j = j_{\max} \quad (63)$$

where  $H$  is the convective heat transfer coefficient representing cooling at the boundary by convection. For the electron-hole density we have the boundary conditions,

$$\frac{\partial^2 N}{\partial z^2} \cong \frac{N(i, j+1, k) - 2N(i, j, k)}{\Delta z^2}, j = 1 \quad (64)$$

$$\frac{\partial^2 N}{\partial z^2} \cong \frac{-2N(i, j, k) + N(i, j-1, k)}{\Delta z^2}, j = j_{\max} \quad (65)$$

For the real and imaginary components of the wave equation the boundary condition at the front face,  $j = 1$ , is given by the incident field,

$$\Psi^R = Re\{E_3(r, z_{samp})\}Re\{t_1\} - Im\{E_3(r, z_{samp})\}Im\{t_1\} \quad (66)$$

$$\Psi^I = Im\{E_3(r, z_{samp})\}Re\{t_1\} + Re\{E_3(r, z_{samp})\}Im\{t_1\} \quad (67)$$

where  $E_3(r, z_{samp})$  and  $t_1$  are given by Eq.36 and Eq.44 respectively.

In Eq.52 the recombination term,  $-\frac{N^{(ns)}}{\tau}$ , is evaluated at  $(i, j, k+1)$ . In all these approximations the indices  $i, j, k$  have the following meaning:  $r = (i-1)\Delta r$ ,  $z = (j-1)\Delta z$ ,  $t = (k-1)\Delta t$ , and  $i = \{1, i_{\max}\}$ ,  $j = \{1, j_{\max}\}$ .  $j_{\max}$  of course is governed by the sample thickness and  $\Delta z$ .

### Stability of Numerical Schemes

In this section we will consider some requirements for the stability of the numerical solution to the wave equation, heat flow equation, and rate equation.

Here stability refers to the unstable growth or stable decay of errors introduced by the arithmetic operations necessary to solve the finite difference equations. If the finite difference scheme is stable then in principle the computational errors can be made arbitrarily small. Stability is a necessary condition for an accurate numerical solution. Most explicit schemes are conditionally stable, while most implicit schemes are unconditionally stable. However when choosing a finite difference scheme one must also consider the computation time. Many methods have been attempted here and it has been found that in reference to computational speed and memory storage requirements the relatively simple "classical" explicit schemes have worked best. (Most implicit schemes yield matrix algebra equations which were found computationally inefficient.)

Perhaps the most widely used procedure for establishing stability requirements for a finite difference scheme is called von Neumann stability. Consider a two dimensional problem with independent variables (x,t). The method introduces a line of errors along x at t=0 and test the growth or decay of these errors along t. The method applies to linear, constant coefficient, finite difference approximations. In the case of nonlinear problems some local linearization is necessary. According to the authors of a highly cited text on finite difference techniques[28], "It is difficult, if not impossible, to generate results on stability, convergence, and consistency for nonlinear PDE approximations; the best that one can usually do is obtain results on a local basis in which certain terms are averaged or even held constant."

First we will consider the wave equation in the linear medium,

$$2in_0k_0 \frac{\partial \tilde{\Psi}}{\partial z} = \frac{1}{r} \frac{\partial \tilde{\Psi}}{\partial r} + \frac{\partial^2 \tilde{\Psi}}{\partial r^2} \quad (68)$$

From before we use the following finite difference approximation,

$$in_0k_0 \frac{\tilde{\Psi}(i, j+1) - \tilde{\Psi}(i, j-1)}{\Delta z} = \frac{\tilde{\Psi}(i+1, j) - \tilde{\Psi}(i-1, j)}{2r\Delta r} + \frac{\tilde{\Psi}(i+1, j) - 2\tilde{\Psi}(i, j) + \tilde{\Psi}(i-1, j)}{(\Delta r)^2} \quad (69)$$

which reduces to,

$$\begin{aligned} \tilde{\Psi}(i, j+1) = & \tilde{\Psi}(i, j-1) + \tilde{c}_1 [\tilde{\Psi}(i+1, j) - \tilde{\Psi}(i-1, j)] + \\ & \tilde{c}_2 [\tilde{\Psi}(i+1, j) - 2\tilde{\Psi}(i, j) + \tilde{\Psi}(i-1, j)] \end{aligned} \quad (70)$$

where,

$$\tilde{c}_1 = -\frac{i\Delta z}{2n_o k_o r \Delta r} \quad (71)$$

$$\tilde{c}_2 = -\frac{i\Delta z}{n_o k_o (\Delta r)^2} \quad (72)$$

We now define  $\delta\tilde{\Psi}(i, j)$  as the error difference between the exact solution and the finite difference approximation. That is the solution  $\tilde{\Psi}(i, j)$  may be represented in our finite difference approximation as,

$$\tilde{\Psi}(i, j) = \Psi^{exact}(i, j) + \delta\tilde{\Psi}(i, j) \quad (73)$$

Substituting Eq.73 into Eq.70 yields,

$$\begin{aligned} \delta\tilde{\Psi}(i, j+1) = & \delta\tilde{\Psi}(i, j-1) + \tilde{c}_1 [\delta\tilde{\Psi}(i+1, j) - \delta\tilde{\Psi}(i-1, j)] + \\ & \tilde{c}_2 [\delta\tilde{\Psi}(i+1, j) - 2\delta\tilde{\Psi}(i, j) + \delta\tilde{\Psi}(i-1, j)] \end{aligned} \quad (74)$$

Our goal is to establish the condition on  $\Delta z$  and  $\Delta r$  such that given some  $\delta\tilde{\Psi}(i, j)$ ,  $\delta\tilde{\Psi}(i, j+1)$  does not grow without bound. This von Neumann stability is carried out by expanding  $\delta\tilde{\Psi}(i, j)$  by a Fourier series,

$$\delta\tilde{\Psi}(m, j) = \sum_p a_p^j e^{i\beta_p m \Delta r} \quad (75)$$

We will also make the definition,

$$\delta\tilde{\Theta}(m, j) = \delta\tilde{\Psi}(m, j-1) = \sum_p b_p^j e^{i\beta_p m \Delta r} \quad (76)$$

Upon substituting into Eq.74 our Fourier series representation and recognizing that all Fourier terms add linearly, we note we need only to consider one such term. Eq.74 thus reduces to,

$$a_p^{j+1} = a_p^{j-1} + [\tilde{c}_1 (e^{i\beta_p m \Delta r} - e^{-i\beta_p m \Delta r}) + \tilde{c}_2 (e^{i\beta_p m \Delta r} + e^{-i\beta_p m \Delta r} - 2)] a_p^j \quad (77)$$

Which after some simplification and Eq. 76 becomes in matrix form,

$$\begin{pmatrix} a_p^{j+1} \\ b_p^{j+1} \end{pmatrix} = \begin{pmatrix} [2i\tilde{c}_1 \sin(\beta_p m \Delta r) - 4\tilde{c}_2 \sin^2\left(\frac{\beta_p m \Delta r}{2}\right)] & 1 \\ 1 & 0 \end{pmatrix} \begin{pmatrix} a_p^j \\ b_p^j \end{pmatrix} \quad (78)$$

In order for the errors to not grow the eigenvalues of the 2x2 matrix must be  $\leq 1$ .

The eigenvalues  $\lambda_\ell$  are given by the solution of,

$$\lambda_\ell^2 - \left[ 2i\tilde{c}_1 \sin(\beta_p m \Delta r) - 4\tilde{c}_2 \sin^2\left(\frac{\beta_p m \Delta r}{2}\right) \right] \lambda_\ell - 1 = 0 \quad (79)$$

and the stability condition,  $|\lambda_\ell| \leq 1$ , becomes,

$$\left| |\tilde{c}_1| \sin(\zeta) + 2i |\tilde{c}_2| \sin^2\left(\frac{\zeta}{2}\right) + \sqrt{\left[ |\tilde{c}_1| \sin(\zeta) + 2i |\tilde{c}_2| \sin^2\left(\frac{\zeta}{2}\right) \right]^2 + 1} \right| \leq 1 \quad (80)$$

where  $\zeta = \beta_p m \Delta r$ . This condition must hold for all  $r$  thus we may set  $|\tilde{c}_1| = 0$  as well as all  $\zeta$ , thus we set  $\zeta = 0$ . Eq.80 then becomes,

$$\left| 2i |\tilde{c}_2| + \sqrt{1 - 4 |\tilde{c}_2|^2} \right| \leq 1 \quad (81)$$

If the argument of the square root is positive we are guaranteed stability. If the argument is negative we arrive at,

$$|\tilde{c}_2| \leq \frac{1}{2} \quad (82)$$

Backing up slightly we must recall that at  $r = 0$  we have that,

$$\frac{1}{r} \frac{\partial}{\partial r} \rightarrow \frac{\partial^2}{\partial r^2} \quad (83)$$

which translates here to  $\tilde{c}_1 \rightarrow 0$  and  $\tilde{c}_2 \rightarrow 2\tilde{c}_2$  and thus Eq.?? is further restricted (in the sense that  $|\tilde{c}_2|$  is further restricted), giving,

$$4 |\tilde{c}_2| \leq 1 \quad (84)$$

or,

$$\Delta z \leq \frac{1}{4} n_o k_o \Delta r^2 \quad (85)$$

Eq.85 is the stability requirement for the finite difference approximation to the linear wave equation. One should keep in mind however that this stability



criteria is merely a necessary condition, but perhaps insufficient condition. What we really desire is a stable finite difference solution to the nonlinear wave equation of which is further complicated by its coupling to the heat flow equation. Thus Eq.85 merely suggests an upper limit on  $\Delta z$ , given some sufficient  $\Delta r$ .  $\Delta r$  has been chosen merely from insight into the physical problem, desired resolution, computation time, and "trial-and-error".

Of the three governing equations under consideration (wave equation, heat flow equation, and rate equation) the linear wave equation is the only one without any explicit time dependence, thus we have used it to establish our stability requirement amongst the spatial variables  $r$  and  $z$ . Next we must establish a stability condition relating the time variable with the spatial variables. This problem is greatly simplified by observing the relative time scales for the heat flow equation and the rate equation. If we assume a steady state solution to the rate equation then the heat flow equation will dictate the stability criteria. If we do not use a steady state solution to the rate equation then we approximate the temperature as a constant over any small time interval and use the rate equation to establish our stability criteria. This turns out to be justified in that the time scales amongst the two phenomenon are orders of magnitude apart. In both cases we must assume that the intensity is constant over the respective time intervals.

First we will consider the heat flow equation with a steady state carrier density. We must linearize the expression for the absorption coefficient in order to invoke the von Neumann stability analysis. Our expression for the coefficient of absorption (Urbach's rule) is,

$$\alpha = \alpha_o e^{\frac{\sigma}{k_b(T_o + \Delta T)}} \left( \hbar\omega + E_x - E_{g_o} - \frac{\partial E_g}{\partial T} \Delta T \right) \quad (86)$$

which by a Taylor series expansion about  $\Delta T = 0$  is approximated as,

$$\alpha \cong \alpha_1 + \alpha_2 \Delta T \quad (87)$$

$$\alpha_1 = \alpha_o e^{\frac{\sigma}{k_b T_o}} (\hbar\omega + E_x - E_{g_o}) \quad (88)$$

$$\alpha_2 = -\alpha_1 \frac{\sigma}{k_b T_o^2} \left( \hbar\omega + E_x - E_{g_o} - \frac{\partial E_g}{\partial T} T_o \right) \quad (89)$$

Here  $T_o$  would be continuously updated as to keep this first order expansion accurate. Using this linearization the heat flow equation becomes,

$$\frac{1}{\eta_{th}} \frac{\partial T}{\partial t} = \frac{1}{r} \frac{\partial T}{\partial r} + \frac{\partial^2 T}{\partial r^2} + \frac{\partial^2 T}{\partial z^2} + \frac{(\alpha_1 - \alpha_2 T)I}{k_{th}} \quad (90)$$

where now it should be understood that  $T$  is actually  $\Delta T$ . Again we will approximate the exact partial differential equation with a finite difference representation and consider the growth in the error. Let the error introduced by our finite difference approximation be  $\delta T$ . The equation for the error becomes,

$$\frac{1}{\eta_{th}} \frac{\partial(\delta T)}{\partial t} = \frac{1}{r} \frac{\partial(\delta T)}{\partial r} + \frac{\partial^2(\delta T)}{\partial r^2} + \frac{\partial^2(\delta T)}{\partial z^2} - \frac{\alpha_2 I}{k_{th}} \delta T \quad (91)$$

We will analyze the following finite difference approximation to Eq.91,

$$\begin{aligned} \frac{1}{\eta_{th}} \frac{\delta T(i, j, k+1) - \delta T(i, j, k)}{\Delta t} &= \frac{1}{r} \frac{\delta T(i+1, j, k) - \delta T(i-1, j, k)}{2\Delta r} + \\ &\frac{\delta T(i+1, j, k) - 2\delta T(i, j, k) + \delta T(i-1, j, k)}{\Delta r^2} + \\ &\frac{\delta T(i, j+1, k) - 2\delta T(i, j, k) + \delta T(i, j-1, k)}{\Delta z^2} - \frac{\alpha_2 I}{k_{th}} \delta T(i, j, k) \end{aligned} \quad (92)$$

Again we now express the error in a Fourier series representation (in this case a two dimensional series),

$$\delta T(m, n, k) = \sum_p \sum_q a_{p,q}^k e^{i\beta_p m \Delta r} e^{i\beta_q n \Delta z} \quad (93)$$

Substituting our Fourier series representation into Eq.92 and realizing that only a single Fourier term in each dimension need be analyzed we arrive at,

$$\begin{aligned} a_{p,q}^{k+1} &= a_{p,q}^k + \frac{\eta_{th} \Delta t}{2m \Delta r^2} (e^{i\beta_p \Delta r} - e^{-i\beta_p \Delta r}) a_{p,q}^k + \\ &\left[ \frac{\eta_{th} \Delta t}{\Delta r^2} (e^{i\beta_p \Delta r} + e^{-i\beta_p \Delta r} - 2) + \frac{\eta_{th} \Delta t}{\Delta z^2} (e^{i\beta_q \Delta z} + e^{-i\beta_q \Delta z} - 2) - \frac{\eta_{th} \alpha_2 I}{k_{th}} \Delta t \right] a_{p,q}^k \end{aligned} \quad (94)$$

which simplifies to,

$$\begin{aligned} a_{p,q}^{k+1} &= a_{p,q}^k \left[ 1 + i \frac{\eta_{th}}{m} \frac{\Delta t}{\Delta r^2} \sin(\beta_p \Delta r) - 4\eta_{th} \frac{\Delta t}{\Delta r^2} \sin^2 \left( \frac{\beta_p \Delta r}{2} \right) - \right. \\ &\left. 4\eta_{th} \frac{\Delta t}{\Delta z^2} \sin^2 \left( \frac{\beta_q \Delta z}{2} \right) - \frac{\eta_{th} \alpha_2 I}{k_{th}} \Delta t \right] \end{aligned} \quad (95)$$

The stability condition must now be modified slightly. That is a parabolic PDE with a source term must allow for solutions which grow in time. This is known as the *von Neumann necessary condition*[28] and is written as,

$$\left| \frac{a_{p,q}^{k+1}}{a_{p,q}^k} - K\Delta t \right| \leq 1 \quad (96)$$

where  $K$  is some constant. Our stability condition then becomes,

$$\left| 1 + i \frac{\eta_{th}}{m} \frac{\Delta t}{\Delta r^2} \sin(\beta_p \Delta r) - 4\eta_{th} \frac{\Delta t}{\Delta r^2} \sin^2\left(\frac{\beta_p \Delta r}{2}\right) - 4\eta_{th} \frac{\Delta t}{\Delta z^2} \sin^2\left(\frac{\beta_q \Delta z}{2}\right) - \frac{\eta_{th} \alpha_2 I}{k_{th}} \Delta t - K\Delta t \right| \leq 1 \quad (97)$$

After a tedious calculation one can show that the magnitude of the left side of Eq.97 has a maximum (worst case scenario) and minimum when the arguments of the trigonometric functions are 0 or  $\pi$ . Thus Eq.97 reduces to,

$$-1 \leq 1 - \frac{\eta_{th} \alpha_2 I}{k_{th}} \Delta t - 4c_2 \Delta t \left( \frac{1}{\Delta r^2} + \frac{1}{\Delta z^2} \right) - K\Delta t \leq 1 \quad (98)$$

Upon setting  $K = -\frac{\eta_{th} \alpha_2 I}{k_{th}}$  we arrive at,

$$\Delta t \leq \frac{1}{2\eta_{th}} \left( \frac{1}{\Delta r^2} + \frac{1}{\Delta z^2} \right)^{-1} \quad (99)$$

This is our stability condition for the heat flow equation. Note, the final result is independent of the source term as well as the first derivative term. This is a common result.

Finally we must consider the rate equation, or rather the error,  $\delta N$ , associated with the finite difference approximation to the rate equation,

$$\frac{\partial(\delta N)}{\partial t} = D_a \left( \frac{1}{r} \frac{\partial(\delta N)}{\partial r} + \frac{\partial^2(\delta N)}{\partial r^2} + \frac{\partial^2(\delta N)}{\partial z^2} \right) - \frac{\delta N}{\tau} \quad (100)$$

Note because the source term is not written explicitly as a function of the carrier density it does not appear in the differential equation for the error. Referring to the finite difference scheme from before and again using the von Neumann stability analysis we arrive at,

$$-1 \leq 1 - 4D_a \left( \frac{1}{\Delta t} + \frac{1}{\tau} \right)^{-1} \left( \frac{1}{\Delta r^2} + \frac{1}{\Delta z^2} \right) \leq 1 \quad (101)$$

Here  $K$  was set equal to zero because the source term did not appear in the finite difference scheme for the error term. In other words the source term was not written explicitly as a function of the carrier density, but has been treated as a constant over some small time  $\Delta t$ . From Eq.101 our stability condition is,

$$\Delta t \leq \left[ 2D_a \left( \frac{1}{\Delta r^2} + \frac{1}{\Delta z^2} \right) - \frac{1}{\tau} \right]^{-1} \quad (102)$$

### Conclusion

We have outlined our numerical scheme for finding a solution to the three governing equations: namely the electric field (wave equation), heat flow equation, and electron hole density. Although the classic explicit scheme used is perhaps not the most perfect scheme one could contrive, the justification here is the justification for any numerical approximation, namely that it works. Computational speed was perhaps the most vexing consideration. Implicit schemes were developed along with numerical algorithms to solve the subsequent matrix algebra problems but the computational effort way exceeded the gain in stability. We have used the well known and most often applied, von Neumann stability analysis to establish a guideline for the choice of our numerical grid. These results should however only serve as a guideline as certain approximations have been invoked in order to decouple the respective equations.

The program developed was simulated on the Oklahoma State University VMS (vax) mainframe. The program lines are the contents of Appendix A.

### Theory II.B.

In this section we will present the results of a quantum mechanical theory for the absorption coefficient in a two band semiconductor for arbitrary wavelength, temperature, and e-h density. The motivation for this is to essentially be able to compute the absorption spectra accurately as a function of these variables so as to be able to compute through the Kramers-Kronig relations<sup>-1</sup> any resonant enhancement of the refractive index. As previously mentioned, section Theory I, we only

employ this calculation for that purpose, as this calculation is computationally time consuming and could not feasibly be applied to the numerical simulations outlined in section Theory II.A..

Below the band gap the induced electron-hole (e-h) density is relatively small, however as the temperature is slowly elevated due to the radiationless recombination of these e-h pairs, the band gap is tuned to longer wavelengths. Upon completely temperature tuning the band gap such that interband transitions become possible, an e-h plasma may result. Each e-h pair then interacts with this plasma greatly influencing the optical properties of the semiconductor. A partly phenomenological theory of the nonlinear optical properties of semiconductors in the spectral vicinity of the absorption edge as a function of temperature and e-h density has been offered by Bányai and Koch(1986)[29]. The theory is an extension of the well known Elliott formula[30] and is based on the many particle Hamiltonian of a system of interacting electrons and holes in a two band semiconductor. The attractive coulomb potential is replaced by a screened one, the Yukawa potential whereby the screening length is dependent on both temperature and e-h density. The relative motion amongst the e-h pair is then described by Schroedinger's equation. This is the modified Wannier equation. In order to solve the Wannier equation the Yukawa potential is approximated by the Hulthén potential.

The theory is a nontrivial one and many details have been omitted here. Our goal has been to use this theory and not necessarily argue its merits. Many authors have shown excellent agreement amongst this theory and experimentally determined absorption spectra and index of refraction spectra as a function of both temperature and e-h density. Again, our purpose for using this theory is to accurately fit the absorption spectra as a function of temperature and e-h density and then by means of the Kramer's-Kronig relations determine the change in the refractive index as the energy gap is temperature tuned to the wavelength of interest. This effectively gives the on-resonant contribution to the change in the refractive index. We will do this for both ZnSe and CdS.

The final expression for the absorption coefficient is[29],

$$\alpha \cong \frac{\omega}{c\sqrt{\epsilon_0}} \text{Im}\epsilon(\omega) \quad (103)$$

$$\text{Im}\epsilon(\omega) = \bar{\epsilon} \tanh \left[ \frac{1}{2} \left( \frac{\tilde{\omega}}{\tilde{T}} - \tilde{\mu}_e - \tilde{\mu}_h \right) \right] [B(\omega) + C(\omega)] \quad (104)$$

$$B(\omega) = \sum_{\ell=1}^{\sqrt{g}} 2\pi \delta_{\tilde{\Gamma}} \left[ \tilde{\omega} + \left( \frac{1}{\ell} - \frac{\ell}{g} \right)^2 \right] \left[ \frac{(g - \ell^2)(2\ell^2 - g)}{\ell^3 g^2} \right] \prod_{n=1(\neq \ell)}^{\infty} \frac{n^2 [n^2 \ell^2 - (g - \ell^2)^2]}{(n^2 \ell^2)(n^2 \ell^2 - g^2)} \quad (105)$$

$$C(\omega) = \int_0^{\infty} dx \sqrt{x} \prod_{n=1}^{\infty} \left[ 1 + \frac{2gn^2 - g^2}{(n^2 - g)^2 + n^2 g^2 x} \right] \delta_{\tilde{\Gamma}}(x - \tilde{\omega}) \quad (106)$$

where,

$$\bar{\epsilon} = \frac{r_{cv}^2}{2\pi a_o^3 E_R}, \tilde{\omega} = \frac{\hbar\omega - E_g}{E_R}, \tilde{T} = \frac{k_B T}{E_R}, \tilde{\Gamma} = \frac{\Gamma}{E_R}, \tilde{\mu}_{e,h} = \frac{\mu_{e,h} - \frac{E_g}{2}}{k_b T}, g = \frac{12}{\pi^2 a_o \kappa}$$

$B(\omega)$  represents the bound (exciton) states and  $\sqrt{g}$  indicates that the sum extends over the existing bound states, i.e. up to the largest integer number  $\ell \leq \sqrt{g}$ . If  $g$  is less than one there is no contribution from the bound states. The value of  $g$  comes from the Bargmann theorem[31] which gives an upper limit on the number of bound states for a given potential.  $C(\omega)$  represents the continuum.

Definitions:  $E_R = \frac{\hbar^2}{2m_\mu a_o^2}$  =Rydberg energy,  $a_o$  =Bohr radius,  $m_\mu$  =reduced effective e-h mass,  $\kappa$  =screening length,  $\mu_{e,h}$  =electron,hole chemical potential,  $E_g$  =energy gap at some temperature,  $T$ , and zero e-h density,  $\hbar\omega$  =incident radiation energy per photon, and  $k_B$  =Boltzmann's constant. The following values were used:

CdS[32]:  $a_o = 30.1\text{\AA}$ ,  $m_e^* = .235m_o$ ,  $m_h^* = 1.35m_o$ ,  $E_g(290^\circ K) = 2.44\text{eV}$ ,  $\frac{\partial E_g}{\partial T} = -.5\text{meV}/^\circ K$ ,  $\Gamma = E_R$ .

ZnSe[32]:  $a_o = 44.4\text{\AA}$ ,  $m_e^* = .16m_o$ ,  $m_h^* = .6m_o$ ,  $E_g(290^\circ K) = 2.70\text{eV}$ ,  $\frac{\partial E_g}{\partial T} = -.72\text{meV}/^\circ K$ ,  $\Gamma = E_R$  and  $m_\alpha^*$  is the effective mass of the particle  $\alpha$  where  $\alpha$  stands for either  $e$  (electron) or  $h$  (hole).

The delta function,  $\delta_{\tilde{\Gamma}}$ , represents a broadened delta function used to fit exciton lineshapes and is given by[33],

$$\delta_{\tilde{\Gamma}}(x) = \frac{1}{\pi \tilde{\Gamma} \cosh \left( \frac{x}{\tilde{\Gamma}} \right)} \quad (107)$$

where the  $\Gamma$  in our definition of  $\tilde{\Gamma}$  is used to describe the spectral width and is used as a fitting parameter. The chemical potentials are determined by the temperature and e-h density. By assuming they behave as an ideal Fermi gas we have the following relation,

$$\frac{1}{2\pi^2}(\tilde{T}\tilde{m}_\alpha)^{\frac{3}{2}} \int_0^\infty dx \frac{\sqrt{x}}{1 + \exp(x - \tilde{\mu}_\alpha)} = a_o^3 N_\alpha \quad (108)$$

$$\tilde{m}_\alpha = \frac{m_\alpha}{m_\mu} \quad (109)$$

and  $N_\alpha$  is the density of the particle  $\alpha$ . For a given temperature and particle density Eq.108 is approximated with the use of the Padé approximate technique[34]. The result is,

$$\tilde{\mu}_\alpha = \ln(\Omega) + k_1 \ln(k_2 \Omega + k_3) + k_4 \Omega + k_5 \quad (110)$$

$$\Omega = 4N_\alpha a_o^3 \left( \frac{\pi}{\tilde{T}\tilde{m}_\alpha} \right)^{\frac{3}{2}} \quad (111)$$

$$k_1 = 4.8966851, k_2 = 3.3105795, k_3 = 73.6264033, k_4 = .1333760, k_5 = -21.0508644 \quad (112)$$

Once the chemical potentials have been found the plasma screening length,  $\kappa$ , is determined by,

$$(a_o \kappa)^2 = \frac{4}{\pi} \sqrt{\tilde{T}} \int_0^\infty dx \sqrt{x} \sum_\alpha \tilde{m}_\alpha^{\frac{3}{2}} \left[ \frac{1}{1 + \exp(x - \tilde{\mu}_\alpha)} \right] \left[ 1 - \frac{1}{1 + \exp(x - \tilde{\mu}_\alpha)} \right] \quad (113)$$

Finally, by phenomenologically forcing a constant exciton ground state energy, which is a well known experimental fact for a highly excited semiconductor, the change in the band gap,  $\delta E_g$ , due to the creation of a plasma is,

$$\frac{\delta E_g}{E_R} = -1 + \left( 1 - \frac{1}{g} \right)^2, g \geq 1 \quad (114)$$

$$\frac{\delta E_g}{E_R} = -\frac{1}{g}, g < 1 \quad (115)$$

This effectively stems from equating the change in the exciton binding energy to the magnitude of the change in the band gap, rendering the exciton ground state energy constant.

Obviously the necessary calculations are lengthy. It was found that the infinite products required limits up to approximately 1000 for the bound states and 4000 for the continuum, depending on the value of  $g$  (which is determined by the temperature and carrier density). In the foregoing the integrals which had to be treated numerically were approximated by a simple Riemann sum. More progressive techniques had been examined, however the computational speed of a simple Riemann sum outweighed the negligible accuracy gained from a more involved algorithm. As a final note to calculate the absorption coefficient given the temperature, e-h density, and wavelength requires approximately 1.5 minutes. Thus for a computational grid of say 15x70 points would require approximately 17.5 hours for a single data point in time! Hence the reason for not employing this calculation in the simulations of section Theory II.A.. The calculation has been simulated on the Oklahoma State University VMS (vax) mainframe. The Program lines are the content of Appendix B.

Once a theoretical fit to the absorption coefficient has been established one can then invoke the Kramers-Kronig relations to find the change in the index of refraction spectra as a function of temperature and e-h density. This has proven fruitful in the evaluation of the change in the index of refraction as the band gap is temperature tuned (resonant enhancement). The change in the index of refraction may be approximated by a first order Taylor series expansion,

$$\Delta n = \left( \frac{\partial n}{\partial T} \right)_{off} \Delta T + \left( \frac{\partial n}{\partial T} \right)_{on}^{N_o} \Delta T + \left( \frac{\partial n}{\partial N} \right)_{on}^{T_o} \Delta N \quad (116)$$

In Eq.116 *off* and *on* refer to off-resonance (background or phonon assisted) and on-resonance respectively. The on-resonance terms result from band edge effects where the properties of a semiconductor are very different from those away from the band edge. The term containing the e-h density is effectively an on-resonant term due to the fact that a negligible number of e-h pairs are created far from the band edge. The superscripts on the on-resonant terms imply that these respective quantities are evaluated at a given point. The index of refraction is a function of the temperature and e-h density. We are merely applying a first order expansion.



We note that in Eq.116 we are not concerned with the change in optical path length, merely the change in the refractive index. There is no cavity resonance consideration in our model because we are not dealing with a dispersive form of bistability, thus in this context the optical path length is not of importance but rather the refractive index change alone. Thus the change in length of the sample due to thermal expansion has been ignored.

It is the on-resonance terms we get from a Kramers-Kronig transformation of the absorption spectra. The change in the index of refraction spectra as a function of temperature is given by,

$$\Delta n(\lambda, T, N_o) = \frac{1}{2\pi^2} PV \int_0^{\infty} \frac{\alpha(\lambda', T, N_o) - \alpha(\lambda', T_o, N_o)}{\left(\frac{\lambda'}{\lambda}\right) - 1} d\lambda' \quad (117)$$

and as a function of e-h density,

$$\Delta n(\lambda, T_o, N) = \frac{1}{2\pi^2} PV \int_0^{\infty} \frac{\alpha(\lambda', T_o, N) - \alpha(\lambda', T_o, N_o)}{\left(\frac{\lambda'}{\lambda}\right) - 1} d\lambda' \quad (118)$$

where  $PV$  indicates the principle value. In Figure 4 we show the absorption spectra for ZnSe as a function of temperature. (The results for CdS are included in Chapter IV.) Included are the experimental spectra for the first five temperatures. Figure 5 is the Kramers-Kronig transformation of the absorption spectra for an e-h density of  $10^{21}\text{m}^{-3}$  giving the index of refraction spectra as a function of temperature. For e-h densities less than  $10^{23}\text{m}^{-3}$  these spectra changed negligibly while the computational effort significantly increased. In the bottom figure we show the change in the index of refraction as a function of the change in temperature at the 476.5nm wavelength for low ( $10^{21}\text{m}^{-3}$ ) e-h densities. We see as the band gap is temperature tuned to this wavelength the index of refraction initially drops and then rises to some equilibrium, or final value. We have empirically fitted this curve to a hyperbolic secant function. This function was chosen merely because it possesses the proper character. Our expression for  $\Delta n$  is,

$$\Delta n_{low} = \left[ 1.546 - \frac{2.571}{\cosh\left(\frac{\Delta T - 36.79}{32.45}\right)} \right] \times 10^{-3} \quad (119)$$

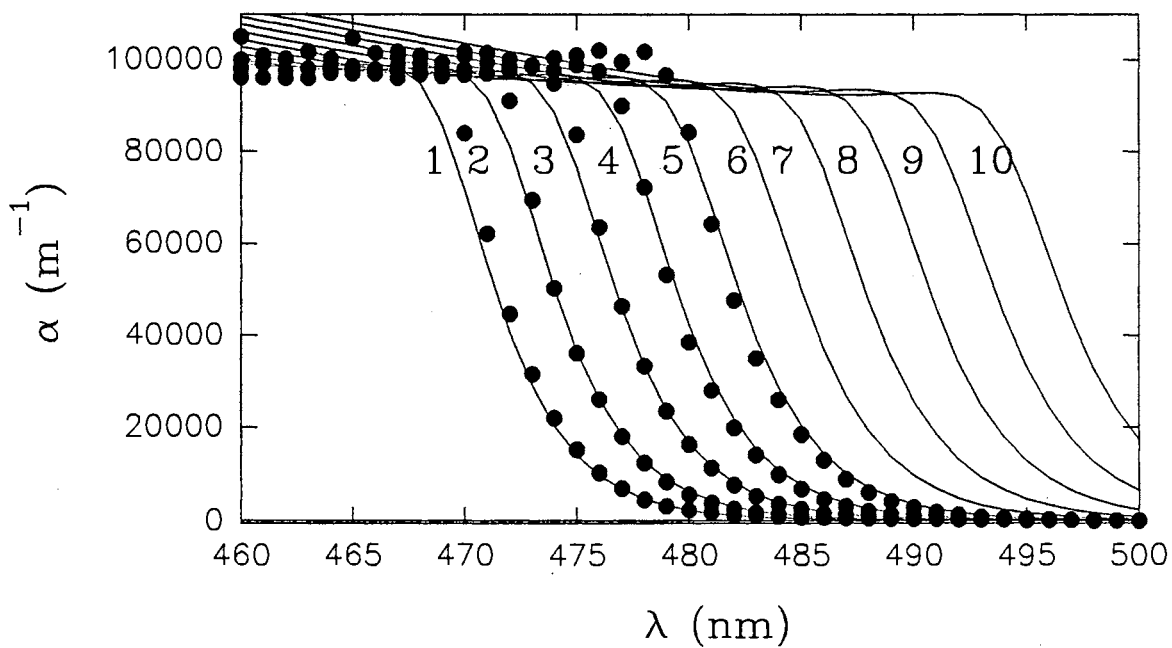


Figure 4. Experimental and theoretical absorption spectra. The filled circles are experimental points while the solid lines are theoretical. The temperatures are room temperature (290K)+ 0, 20, 40, 60, 80, 100, 120, 140, 160, 180 for plots 1 thru 10 respectively.

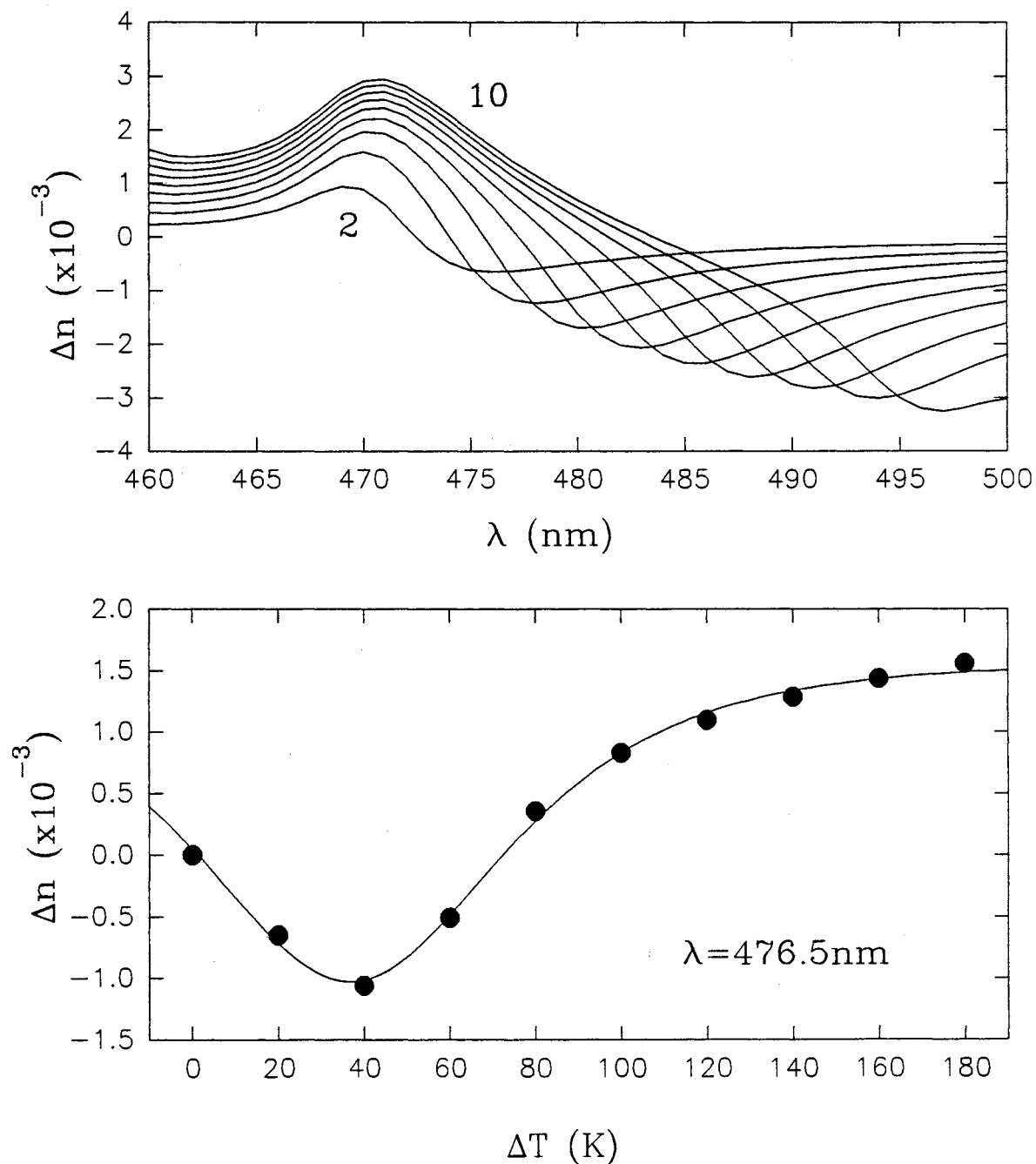


Figure 5. (top) Kramers-Kronig transformation of the absorption spectra for a low e-h density. The curves 2 thru 10 correspond to temperatures  $290\text{K}+20, 40, 60, 80, 100, 120, 140, 160,$  and  $180$  respectively. (bottom) Change in the refractive index as a function of a change in temperature at the wavelength  $476.5\text{nm}$  for low e-h densities.

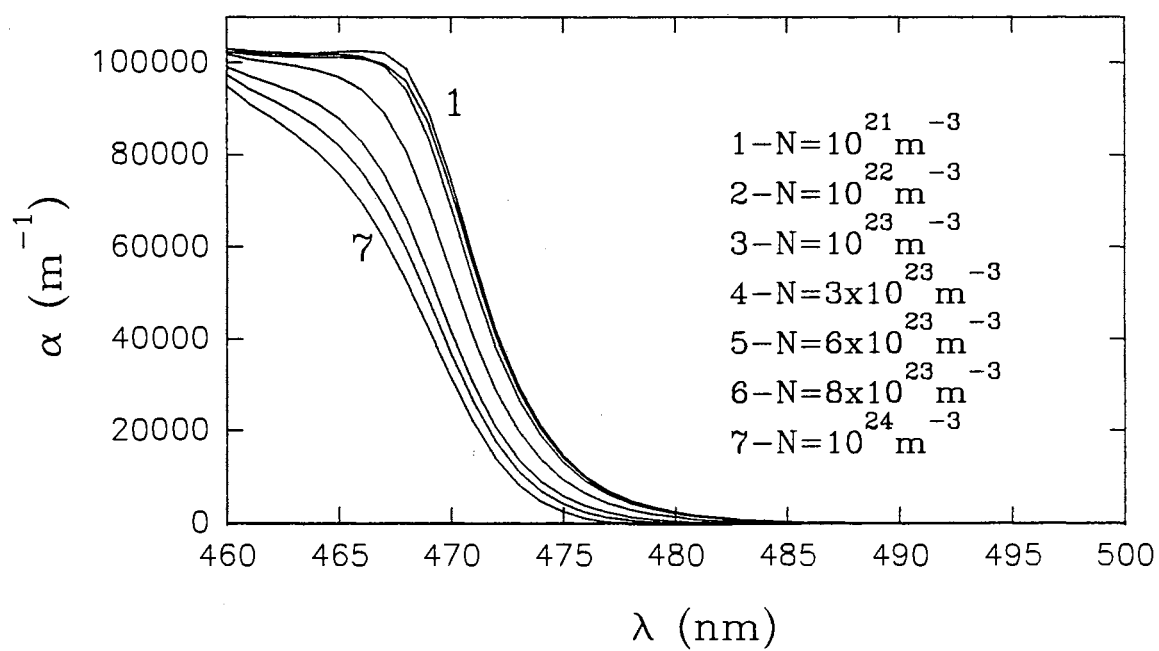


Figure 6. Theoretical absorption spectra for ZnSe at room temperature as a function of e-h density.

In Figure 6 we show the theoretical absorption spectra as a function of e-h density at room temperature. In Figure 7 we show the associative refractive index spectra (top) along with the change in the refractive index at the wavelength 476.5nm (bottom). From this picture it is clear the index change due to the e-h density is small (compared to the temperature effects) for e-h densities less than  $\sim 10^{23}\text{m}^{-3}$ . In Figure 8 we show the absorption as a function of temperature and e-h density. Both graphs (top and bottom) represent the same data, only oriented differently for ease of perspective. This shows that at relatively high temperatures the absorption drops off rapidly near e-h densities beyond  $\sim 10^{24}\text{m}^{-3}$ . This is due to band-filling. The steady-state value for the electron-hole density, for the simplest of rate equations, is given by,

$$N^{(s)} = \frac{\alpha I \tau}{\hbar \omega} \quad (120)$$

As  $\alpha$  approaches zero the intensity,  $I$ , would have to approach infinity for finite  $N^{(s)}$ . An unphysical result. Thus there exist some maximum electron-hole density achievable using a single exciting beam. Also as  $N^{(s)}$  increases  $\alpha$  decreases which in turn decreases  $N^{(s)}$ . It is somewhat unclear what e-h densities are achievable in our experiment. The simple rate equation allows e-h densities beyond  $10^{25}\text{m}^{-3}$  at high excitation levels. However this does not include such nonlinear effects as band-filling, nonconstant ambipolar diffusion, nonconstant thermal conductivity, or higher order recombination terms. At high excitation levels it is likely these quantities become a function of temperature and e-h density. It seems possible that such high e-h densities may never be reached on a  $\mu$  sec time scale (meaning after thermalization and relaxation). For this reason we have ignored the effect of the e-h pairs in the evaluation of the on-resonant enhancement of the refractive index.

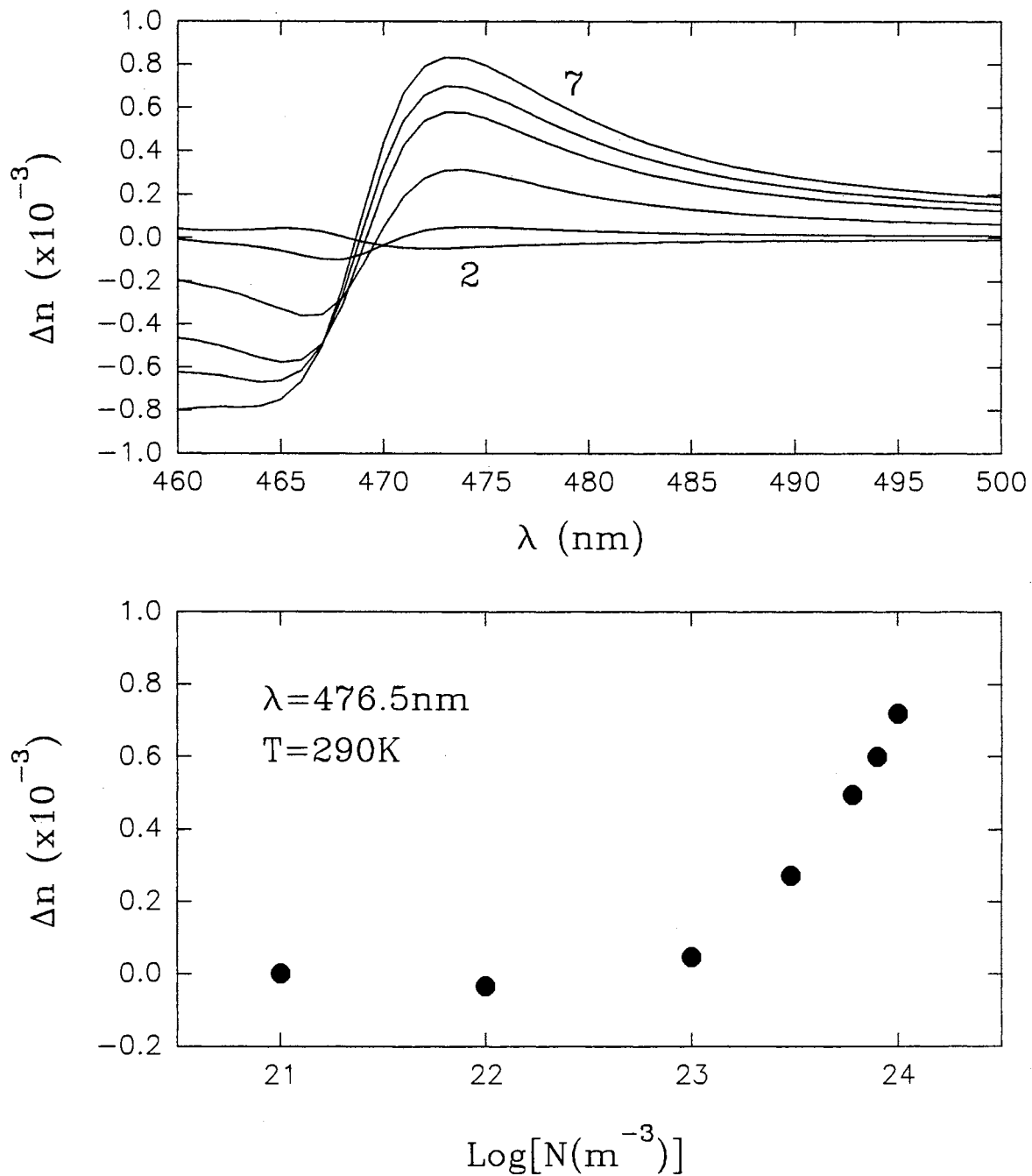


Figure 7. (top) Index of refraction spectra for ZnSe as a function of e-h density and (bottom) the resonant enhancement at 476.5nm.

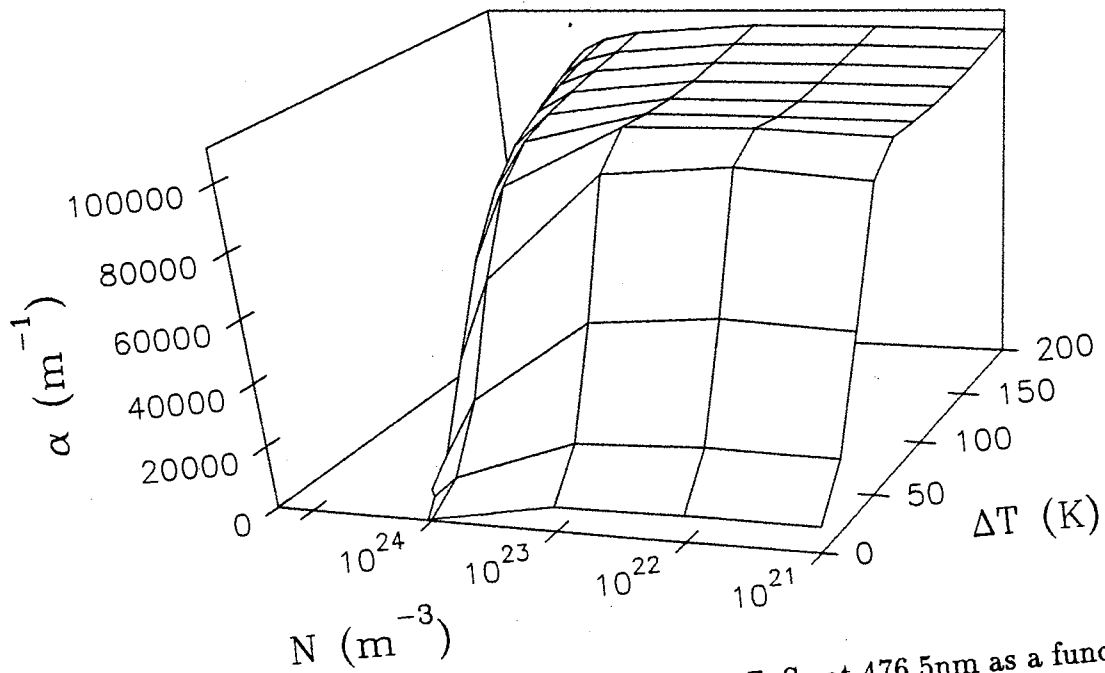
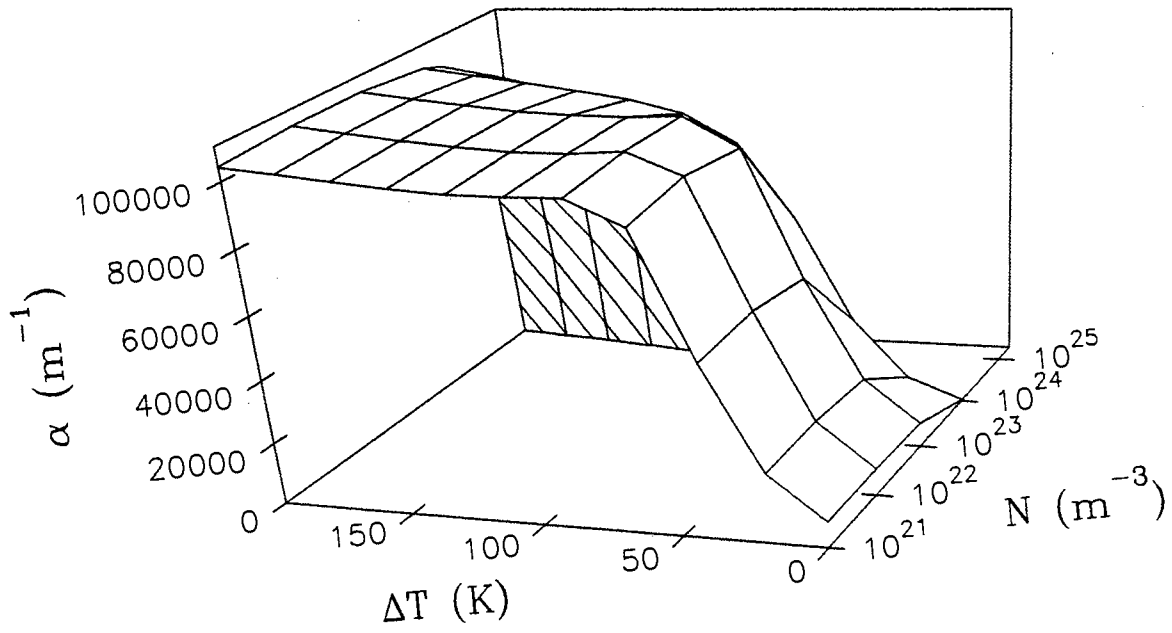


Figure 8. 3-d view of the absorption spectra for ZnSe at 476.5nm as a function of e-h density and temperature.

## Results and Discussion

### Absorptive Switching

Figure 9 illustrates three example cases of the normalized power transmission as a function of time for both the experimental results (left) and theoretical simulations (right). We stress that in all cases the input intensity remains constant from  $t=0$  to beyond the point of switching (i.e. the switching to an "off" state is due to the sample, not the AOM). The powers noted were the actual powers used in the experiment and model. Because one cannot know exactly the location of the sample with respect to the focusing lens this location has been identified theoretically and is given by  $z_{samp}$ . A theoretical value of  $5 \times 10^{-5} K^{-1}$  was used for the off-resonant contribution to the thermo-optic coefficient,  $(\partial n / \partial T)_{off}$ .

The experimental results indicate a very similar temporal profile over a difference in time scale of five orders of magnitude. This would seem to indicate that the same dynamical processes are responsible for the bistable behavior. Using the previously discussed model we were able to theoretically simulate the experimental results to a fair degree of accuracy. Only in the case of the very long time scale, Figure 9.(c.2), does the model begin to resemble less that of the experimental result. Here the model shows a relative fast decrease in transmission at the onset and a near equilibrated regime prior to switching. The experimental result would indicate a gradual decrease in transmission from the onset until switching. In this example we only include the stationary case for the e-h density as this allows for a much greater step size in time.

In Figure 10 we simulate the effects of various parameters on the switching characteristics. In Figure 10.(a) we show the effect of the electronic dynamics. Namely, (a.1) assumes the full non-stationary solution of the e-h density equation while (a.2) assumes a stationary solution. Obviously the effects of diffusion and temporal dynamics are minimal. Therefore the major dynamical process is governed by the heat flow equation. In the five other graphs we have used a stationary e-h density.



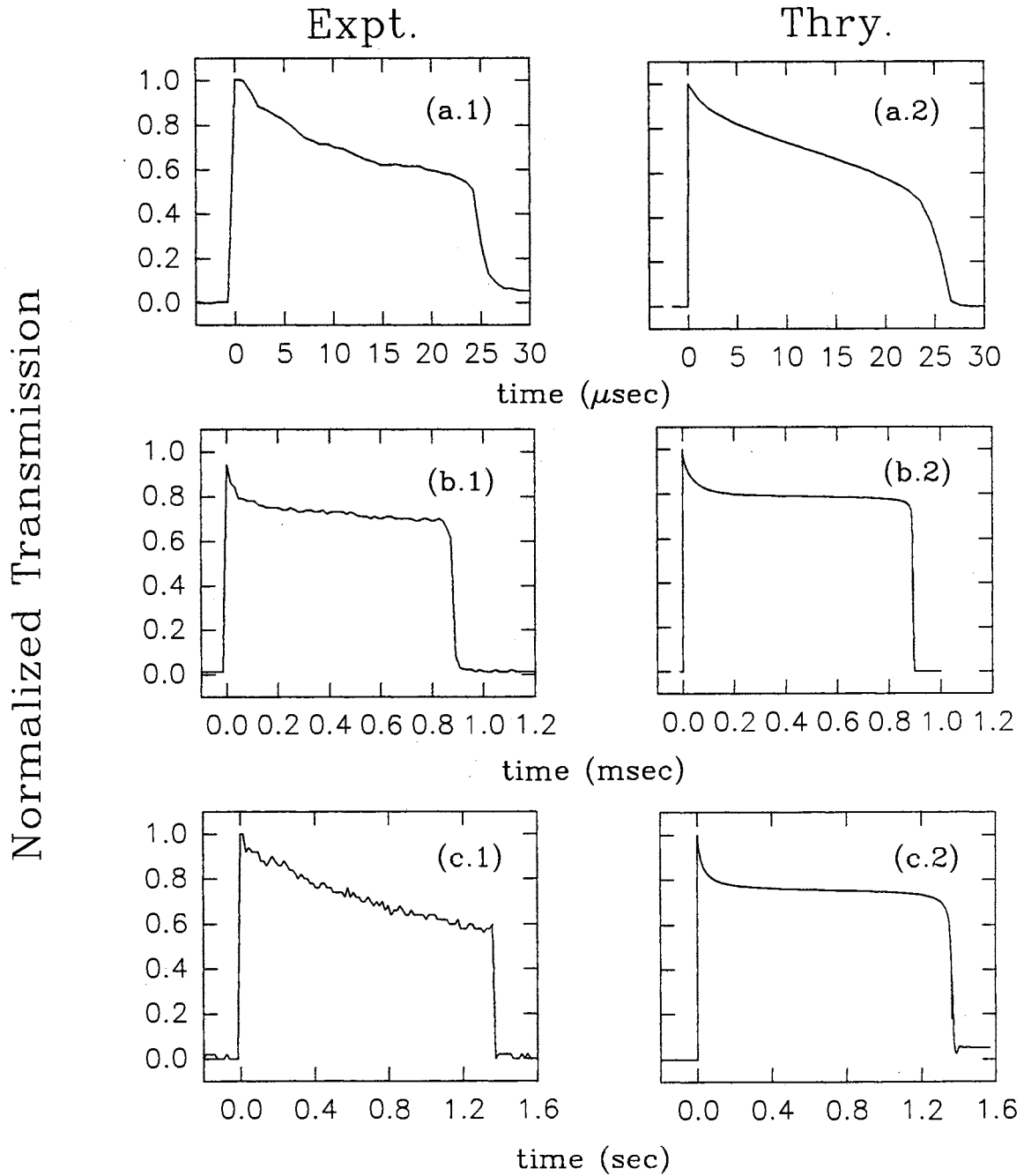


Figure 9. Normalized power transmission vs. time. The powers are (a) 640mW, (b) 470mW, (c) 330mW. The sample location,  $Z_{\text{samp}}$ , was theoretically determined to be (a.2) f-.17mm, (b.2) f-.2317mm, and (c.2) f-.18mm where  $f=5\text{cm}$ .

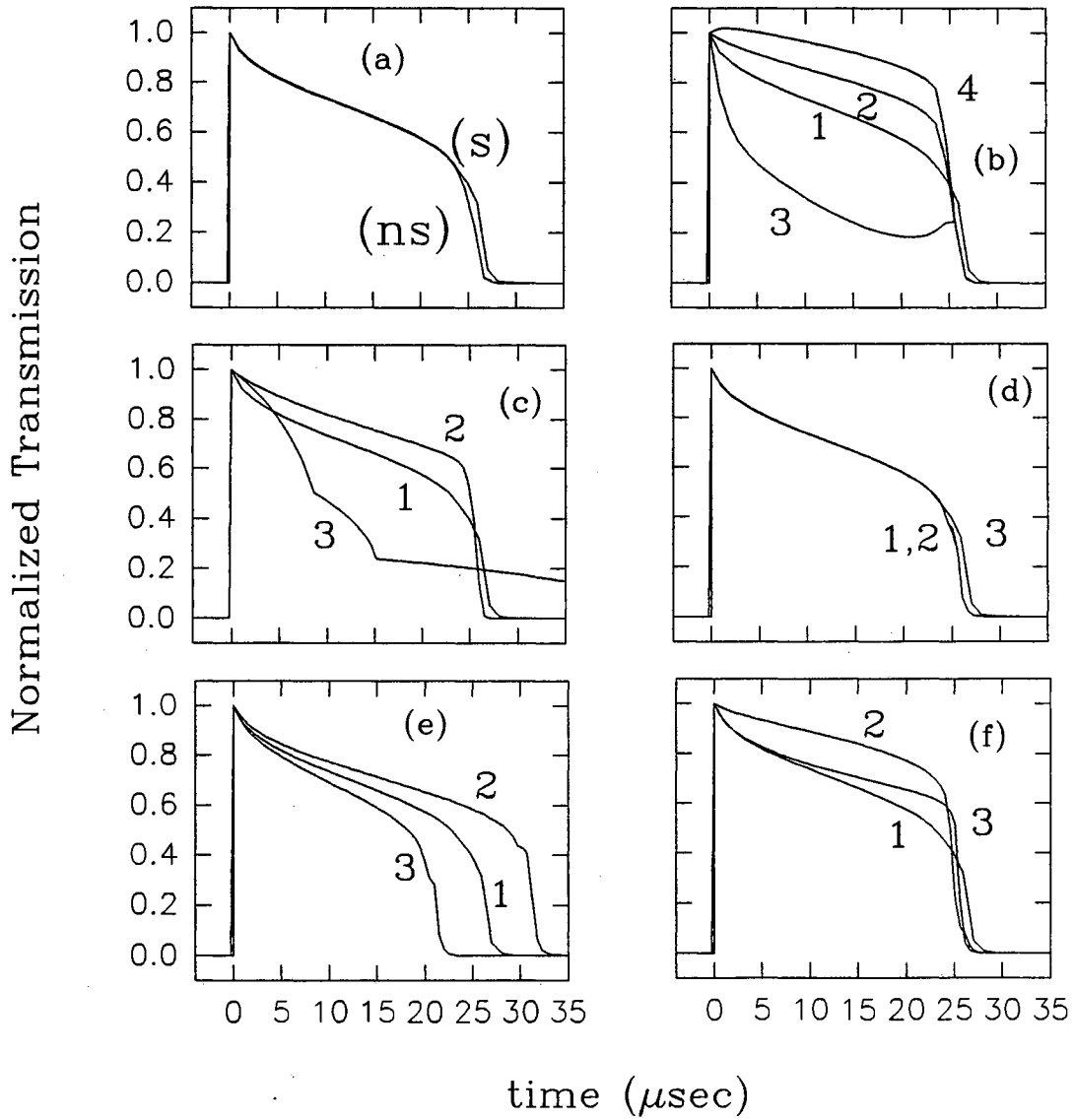


Figure 10. Absorptive switching characteristics as a function of (a) electronic dynamics, (b)  $dn/dT$ , (c) longitudinal and transverse heat diffusion, (d) ambipolar diffusion, (e) sample thickness, and (f) sample placement along the  $z$ -axis.

In Figure 10.(b) we show the effect of self-focusing. (b.1) assumes both the on-resonant and off-resonant contributions to the change in the index of refraction due to temperature changes (low e-h density). This is the case used to fit the data. (b.2) ignores both contributions, thus the diffraction here is solely due to the already present diffraction caused by the external focusing. (b.3) ignores the on-resonant term, which effectively gives a larger value for  $dn/dT$  and (b.4) simply reverses the sign of both terms. Interestingly it would seem the more positive the total  $dn/dT$  the less the transmission until the time of switching, however the time of switching still remains roughly the same.

Figure 10.(c) shows the effect of the heat diffusion terms. (c.1) contains both the longitudinal and transverse diffusion terms. In (c.2) we turn off the longitudinal heat diffusion term and in (c.3) we turn off the transverse heat diffusion. Due to the similarity amongst curves (c.1) and (c.2) in comparison to curve (c.3), one may conclude that heat diffusion transverse to the direction of beam propagation exceeds that along the direction of propagation. This is due to the fact that the temperature gradient is greater transverse to the beam than along the beam. The transmission profile of curve (c.3) is unique. Because there is no radial heat diffusion and negligible radial carrier diffusion, the temperature profile, and hence the absorption profile, follows that of the intensity profile. Thus the center portion of the intensity profile switches sooner than in the case of diffusion in all dimensions because of the heat confinement. In addition, the total transmitted power does not switch to zero spontaneously. The heat generated near the center of the beam is not shared with that portion of the beam outside this region. Thus initially only a finite portion of the beam completely switches, the remaining portion, extracting less energy from the beam, decays slowly.

In Figure 10.(d) we examine the effect of ambipolar diffusion. In (d.1) we have  $D_a = 10^{-4} \text{m}^2 \text{sec}^{-1}$ , in (d.2) we set the diffusion term to zero, and in (d.3) we raise  $D_a$  to  $10^{-3} \text{m}^2 \text{sec}^{-1}$ . Clearly the electronic diffusion term has little effect.

In Figure 10.(e) we show the effect of translating the sample along the optical axis. In (e.1) thru (e.3) we have that  $z_{samp}$  is equal to f-.17mm, f-.18mm, and f-.16mm respectively ( $f=5\text{cm}$ ). Clearly as the sample is moved closer to the focal plane the time of switching decreases. It would seem in comparing this figure with Figure 10.(b) that external focusing effects more the time of switching whereas internal self-focusing effects the overall structure.

Lastly in Figure 10.(f) we adjust the thickness of the sample from 1mm in (f.1), to 0.5mm in (f.2), to 2mm in (f.3). The position of the front face relative to the focusing lens is constant. (f.2) seems to rise above (f.1) similarly to how (b.2) is elevated from (b.1). Perhaps in the thinner sample self-focusing becomes less significant. (f.3) appears similar to (f.1) indicating that most of the dynamics are taking place towards the front portion of the sample, thus extending the back end has little effect.

In Figure 11 we show the time necessary for switching to take place as a function of input power at a fixed  $z$  value. The inset is a reproduction of the same graph using a common logarithmic scale for the vertical axis. The inset would seem to indicate two linear regimes. Thus the time of switching approximately decreases exponentially with power at a "rate" corresponding to the respective regime.

### Transverse Structures

Figure 12 illustrates theoretical beam profile calculations for transverse heat diffusion only (a), longitudinal heat diffusion only (b), and three dimensional heat diffusion (c). All three cases show the output intensity profile when their respective temporal profiles in Figure 10.(c) reach normalized power transmission values from 0.6 to 0.1. We observe that when either transverse or longitudinal heat diffusion is restricted only a local minima on axis results. This local minima (hole) forms at earlier transmissions in the case of no transverse heat diffusion compared to no longitudinal heat diffusion, further showing that heat diffusion in the transverse direction is greater than that along the beam path. Three dimensional heat diffusion is required to observe the formation of a local minima on axis (hole) followed

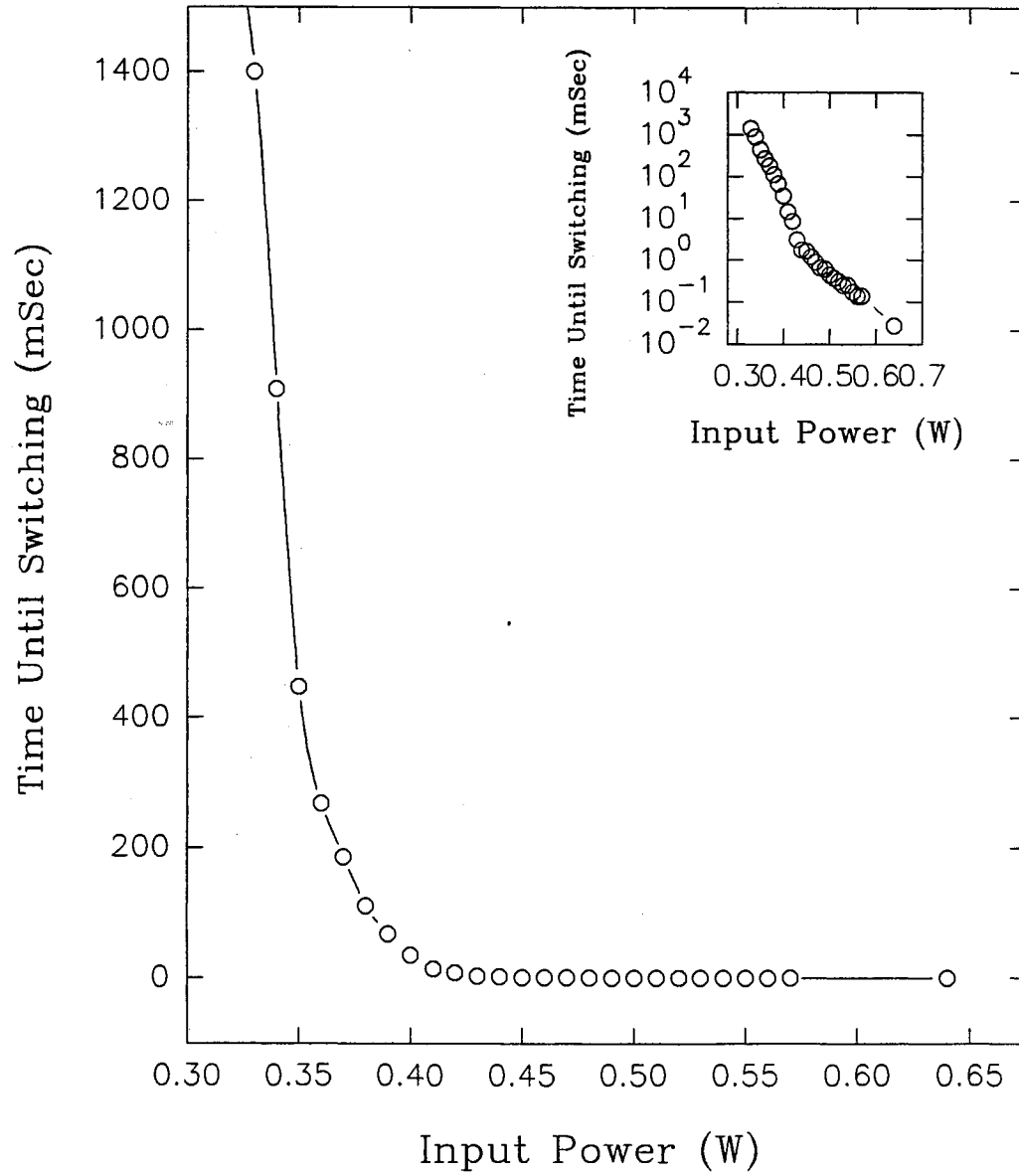


Figure 11. Time of switching as a function of input power.

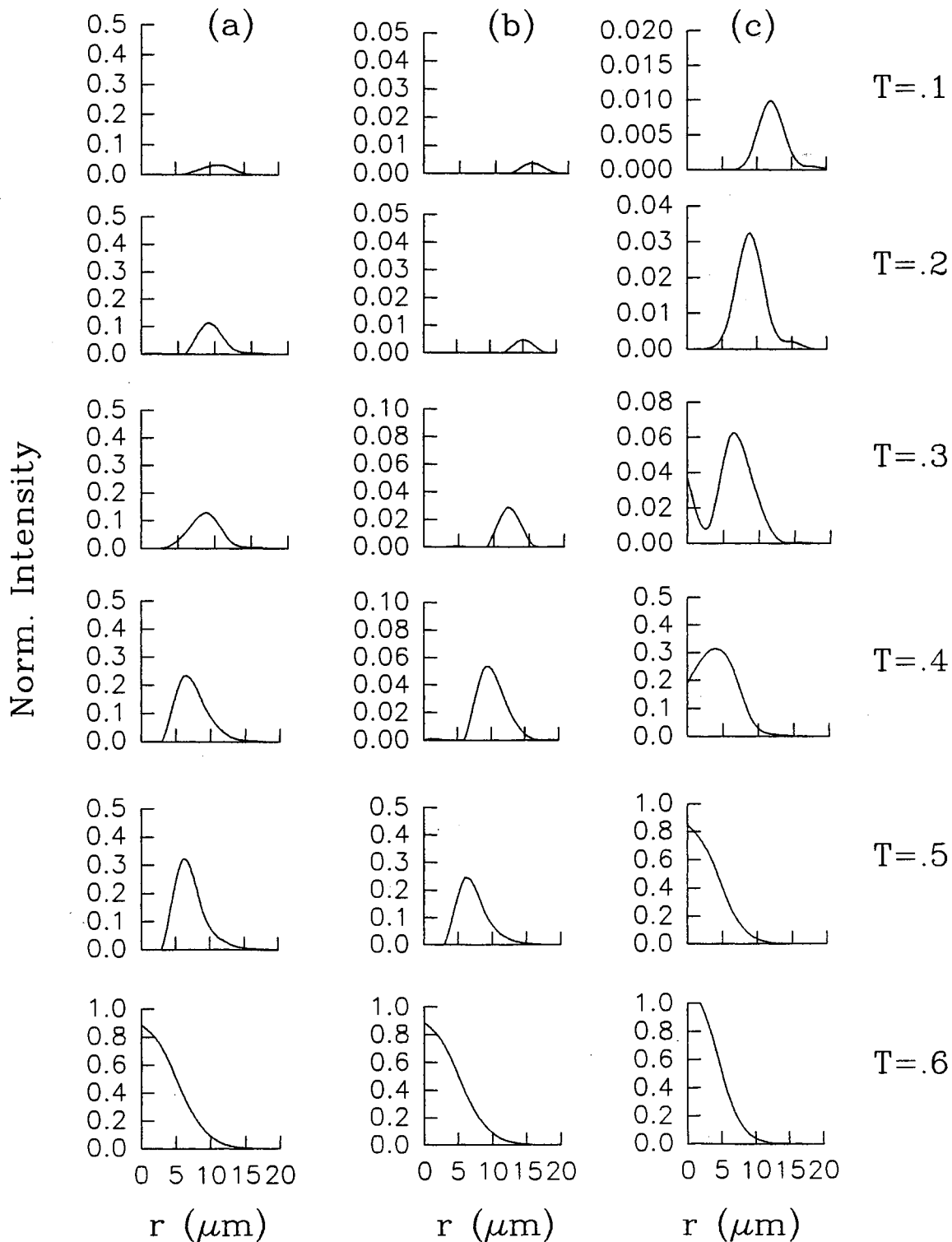


Figure 12. Output beam profiles during switching as a function of transmittivity and longitudinal and transverse heat diffusion. (a) no longitudinal heat diffusion, (b) no transverse heat diffusion, and (c) both longitudinal and transverse heat diffusion.

by a local maxima on axis and local minima off axis (rings). This resembles that of a switching wave in that the local minima begins on axis and propagates radially outward. Thus while Figure 10.(c) would seem to indicate that transverse heat diffusion dominates the dynamics, Figure 12 clearly shows the importance of longitudinal heat diffusion in the formation of these beam profiles.

Figure 13 illustrates the experimental far field beam profile measurements and the comparison with theory in the case of the long time scan, Figure 9.(c). Here only a cross sectional slice through the center (near azimuthal symmetry) is shown. The model utilizes the stationary (s) electron-hole density and three dimensional heat diffusion. The experimental power transmission was not measured simultaneously with that of the beam profile measurements, thus it is not exactly known at what normalized power transmissions these profiles were taken. However when comparing to the model we found good agreement at theoretical normalized power transmissions of 0.4 (c) and 0.38 (d). The experimental and theoretical results of Figure 13 show the very same structures as the computer simulation of Figure 12.(c), namely a hole followed by rings.

In Figure 14 we show the intensity throughout the bulk of the sample at six different transmittivities for the case of Figure 9.(a.2). The respective axes are the same for all graphs.  $Z=0$  represents the front face while  $Z=1\text{mm}$  represents the exit face. Initially the beam is focused near the rear of the sample (a). In (b)-(f) the sample is switching to its off-state. A number of interesting structures result. Quite clear is the appearance of self-focusing already present in (b). One can observe an increase in the on-axis intensity and a narrowing of the beam "width". This self-focusing also gives rise to undulations in the beam "width" clearly identifiable in (c). In (d)-(e) one can see the ring and hole structures throughout the bulk of the sample. At this higher power multiple rings result. Such structures have previously been theoretically predicted[35]. And lastly one can see from (d)-(f) the gradual localization of the beam at the front face. As a final note, beam profile calculations were carried out in previous work[36] whereby all diffraction was ignored. There

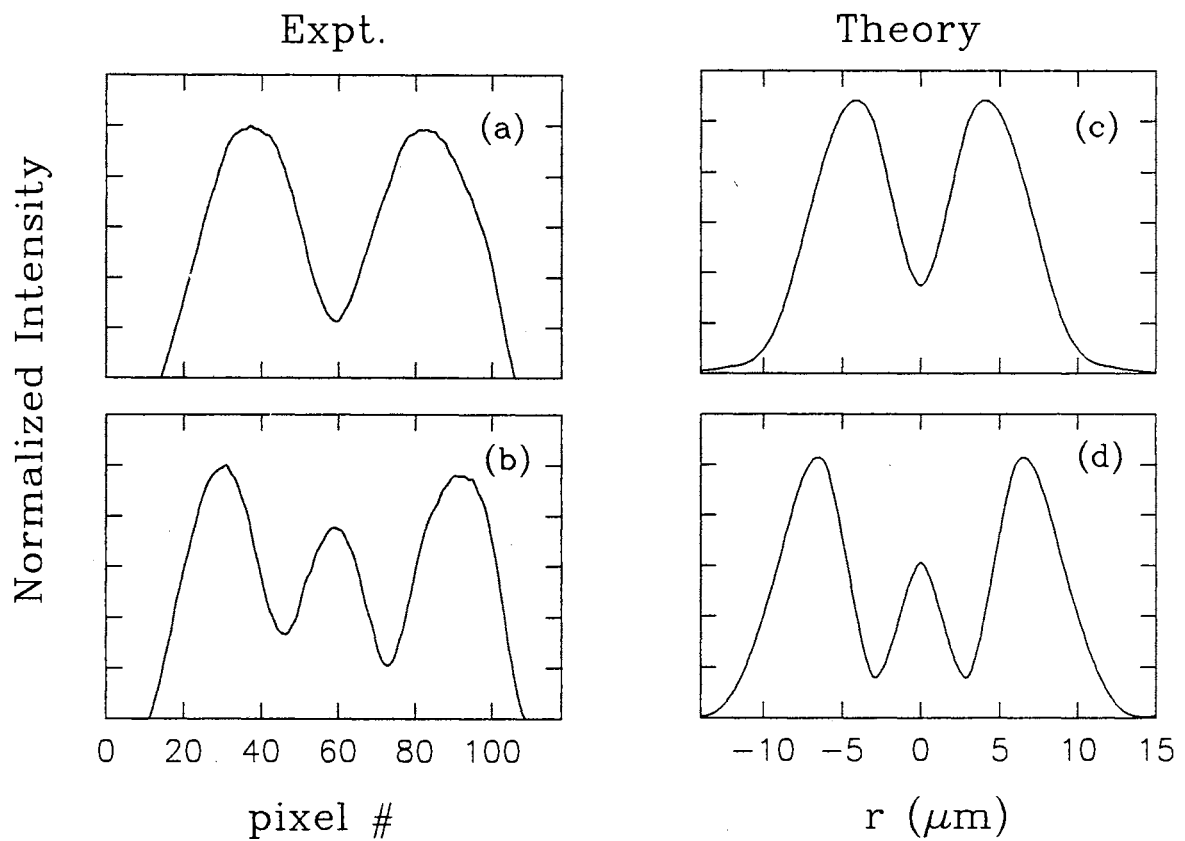


Figure 13. Experimental and theoretical beam profiles at transmittivities of 0.4 (top) and 0.38 (bottom)



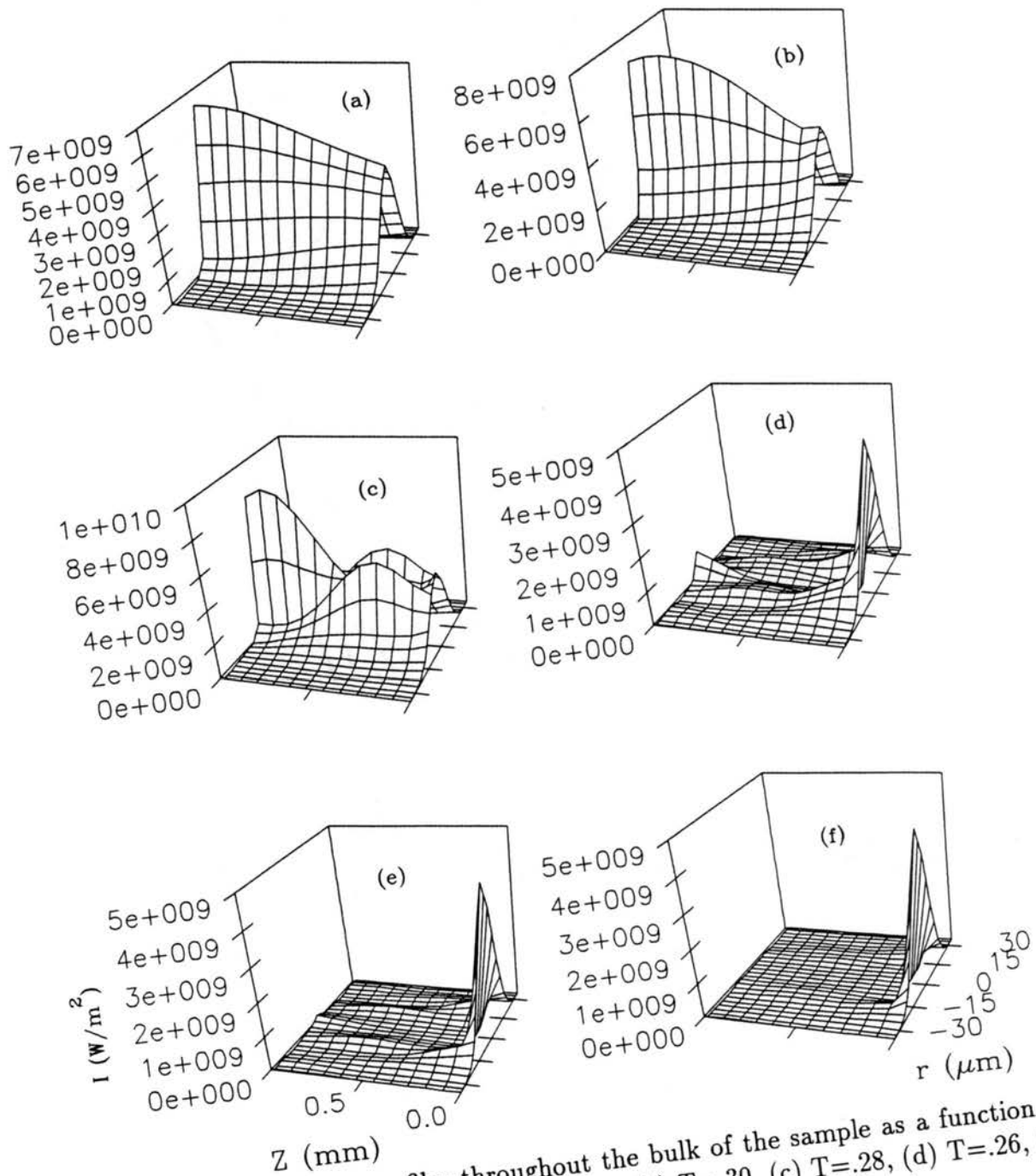


Figure 14. Intensity profiles throughout the bulk of the sample as a function of transmittivity,  $T$ . (a)  $T=1.0$ , (b)  $T=.30$ , (c)  $T=.28$ , (d)  $T=.26$ , (e)  $T=.15$ , and (f)  $T=.10$

the single hole and ring type structures occurred on all power and time scales. Thus diffraction is essential to the further development of multiple ring formation.

In Figure 15 and Figure 16 we similarly show the temperature and e-h density profiles respectively. In these figures we can see the formation and localization of an excitation domain at the front face. Without any additional relaxation mechanism the result is a runaway process. Here the temperature soars well beyond the melting point ( $\sim 1700\text{K}$ ) and extremely high e-h densities result. With such levels of excitation a highly complex nonlinear problem at the surface surely results. In all samples the resulting damage appeared at the surface. It would seem plausible that such excitation localization would be responsible.

### Regenerative Pulsations

A very interesting phenomenon has been observed in a few samples. Perhaps the most vexing consideration in attempting to understand this phenomenon is 1) it only occurs in a single batch of our samples and 2) the data was rarely consistent, thus trends and dependencies on controllable parameters were difficult to identify. This phenomenon, known as regenerative pulsations, seems to possess a great deal of structure. That is the character of the pulsing seems to be highly varied and not always reproducible. The absorption spectra, and this spectra as a function of temperature were identical amongst the various samples investigated. Their thicknesses were the same. Their bulk thermal properties were specified to be the same. All samples were grown by the Seeded Vapor Phase Transport (SVPT). All samples had been similarly polished and none were etched. Experimentally, the absorptive switching characteristics were the same. The only difference is that in some samples the material immediately damaged following the switching to the off-state whereas in one particular batch of samples the material would switch to an off-state and then self-pulse for a period of time and then damage. Because of the time scale of this phenomenon it seems the effect must be thermal in nature. That is the effect must be a function of the heating and cooling rates throughout the sample.

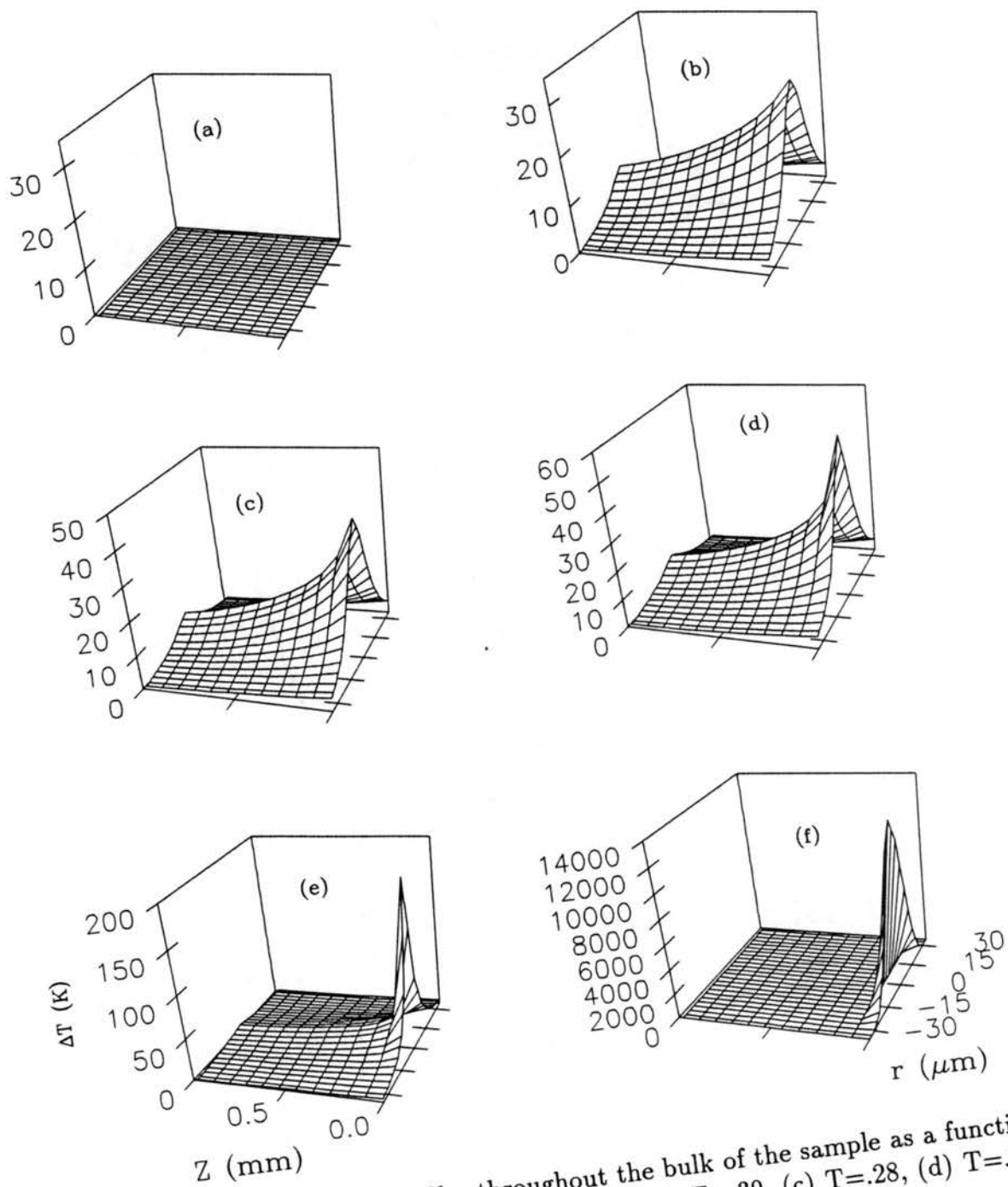


Figure 15. Temperature profiles throughout the bulk of the sample as a function of transmittivity,  $T$ . (a)  $T=1.0$ , (b)  $T=0.30$ , (c)  $T=0.28$ , (d)  $T=0.26$ , (e)  $T=0.15$ , and (f)  $T=0.10$

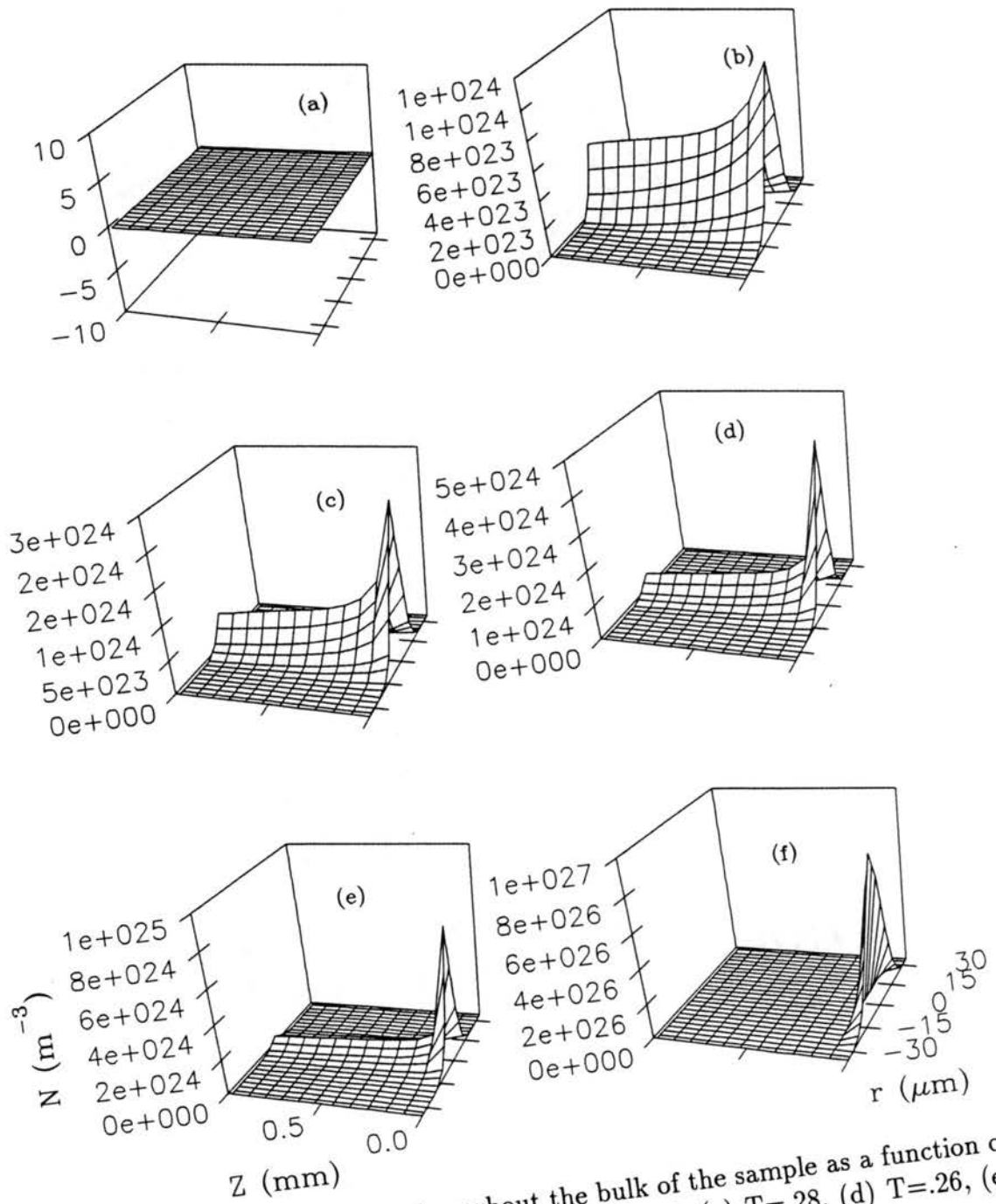


Figure 16. e-h density profiles throughout the bulk of the sample as a function of transmittivity,  $T$ . (a)  $T=1.0$ , (b)  $T=.3$ , (c)  $T=.28$ , (d)  $T=.26$ , (e)  $T=.15$ , and (f)  $T=.10$

Several hybrid studies of regenerative pulsations have been reported in the literature[37–42] These experiments utilized a piezoelectric Fabry-Perot cavity. Regenerative pulsations have also been seen in intrinsic bistable systems by some workers[43,44,37]. However these intrinsic forms of regenerative pulsations are all dispersive in nature, requiring some form of cavity resonance, and thus could not explain our results (absorptive bistability). Only the work by Stadnik[11,12] is similar to our results. There they see similar structures in bulk ZnSe utilizing an equivalent excitation source and experimental geometry. However these results lack any quantitative theory. The qualitative explanation is based on the concept of excitation domains and their unstable propagation. Some collaborative theoretical work[13,10,14,46–49] has been reported and essentially involves the calculation of hysteresis phenomenon, excitation domains, and domain structure and velocity. Although such theories may apply, without a direct simulation and comparison amongst theory and experiment, it is unclear.

Perhaps the easiest means of understanding what is meant by regenerative pulsations is offered by Figure 17. The experiment is identical to that used in the previous sections (Figure 2). In figure 17.(a) we show the normalized transmission as a function of time. Below in Figure 17.(b) we show the simultaneous normalized reflection ( $P=375\text{mW}$ ). Because there is no obvious phase difference we conclude that the regenerative pulsations are indeed a form of absorptive bistability as opposed to dispersive bistability. As mentioned the structure of these pulses varies. Some appear more square top shaped as in Figure 18.(a) while others more saw-tooth in character, as in Figure 18.(b). Experimentally both structures may result without any modification to the apparatus. Thus it was very difficult to identify trends. In addition to this anomaly it was difficult to predict how many after pulses would occur. After some unforeseen number of pulses the material would damage. Thus while trying to identify trends, one would have to occasionally translate the sample transverse to the beam. This also effected the experimental results. Merely thumping the sample mount would effect the results. Using a 3.5cm focusing lens as opposed to a 5cm focusing lens, extremely clear square top pulses result (Figure

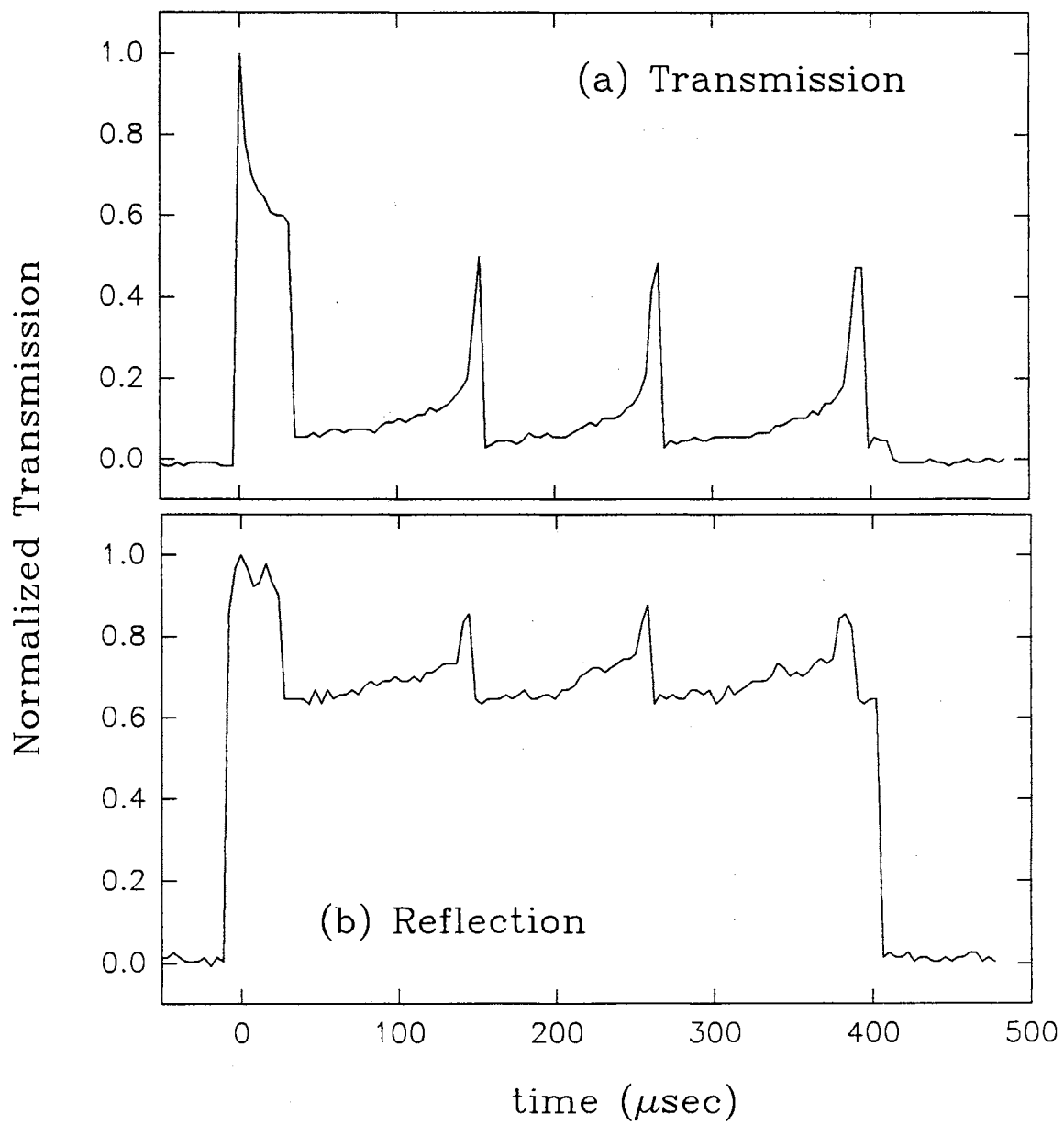


Figure 17. Normalized transmission and reflection showing regenerative pulsations.

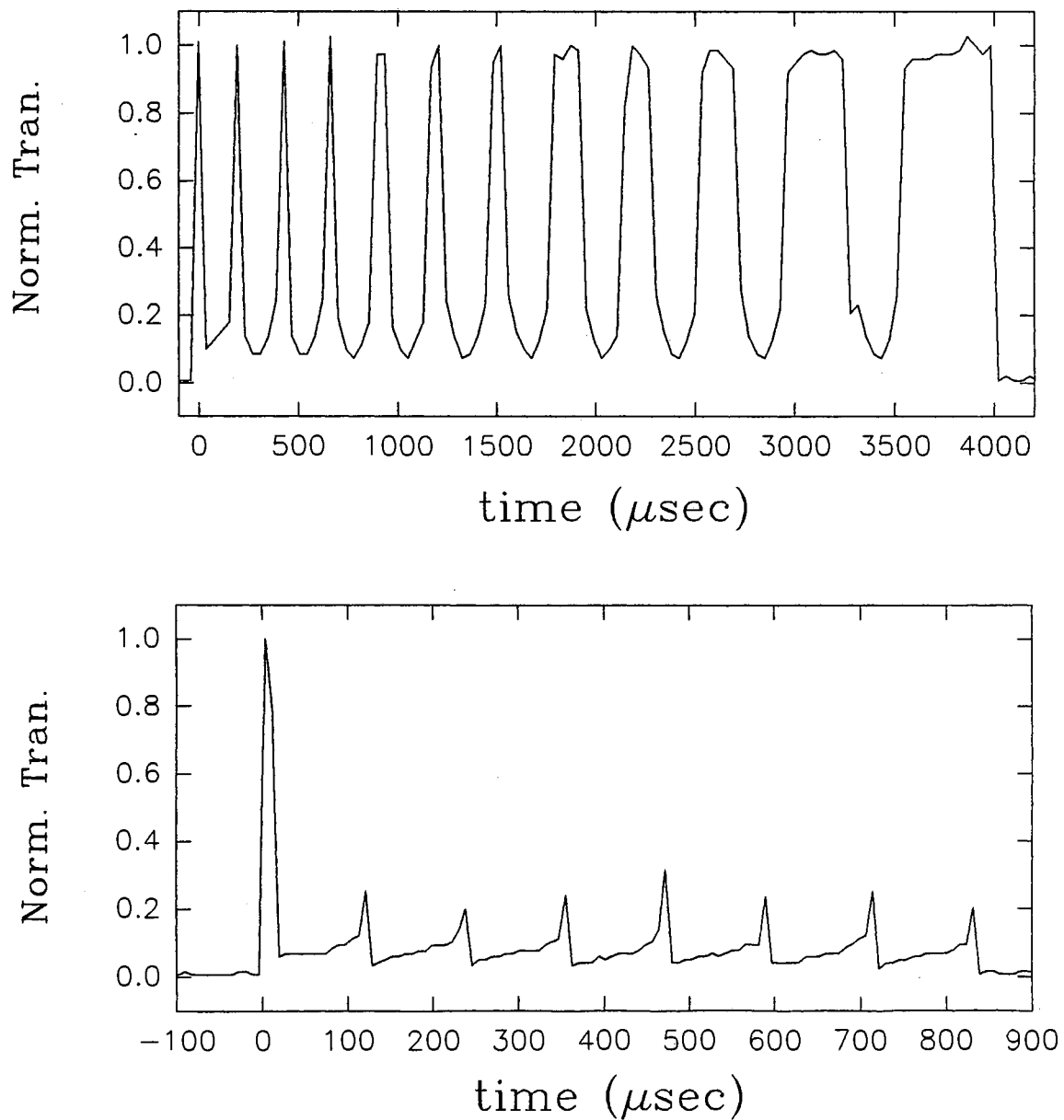


Figure 18. Two examples of regenerative pulsations showing the two forms of pulsing structures. Square top (top, 430mW) and sawtooth (bottom, 510mW).

19). (Here the power used is 430mW). It would seem the square top structures favor a tighter focusing geometry. Using a 10cm focusing lens and the range of power available, regenerative pulsations never occurred.

Briefly summarizing the most significant parameters responsible for the appearance and structure of these pulses seems to be 1) focusing geometry. There had to be sufficient fluence and proper diffraction. Thus power, beam size, time, and focusing were all important. 2) Sample homogeneity. Translating the sample perpendicular to the beam effected the results. 3) Hysteresis. The sample did not always respond the same at the same location. 4) The sample properties themselves. Not all samples reveal such pulsing and the phenomenon is seemingly rare in the scientific literature.

By computer simulation it seems that the effect is essentially a surface problem. That is, the effect occurs due to some relaxation of the thermal domain at the surface. We have theoretically simulated regenerative pulsations by stipulating that at the front surface there is a reduced heating effect. Numerically this is accomplished by reducing the forcing function for the temperature by a factor of 12. The forcing function is,

$$F_T = q_{eff} \frac{N\hbar\omega}{\tau k_{th}} \quad (121)$$

The inhomogeneity at the surface results in many dangling bonds which manifest themselves as a tremendous perturbation in the band structure. Essentially the band gap is replaced by a near continuous distribution of states[50]. Any change in  $q_{eff}$  and  $\tau$  would most likely be an increase in  $q_{eff}$  and a decrease in  $\tau$ . The thermal conductivity could increase or decrease but certainly not increase by a factor of 12 (from a bulk value of  $5.6\text{Wm}^{-1}\text{K}^{-1}$ ). The only other parameter is the e-h density. It was shown earlier that the ambipolar diffusion coefficient had little effect on the switching and furthermore an increase in  $D_a$  by a factor of 10 did not reveal any self-pulsing. The forcing function for the e-h density is proportional to the absorption coefficient. Perhaps some form of saturation (band-filling or dynamic Burnstein-Moss effect) causes a reduction in the absorption however all attempts to include such a mechanism failed. In any case, the net outcome is to bring the



heating and cooling rates into close competition resulting in thermal waves at the surface. These thermal waves modulate the absorption coefficient and the index of refraction. This causes the intensity, and hence heating rate, to undulate. In Figure 20 we compare the experiment with theory. The arrows in the theoretical scan are used as markers related to the three following figures. Some features compare quite convincingly. (The "fingernail" like spikes impressed on the individual pulses in the theoretical scan, as well as the noise following the initial switching to the off-state, are believed to be a numerical manifestation.) Figures 21,22, and 23 show the (radial) intensity, temperature, and e-h density profiles respectively as a function of time at the surface (or rather within the first hypothetical "slice" of the sample). The time period corresponds to the region between the arrows in Figure 20. Obviously under such high excitation very complex structures result. The intensity profile clearly shows the undulations present across the entire beam, as do the temperature and e-h density profiles. It is the network of feedback amongst the intensity, heating/cooling, absorption, and diffraction responsible for this interesting competition amongst heating and cooling. Beyond this first slice the excitation is much reduced however these complex structures continue to deform due to the effects at the surface layer.

Figure 24 shows the results of the side-beam experiment (refer to Figure 2). The top figure shows the incident (square pulse) and transmitted signals (both along the optical axis). Below are the incident pulse (same as above, along the optical axis) and the side beam (transverse to the optical axis). The side beam is at a wavelength of 543.5nm, well below the band edge. The change in absorption at this wavelength is negligible thus any changes in its propagation will be detected by the deflection of its beam path, hence the use of the iris. As the transmitted signal switches to the off-state and subsequently pulses, the side beam steadily rises. Qualitatively this may be understood as follows. Initially the side beam is incident upon the iris slightly to its right side, thus not at the maximum transmittivity. The incident beam comes to focus near the rear of the sample while the side beam traverses roughly through the middle. The two beams cross in the interior. As the

switching takes place a temperature gradient forms such that the front portion of the sample (along the z-axis) is at a greater temperature than the back portion. The subsequent refractive index gradient steers the side beam towards the center of the iris steadily increasing the transmission. During the pulsing a region localized at the front face steadily rises in temperature. When the incident  $\text{Ar}^+$ -ion beam turns off the middle portion of the sample readily cools and the side beam is steered back towards the right side of the iris reducing for a moment the transmission. The strong excitation domain at the surface now begins to diffuse throughout the bulk of the sample. As this heat traverses the side beam a steering of the side beam towards the center of the iris again occurs and the transmission rises for a period before again descending as the sample state approaches equilibrium. The important observation is that the pulsing mechanism would appear to exist at the surface, as opposed to some process occurring throughout the bulk. This is evidenced by the lack of any modulation in the side beam transmission during the pulsing.

### Conclusion

We have presented experimental and theoretical evidence of absorptive switching, transverse structures, and regenerative pulsations in bulk ZnSe. By using the Kramers-Kronig transformation we have been able to calculate the effect of temperature and e-h density on the resonant enhancement of the refractive index as the absorption spectra is altered. Utilizing Urbach's rule for the absorption, three dimensional spatial as well as time dependent transport equations, and a numerical scheme for solving this system of equations, we have been able to simulate the effect of longitudinal and transverse heat diffusion, ambipolar diffusion, self-focusing due to background as well as on-resonant contributions, sample thickness and location, and lastly the effect of a nonstationary e-h density. We have also been able to simulate the 3-dimensional profiles of the governing variables throughout the bulk of the sample. From this we see the formation of hole and ring type structures at relatively low power (330mW) and slow time scale ( $\sim$

1sec) and multiple rings, as well as further complex structures at a higher power (640mW) and shorter time scale ( $\sim \mu\text{sec}$ ). The bistable property of our system manifests itself through the positive feedback amongst the absorption and heating mediated by the production and radiationless recombination of electron-hole pairs. However in the case of regenerative pulsations, it would seem some form of thermal relaxation is necessary. We have simulated such pulsing by unjustifiably reducing the heating rate at the surface. This phenomenon still has many questions.

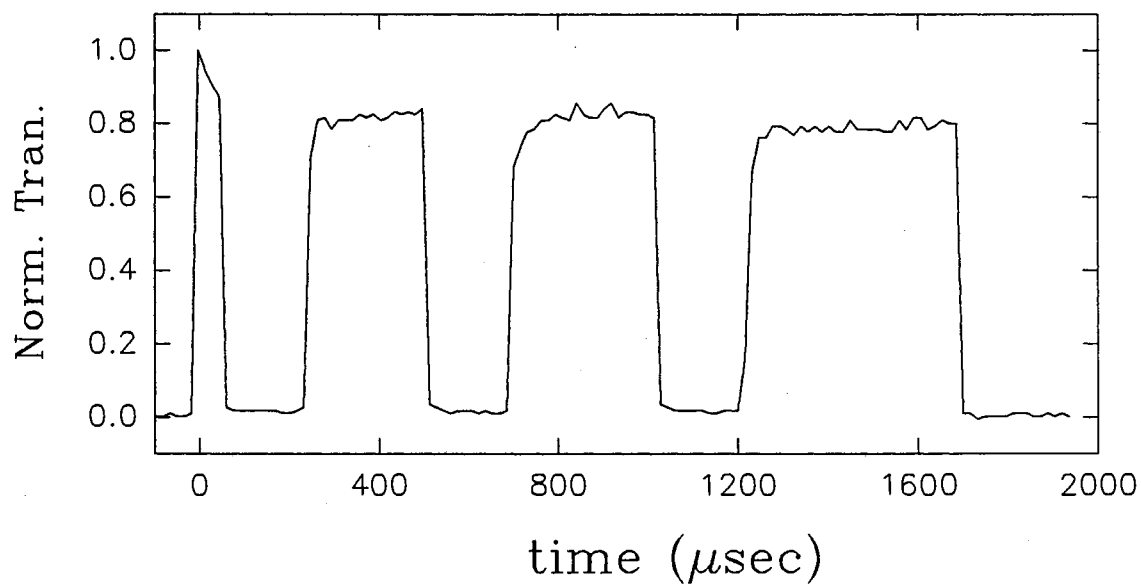


Figure 19. Example of regenerative pulsations using a 3.5cm focal length lens.

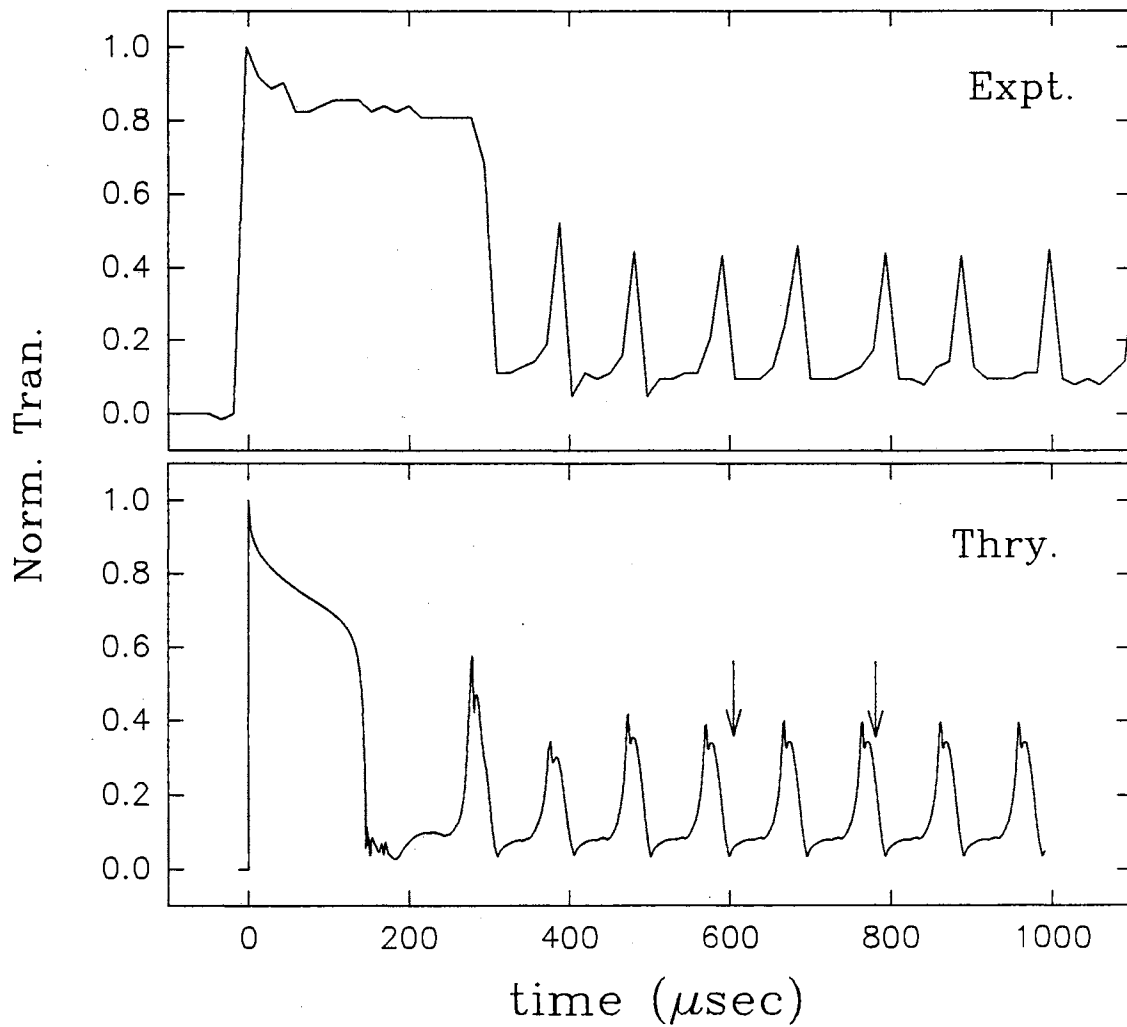


Figure 20. Experimental regenerative pulsations (top) and theoretical simulation (bottom). The arrows serve as markers for Figures 21, 22, and 23. The power is 430mW and  $Z_{\text{samp}}=f\text{-}175\text{mm}$ .

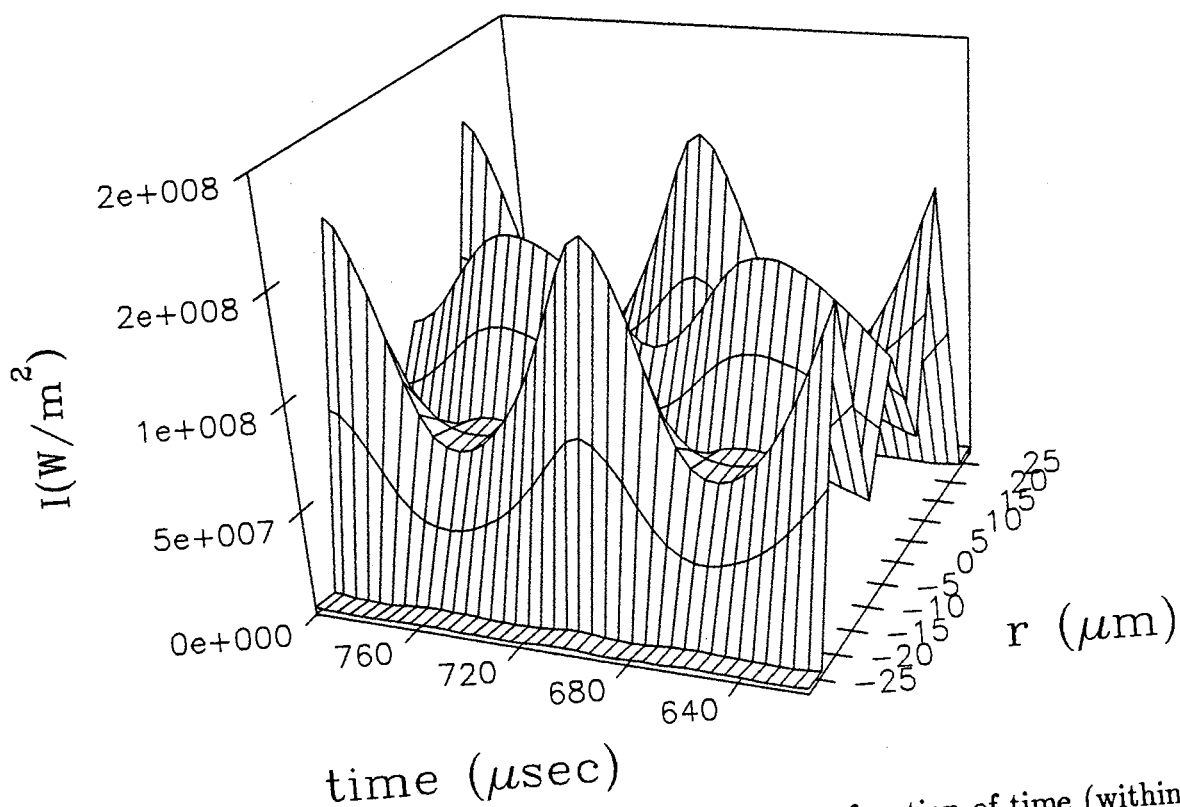


Figure 21. (Radial) intensity profile at the surface as a function of time (within arrow markers in Figure 20).

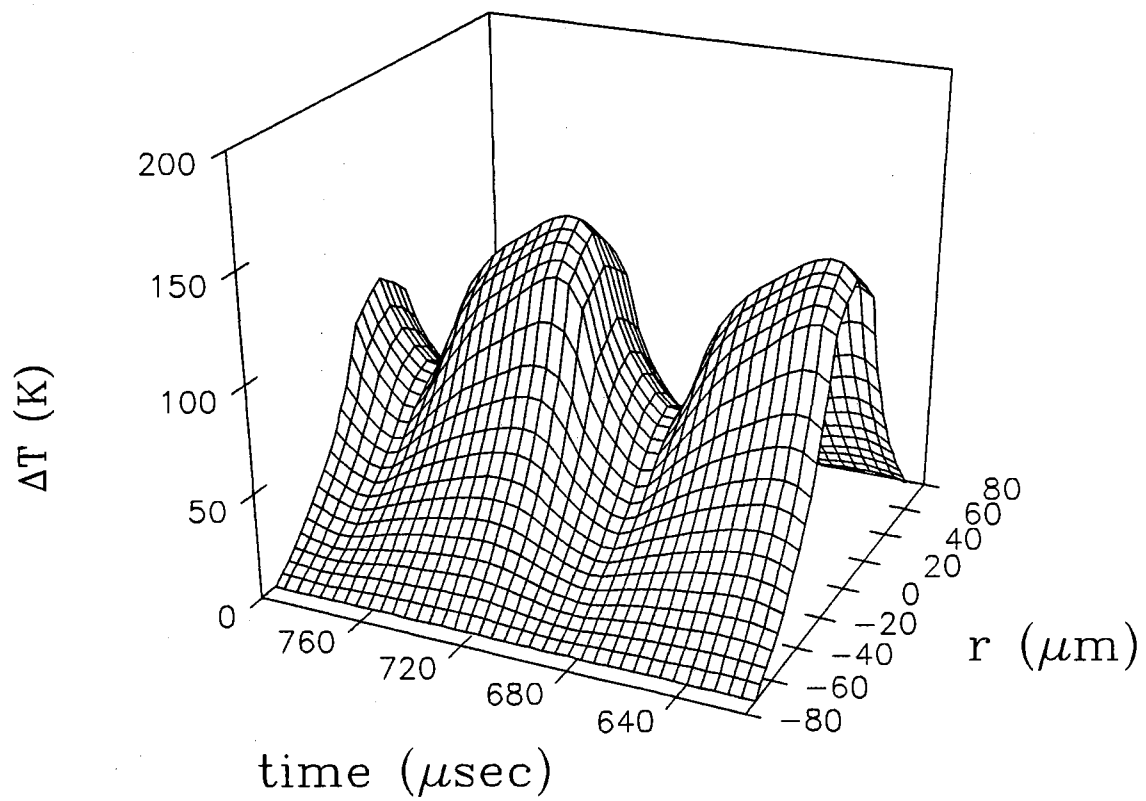


Figure 22. (Radial) temperature profile at the surface as a function of time (within arrow markers in Figure 20).

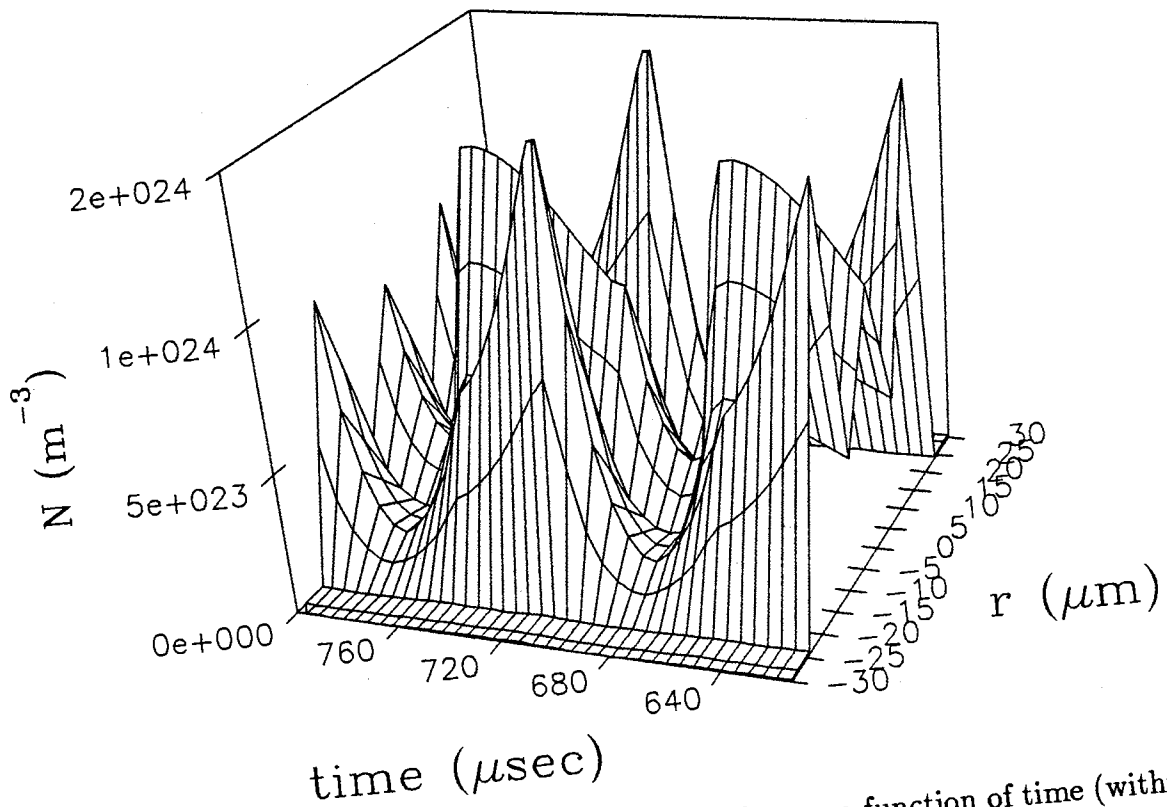


Figure 23. (Radial) e-h density profile at the surface as a function of time (within arrow markers in Figure 20).



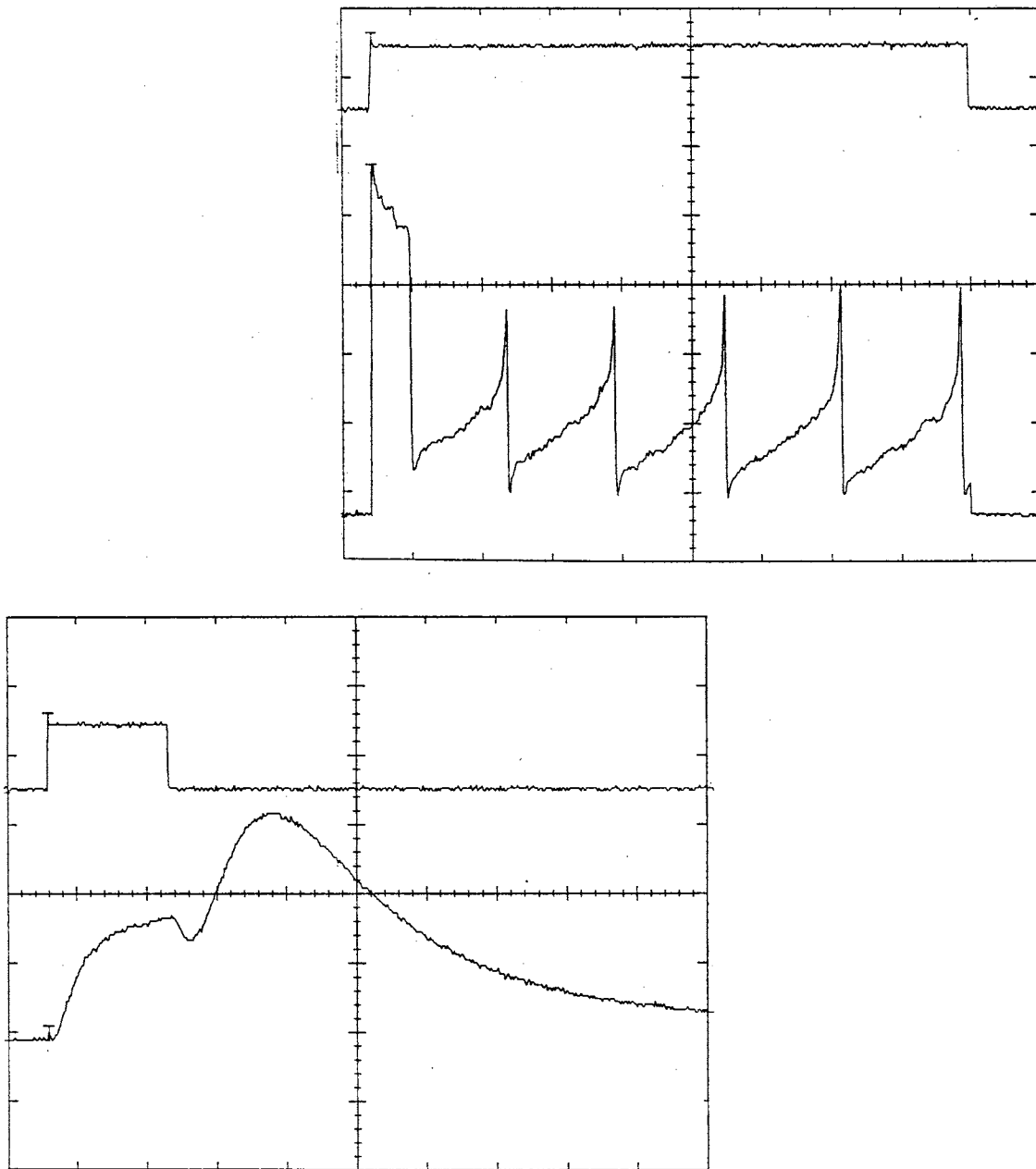


Figure 24. Results of side beam experiment. (top) Incident exciting beam (square pulse) and transmitted exciting beam. (bottom) Incident exciting beam (square pulse) and side HeNe beam.

## CHAPTER III

### THERMAL LENSING IN A LEAD SILICATE

#### GLASS

##### Introduction

The trapping of a laser beam due to self-induced changes in the index of refraction is known as self-focusing and is a phenomenon of which has been studied extensively for over two decades[55,56]. This effect has been observed in a variety of optical materials[57-59,61-69] When this change in the refractive index is due to a change in the local temperature then it is referred to as thermal lensing. Thermal lensing has been studied in a great number of optical glasses[62-65,67]. Extensive research has been collected concerning this phenomenon, most of which applies to the effect of self-focusing on the propagation characteristics of laser light and the various mechanisms responsible for this effect. Our aim has been to study the relative strength of the thermal lensing effect in a variety of optical glasses[70]. Of these materials, we only report here the results for a lead oxide modified silicate glass with the following constituents: 57% SiO<sub>2</sub>, 34% PbO, 5% Eu<sup>3+</sup>, and 3.3% BaO. Similar experiments are carried out using a 10msec square pulse at 514nm and a ~ 10nsec gaussian pulse at 532nm. The effect of sample thickness is also discussed. Two types of measurements using the same experimental setup were taken. The first measurement involves the output vs. sample location, or Z-scan. The second is simply output vs. input with the sample location being fixed. For the nanosecond experiments the output and input are expressed as fluence whereas for the millisecond experiments these are normalized transmittance and power respectively. As will become clear later, the Z-scan enables us to see at what location the thermal lensing is greatest whereby the second type of measurement

allows us to see the effect of the lensing on the transmittance characteristics of the output.

On the millisecond time scale the beam undulates within the sample. This is predictable from the ray tracing theory of quadratic index media[77] and has been investigated early on by Dyshko et. al.[71,72], Kerr[61], Zverev and Pashkov[67], Fiet et. al.[72,73,20],Wagner et. al.[21], and more recently for GRIN lenses[74] and laser crystals such as Nd:YAP[75,76]. These studies primarily focus on the characteristics of wave propagation in such media, catastrophic self-focusing, and filament formation. These references are consistent in identifying beam waist undulations. Finally we point out that it has been our attempt to study the effects of self-focusing in order to understand its potential as a light controlling mechanism in these lead silicate glass materials.

#### Thermo-optic Effect

The change in the index of refraction is approximated (to first order) as that solely due to the thermo-optic effect,

$$n = n_o + \frac{dn}{dT} \Delta T \quad (122)$$

where  $n_o$  is the background index of refraction,  $\Delta T$  the change in temperature, and  $dn/dT$  is the total change in the index of refraction with temperature. Any nonlinearities resulting from thermal expansion have been omitted due to their negligible contribution in these lead glasses[70]. The change in temperature arises from the absorption of light energy and is governed by the heat diffusion equation. Ignoring any diffusion along the optical axes, in 2-dimensions the heat diffusion equation is,

$$\frac{1}{\eta} \frac{\partial T(\vec{r}, t)}{\partial t} = \nabla^2 T(\vec{r}, t) + 4\pi Q(\vec{r}, t) \quad (123)$$

where  $\eta$  is the thermal diffusivity,  $T$  the temperature, and  $Q$  the heat source. Using the following Green's function,

$$G(\vec{r}, t; \vec{r}', t') = \frac{1}{4\pi(t-t')} \exp \left[ -\frac{|\vec{r} - \vec{r}'|^2}{4\eta(t-t')} \right] \quad (124)$$

we find the change in temperature at time  $t$  and position  $r$  to be[78],

$$\Delta T(\vec{r}, t) = \int_0^t \int_0^\infty \int_0^{2\pi} \frac{\exp\left[-\frac{|\vec{r}-\vec{r}'|^2}{4\eta(t-t')}\right]}{(t-t')} Q(r', t') r' dr' d\varphi' dt' \quad (125)$$

The forcing function  $Q(r', t')$  is written as,

$$Q(r', t') = \frac{I(r', t')\alpha}{k_{th}} = \frac{2\alpha}{\pi w^2 k_{th}} \exp\left[-\frac{2r'^2}{w^2}\right] P_o(t') \quad (126)$$

where  $\alpha$  is the coefficient of linear absorption,  $k_{th}$  the thermal conductivity,  $w$  the beam waist size, and  $P_o(t')$  the peak power at time  $t'$ .

In our experiments we have used a 10msec square pulse derived from an Ar<sup>+</sup>-ion laser and acousto-optic modulator (AOM) and a  $\sim$  10nsec gaussian pulse from a pulsed YAG laser. The form of the forcing function is dependent on the temporal profile of the exciting pulse. In the case of the square pulse the peak power is merely a constant,  $P_o(t') = P_o = \text{constant}$ . Figure 25 shows the peak power of a cross-sectional slice versus time for the 10nsec pulse. Because a closed analytical solution is not possible for the case of a gaussian temporal profile we have approximated the gaussian by two linear equations (dashed triangle in Figure 25). At  $t = t_o$  the pulse reaches its peak power. We thus have for its temporal profile the following expressions,

$$P(t') = \begin{cases} \frac{P_o t'}{t_o} & , t' \leq t_o \\ P_o \left(2 - \frac{t'}{t_o}\right) & , t_o \leq t' \leq 2t_o \end{cases} \quad (127)$$

Using the above expressions for the temporal profiles in the expression for the forcing function Eq.126, solving for the temperature Eq.125 with the parabolic approximation, and using Eq.122 one arrives at the following expressions for the index of refraction,

10msec square pulse:

$$n(r, t) = n_o + \frac{dn}{dT} \frac{P_o \alpha}{k_{th}} \left[ \ln\left(1 + \frac{t}{t_c}\right) - \frac{2r^2}{w^2} \left(\frac{\frac{t}{t_c}}{1 + \frac{t}{t_c}}\right) \right] \quad (128)$$

10nsec triangular pulse:

$$n(r, t) = n_o + \frac{dn}{dT} \frac{P_o \alpha}{k_{th}} \left\{ \frac{t}{t_o} + \frac{t_c}{t_o} \ln\left(1 + \frac{t}{t_c}\right) - \frac{2r^2 t_c}{w^2 t_o} \left[ \ln\left(1 + \frac{t}{t_c}\right) - \frac{\frac{t}{t_c}}{1 + \frac{t}{t_c}} \right] \right\} \quad (129)$$

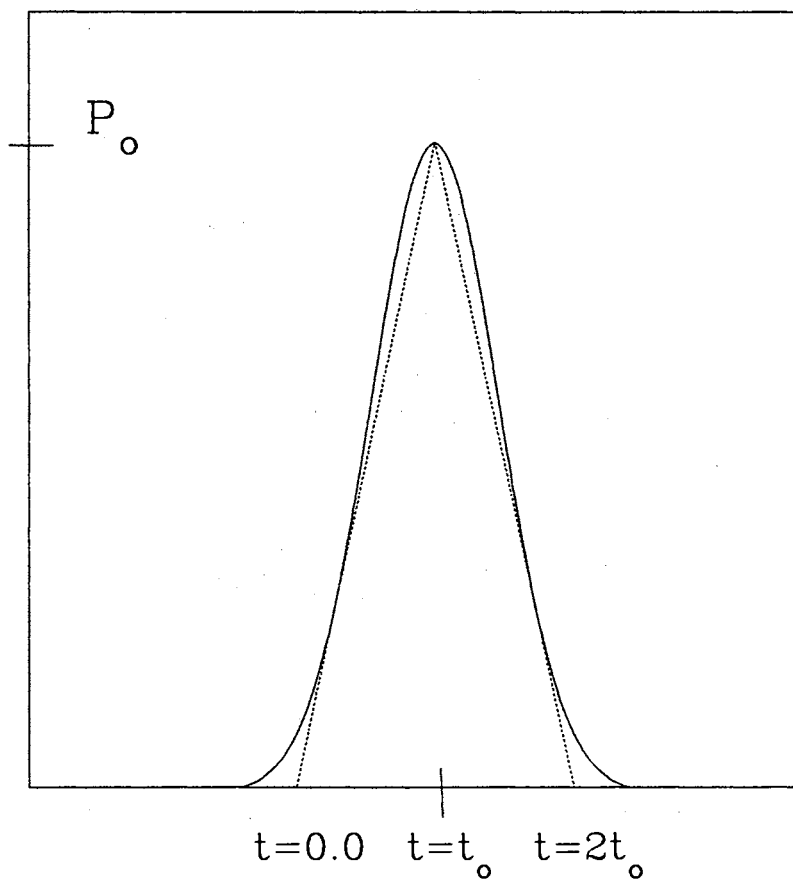


Figure 25. Triangular approximation to YAG pulse.

for  $t < t_o$  and,

$$n(r, t) = n_o + \frac{dn}{dT} \frac{P_o \alpha}{k_{th}} \left[ 2 - \frac{t}{t_o} + \left( 2 + \frac{t_c}{t_o} \right) \ln \left( 1 + \frac{t}{t_c} \right) - \frac{4r^2}{w^2} \left( \frac{t - t_o}{t + t_c} \right) \right] \quad (130)$$

for  $t > t_o$ . In the above expressions,  $t_c = \frac{w^2}{8\eta}$  and  $\frac{t_o}{t_c} \ll 1$ . Collecting terms for either Eq.128 or Eq.129 one can write the index of refraction as,

$$n(r, t) = n_3(t) - n_4(t)r^2. \quad (131)$$

### Gaussian Beams in Quadratic Index Media

Following the development by Kogelnik[79], the propagating characteristics of an electric field in an isotropic charge-free medium is governed by the wave equation,

$$\nabla^2 \vec{E} + k^2(r) \vec{E} = 0 \quad (132)$$

where by arriving at Eq.131 the fractional change in the index of refraction over one optical wavelength is assumed negligible. From Eq.131  $k^2$  is given by,

$$k^2(r) = n^2(r)k_o^2 = k_o^2(n_3^2 - 2n_3n_4r^2 + n_4^2) \approx k_o^2(n_3^2 - 2n_3n_4r^2) \quad (133)$$

where  $k_o = \frac{2\pi}{\lambda_o}$ .

In reference to the development in Kogelnik, we will now use the definition of  $k^2$  given by 133.

Assuming near plane-wave like propagation in the paraxial approximation one writes,

$$E = \psi(x, y, z) \exp(-ikz) \quad (134)$$

Using Eq.132, Eq.133, and Eq.134 one gets,

$$\nabla_{\perp}^2 \psi - 2ik_o n_3 \psi' - 2k_o^2 n_3 n_4 r^2 \psi = 0 \quad (135)$$

where  $\psi' = \frac{\partial \psi}{\partial z}$  and  $\psi''$  is assumed negligible compared to the other terms. Eq.135 is a parabolic equation with an exact solution. Writing  $\psi$  in terms of a complex phase parameter  $\tilde{P}$  and a complex beam parameter  $\tilde{Q}$  such that,

$$\psi = \exp \left[ -i \left( \tilde{P} + \frac{1}{2} \tilde{Q} r^2 \right) \right] \quad (136)$$

one arrives at the following relationships,

$$\tilde{P}' = -i \frac{\tilde{Q}}{k_o n_3} \quad (137)$$

and,

$$\tilde{Q}^2 + k_o n_3 \tilde{Q}' + 2k_o^2 n_3 n_4 = 0 \quad (138)$$

where the term  $\frac{\partial(k_o n_3)}{\partial z}$  has been omitted. The problem of the wave equation has now been converted into the problem of the solutions to Eq.137, and Eq.138.

The solution to Eq.138 yields the gaussian q-parameter defined by  $q \equiv \frac{k_o n_3}{\tilde{Q}}$ ,

$$q(z) = \frac{\cos(\varphi z)q(0) + (1/\varphi) \sin(\varphi z)}{-\varphi \sin(\varphi z)q(0) + \cos(\varphi z)} \quad (139)$$

where  $\varphi = \sqrt{2n_4/n_3}$ . Here,  $q(0)$  represents the q-parameter at the first interface. Using the well known technique of ray matrices one can identify from Eq.139 the following ABCD ray matrix representation,

$$ABCD \Rightarrow \begin{pmatrix} \cos(\varphi z) & (1/\varphi) \sin(\varphi z) \\ -\varphi \sin(\varphi z) & \cos(\varphi z) \end{pmatrix} \quad (140)$$

### Experiment

Figure 26 shows the experimental setup. In the case of the 10msec square pulse experiments an argon ion laser operating at 514.5nm was used together with an acousto-optic modulator (AOM). The detection was accomplished with the use of fast photodiodes and a digital storage oscilloscope. For the 10nsec experiments, an Nd<sup>+</sup>:YAG pulsed laser operating at 532nm was used with detection accomplished via an energy meter. (Here in place of the AOM above we have an attenuator.) In both cases, a focusing lens of 5cm was used to focus the beam down to  $\sim 40\mu\text{m}$ . Z1 represents the distance from the focal plane of the focusing lens to the front face of the sample. An iris was set 10cm away from the focusing lens with its diameter being equal to the diameter of the beam prior to this lens (giving rise to a transmittance of  $\sim 88\%$  at very low light levels). The second lens is used to collect all the light past the iris.

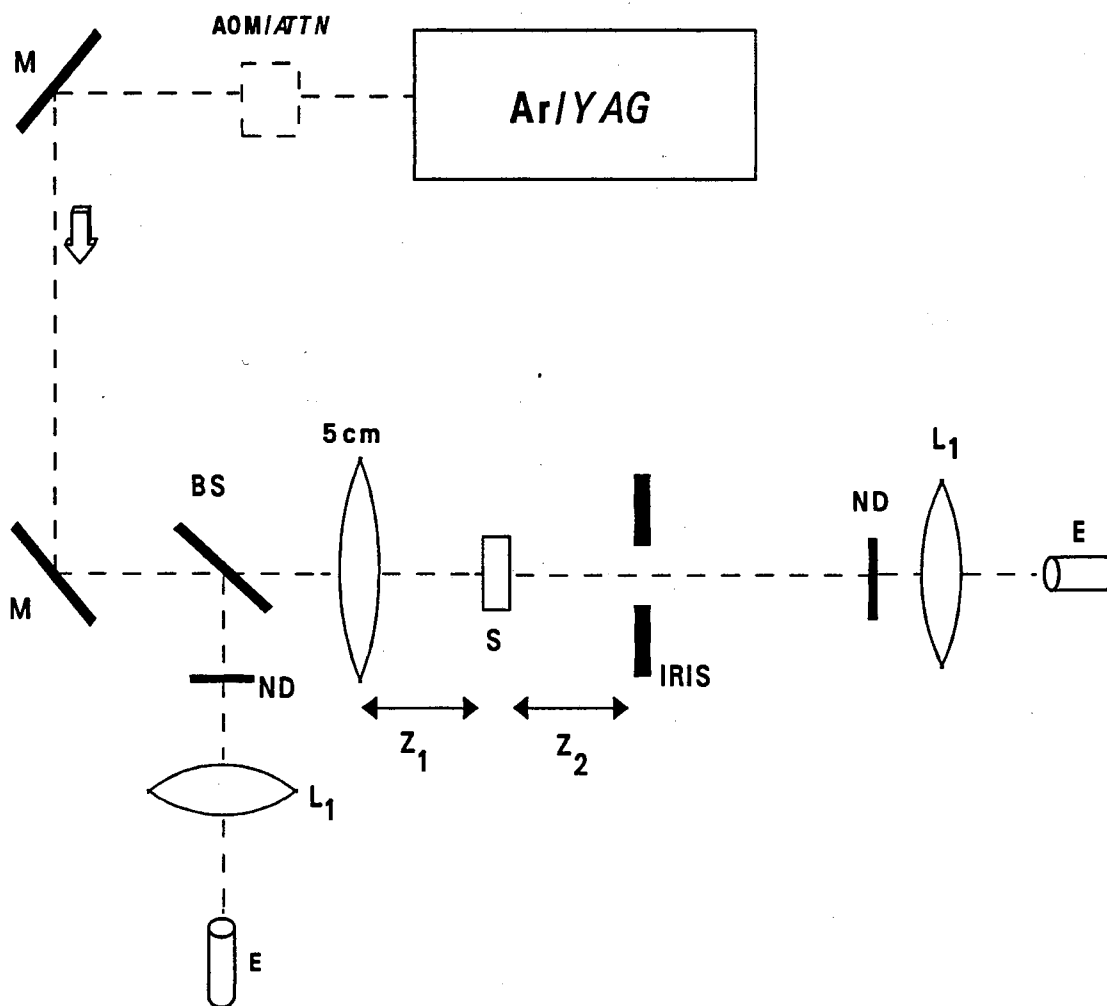


Figure 26. Experimental arrangement for both nanosecond and microsecond experiments in the lead glasses. M-mirror, P/E-photodiode/energy meter, AOM/ATTN-acousto-optic modulator/ attenuator, ND-neutral density filter, BS-beam splitter, S-sample



## Results and Discussion

The ray matrix method was used to model the experimental results whereby a gaussian TEM<sub>00</sub> mode was assumed. Because the ray matrix representation for the sample depends on the waist size of the beam of which continuously changes, an iterative method of carrying out the necessary calculations was used whereby the sample is hypothetically sliced  $m$  times and the beam is assumed to have an unchanging waist size as it traverses each thin slice. Using eq.138 the waist is then recalculated after each slice.

Figure 27 illustrates the 10msec temporal response for the 1.5mm thick sample. Similar results were obtained for the 1mm thick sample. In these four graphs the power of the laser is held constant (275mW) and temporal profiles are collected at four different values of  $Z_1$ . Here the output is not time integrated but rather monitored as a function of time. These plots illustrate the effect of sample location on the time-dependence of the output pulse.

Figure 28 (top) shows the  $Z$ -scans for sample thicknesses of 1mm and 1.5mm. In the bottom of Figure 27 are the respective plots of normalized output vs. input power for two different values of  $Z_1$ . Here the output is the time-integrated output of the pulse. The open and closed circles represent experimental data and the solid line the theory. The open circle data refers to a  $Z_1$  value just before the first minima on the respective  $Z$ -scan and the closed circle data, centered at the minima. These plots show features which have not been previously observed in the literature using similar experiments. These are the characteristic second dip in the  $Z$ -scans (top graphs) and the oscillatory behavior in the transmission (bottom graphs). In the case of the  $Z$ -scans the drop in the transmittance is due to defocusing at the iris. Generally one sees a single minima. However due to the very strong thermo-optic effect in these samples, the beam waist is undulating within the sample. This gives rise to a second minima.

Referring to the  $Z$ -scan at the top of Figure 28, the graphs in Figure 27.(a-d) correspond to  $Z_1$  values just before the first minima (3a and 3b), right at the

minima (3c), and just passed the minima (3d). The response is representative of the change in transmittance at the iris due to the defocusing of the beam. From our theoretical fit our model seems to correctly identify the time dependence.

Figure 29.(a) shows the theoretical Z-scans at three different powers. Adjacent to each Z-scan, Figure 29.(b), is a theoretical plot of the waist size of the beam within the sample after 10msec (i.e.  $Z=0$  refers to the front face and  $Z=.001\text{m}$  the back face) whereby the sample is fixed at  $Z_1$  corresponding to the first minima. As can be seen the undulating of the waist increases with increasing power. For a single minima in the Z-scan there are no undulations in the beam with the exception of that which is due simply to the focusing of the beam prior to the sample. As the power increases, so does the undulating of the beam. It is this undulation within the sample which gives rise to the multiple minima in the Z-scans[81] as well as the oscillatory behavior in Figure 28. The presence of these undulations is very  $Z_1$  dependent as it is determined by the input intensity and the radius of curvature of the phase front. This propagating characteristic occurs for the same reason as the undulating of a laser beam in a fiber optic waveguide with a parabolic transverse index of refraction profile. This can be clarified by the following analysis.

The q-parameter, Eq.139, by definition, can be expressed as,

$$\frac{1}{q(z)} = \frac{1}{R(z)} - i \frac{\lambda}{\pi w^2(z)} \quad (141)$$

where  $R(z)$  is the radius of curvature of the phase front and  $w(z)$  is the beam waist. Expanding Eq.139 into its real and imaginary parts and using Eq.141 we arrive at the following expressions for the beam waist and radius[80],

$$w^2(z) = w^2(0) \left[ \left( \cos(\varphi z) + \frac{1}{R(0)} \frac{\sin(\varphi z)}{\varphi} \right)^2 + \left( \frac{\lambda}{\pi w^2(0)} \frac{\sin(\varphi z)}{\varphi} \right)^2 \right], \quad (142)$$

$$\frac{1}{R(z)} = \frac{\cos^2(\varphi z) - \sin^2(\varphi z)}{R(0)} + \sin(\varphi z) \cos(\varphi z) \left[ \frac{1}{\varphi R^2(0)} - \varphi + \frac{1}{\varphi} \left( \frac{\lambda}{\pi w^2(0)} \right)^2 \right] \quad (143)$$

where  $\varphi = \varphi[w(0)]$ .

Both the beam waist and radius continuously change and are dependent on each other. Clearly these quantities are oscillatory, albeit nonperiodic. For the

index of refraction governed by Eq.128,  $\varphi$  is given by,

$$\varphi[w(z)] = \sqrt{\frac{4P_o\alpha}{n_o w^2(z)k_{th}} \frac{dn}{dT} \frac{t}{t_c} \frac{1}{1 + \frac{t}{t_c}}} \quad (144)$$

where  $n_3 \approx n_o$ .

Because of the interdependence of  $\varphi$ ,  $w$ , and  $R$ , as well as their dependence on time, an iterative method is required to calculate these quantities. Such a calculation for  $w$  is shown in Figure 29. From this figure and eq.144, we see that the number of undulations increases with power, accompanied by a dramatic decrease in the beam waist. One conclusion from this is that filament formation is oscillatory, that is, the filament diameter fluctuates. This is consistent with references cited in section 1. Given the values for thermal diffusivity, thermal conductivity,  $dn/dT$ , the coefficient of absorption, and the operating time scale,  $\varphi$  for this material is sufficient enough to allow for the undulations within the thickness of our samples.  $\varphi$  determines the "frequency" of these undulations and from Eq.144 one can immediately recognize the effect of the various material parameters. Increases in the beam power, coefficient of linear absorption, and nonlinear change in the refractive index,  $dn/dT$ , all have the effect of increasing  $\varphi$ , where as an increase in the waist size or thermal conductivity decreases  $\varphi$ . The ratio of these quantities is directly proportional to the nonlinear change in the refractive index, Eq.128. Thus the greater the nonlinearity, the greater the number of undulations over a given path length. An increase in the thermal diffusivity,  $\eta$  ( $t_c = w^2/8\eta$ ), decreases  $t_c$ , and  $\varphi$  reaches steady state in a shorter time. Or conversely, the less the heat diffusion, the more the nonlinearity will continue to grow, and thus the greater the time for steady state. Finally we note that for shorter times  $\varphi$  decreases. On a nanosecond time scale,  $\varphi$  becomes very small, and the distance between the multiple foci is greater than the thickness of our samples, and thus no undulations are detected.

By making an approximation for the trigonometric quantities, as well as  $R(0)$ , in Eq.142 we are able to compare with the early work by Akhmanov et.

al.[56]. Assume the beam is incident such that  $R(0)$  is infinite. Eq.142 becomes,

$$\frac{w^2(z)}{w^2(0)} = \cos^2(\varphi z) \left[ 1 - \left( \frac{\lambda}{\varphi \pi w^2(0)} \right)^2 \right] + \left( \frac{\lambda}{\varphi \pi w^2(0)} \right)^2. \quad (145)$$

Using Eq.144 we get,

$$\frac{w^2(z)}{w^2(0)} = \cos^2(\varphi z) \left( 1 - \frac{P_{cr}}{P_o} \right) + \frac{P_{cr}}{P_o} \quad (146)$$

where,

$$P_{cr} = \frac{n_o k_{th} \lambda^2}{4\pi^2 w^2(0) \alpha \frac{dn}{dT}} \left( \frac{1 + \frac{t}{t_e}}{\frac{t}{t_c}} \right). \quad (147)$$

Letting  $t$  become very large we have for  $P_{cr}$  at steady-state (ss),

$$P_{cr}^{(ss)} = \frac{n_o k_{th} \lambda^2}{4\pi^2 w^2(0) \alpha \frac{dn}{dT}}. \quad (148)$$

We can always choose some  $z$  such that  $\varphi z$  is small. Thus we expand  $\cos(\varphi z) \approx 1 - \varphi^2 z^2$ . Eq.146 at steady state now reads,

$$\frac{w^2(z)}{w^2(0)} = 1 - \varphi^2 z^2 \left( 1 - \frac{P_{cr}^{(ss)}}{P_o} \right).$$

For  $P_o \ll P_{cr}^{(ss)}$ ,  $w(z)$  will always be greater than  $w(0)$  and as such is divergent. Beam trapping occurs when  $w(z)$  is no longer a function of  $z$ . This condition translates into  $P_o = P_{cr}^{(ss)}$ . For  $P_o \gg P_{cr}^{(ss)}$ ,  $w(z)$  will always be less than  $w(0)$  and thus in the limit of an infinite number of iterations, approach zero. In the classical work by Akhmanov et. al., they have defined the nonlinearity in terms of the permittivity as opposed to the refractive index. Also in arriving at their solution for the beam waist a different phase factor for  $\psi$ , Eq.135, was chosen. However, despite these differences, our results and theirs are consistent with regard to the limiting behavior of the beam waist for gaussian beams in quadratic index media. The optical behavior is determined by the nonlinearity of the refractive index. We note that for an increase in the nonlinearity (increase in the absorption or  $dn/dT$  and decrease in the thermal conductivity), the critical power,  $P_{cr}^{(ss)}$ , decreases. In other words, less power is necessary to achieve the same optical behavior by proper adjustment of the other material parameters. By decreasing the thermal conductivity the heat is further localized and thus the nonlinearity increases. Similarly,

by increasing the absorption, more heat is supplied to the medium, and this also enhances the nonlinearity.  $dn/dT$  has the property of increasing the refractive index for an increase in temperature. The greater  $dn/dT$ , the sharper the change in the refractive index, and thus the greater the self-focusing.

The results of the nanosecond experiments are given in Figure 30 and arranged as in Figure 28. In Figure 30 we do not see a second minima in the Z-scan nor any oscillatory behavior in graphs Figure 30. On this time scale the change in temperature, and hence change in the index of refraction, is insufficient to bring about any undulations of the beam. However as is apparent in both graphs the thermal lensing is still quite significant and our model, utilizing the same parameters, fits the results fairly well. In Figure 30 the effect of increased thickness results in a lowering of the output fluence. This would be expected merely from the increase in absorption. However, by dividing out the effect of absorption we have seen it is due primarily to an increase in the lensing. This can be understood by considering the medium as a continuous distributed lens system. The greater the number of lenses, the greater the defocusing, unless the beam begins to undulate, which it does not on this time scale. Thus by utilizing a thicker sample one sacrifices visibility for greater limiting of the transmittance. Similar to Figure 28, Figure 30 shows how these glasses may prove useful as a light controlling device. We note that in Fig.30.(b) the glass is being damaged beyond  $\sim 2\text{J}/\text{cm}^2$ . Thus upon each pulse the sample is translated in the xy-plane. Even though the sample experiences damage, the limiting property of this material is still active.

In fitting the data the following constants were used:  $n_o=1.82$ ,  $k_{th}=.5\text{Wm}^{-1}\text{K}^{-1}$ ,  $\alpha=800\text{m}^{-1}$ ,  $\eta=1\times 10^{-6}\text{m}^2\text{sec}^{-1}$ , and  $dn/dT=1\times 10^{-5}\text{K}^{-1}$ . On both time scales we see that the model fits the experimental results quite well. This would seem to indicate that the same physical phenomenon is responsible for the results, namely a change in the refractive index due to thermal heating.

## Conclusion

Basing our model on thermal changes in the refractive index and fitting the experimental results we have found a value of  $dn/dT \sim 10^{-5} K^{-1}$  for the lead silicate glass in our study. Although other nonlinear mechanisms may be occurring on either time scales[57–60] the fits resulting from our analysis indicate that the thermal lensing mechanism is prominent enough to describe the results at least to first order. One application of thermal lensing is in the controlling of light; Figure 28 and Figure 30. From our modeling we see that a number of physical parameters strongly influence the relative strength of the thermal lensing effect. For strong thermal lensing  $dn/dT$  should be relatively large. This is because  $n$  is directly proportional to  $dn/dT$ . A small value for the thermal diffusivity and thermal conductivity is also necessary. If the heat generated readily diffuses then the change in temperature at a fixed point will be relatively small as will its gradient. Once a temperature gradient is established, small heat conduction is necessary for maintaining the gradient: For strong lensing one would like the index of refraction profile to follow that of the exciting beam. This can only happen if the heat is localized (small  $\eta$ ) and the heat conduction minimal (small  $k_{th}$ ). The order of magnitude for these three parameters together with the ease by which silicate glasses may be fabricated make these materials attractive as light controlling devices.

There is a trade-off between the coefficient of absorption and sample thickness and that of visibility (transmittance prior to any thermal lensing). Increasing the absorption increases the heating and thus increases the thermal lensing. Increased sample thickness increases the extent of the active medium. However both these variables decrease the level of throughput, lowering the visibility through the sample. The results of the millisecond experiments have allowed for the undulations of the laser beam to be investigated in a new way. Here we see that the front portion of the input pulse readily establishes a quadratic index profile such that the portion of the pulse to follow not only enhances this profile but is guided

through the sample much in the same way as a gaussian beam in a quadratic or gaussian index fiber optic waveguide.

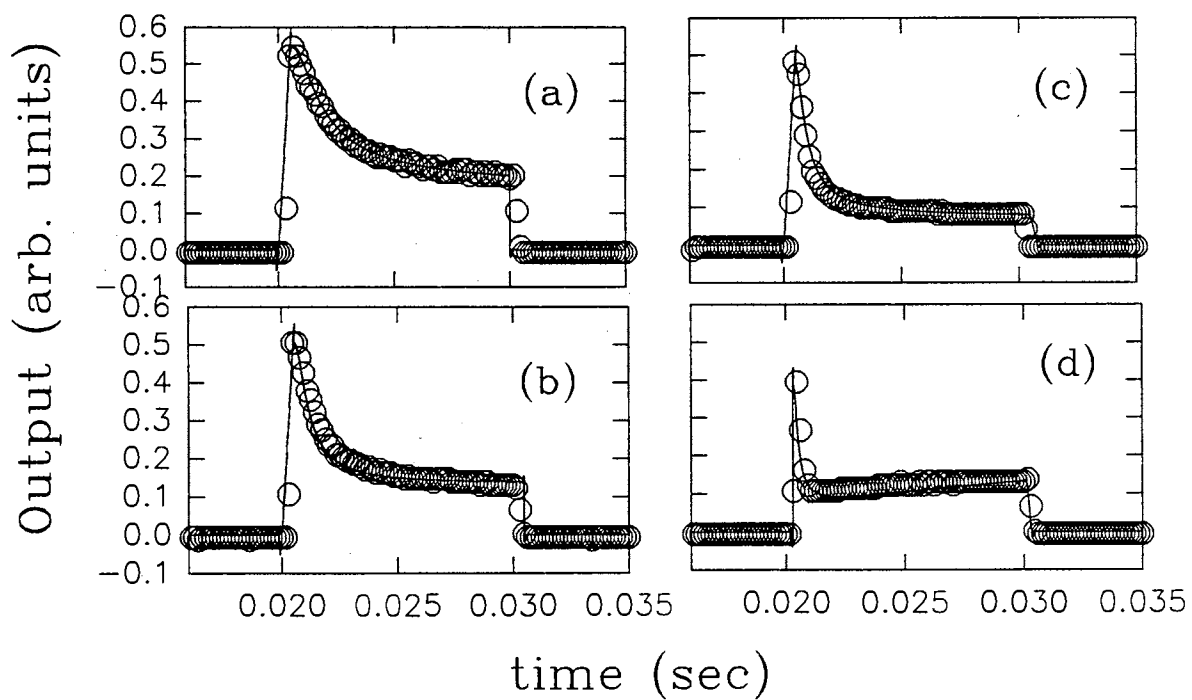


Figure 27. Millisecond temporal response at four values of  $Z_1$  with a laser power of 275mW. (a)  $Z_1=4.77\text{cm}$ , (b)  $Z_1=4.79\text{cm}$ , (c)  $Z_1=4.84\text{cm}$ , and (d)  $Z_1=4.88\text{cm}$ . The solid curves through the circled data points are theoretical fits described in the text.



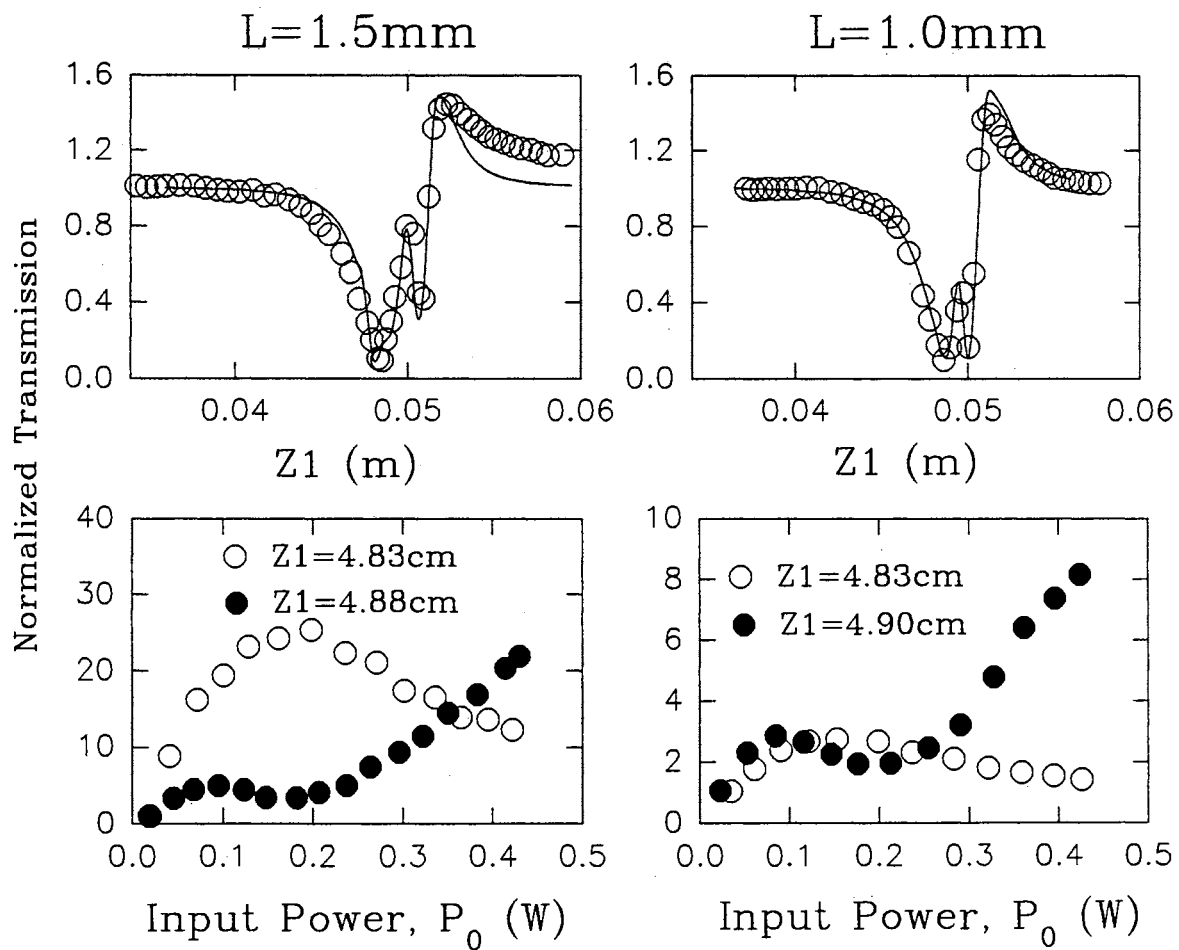


Figure 28. (a) Z-scans and (b) normalized transmittance versus input power at two different values of  $Z_1$ . The solid curves through the circled data points are theoretical fits described in the text.

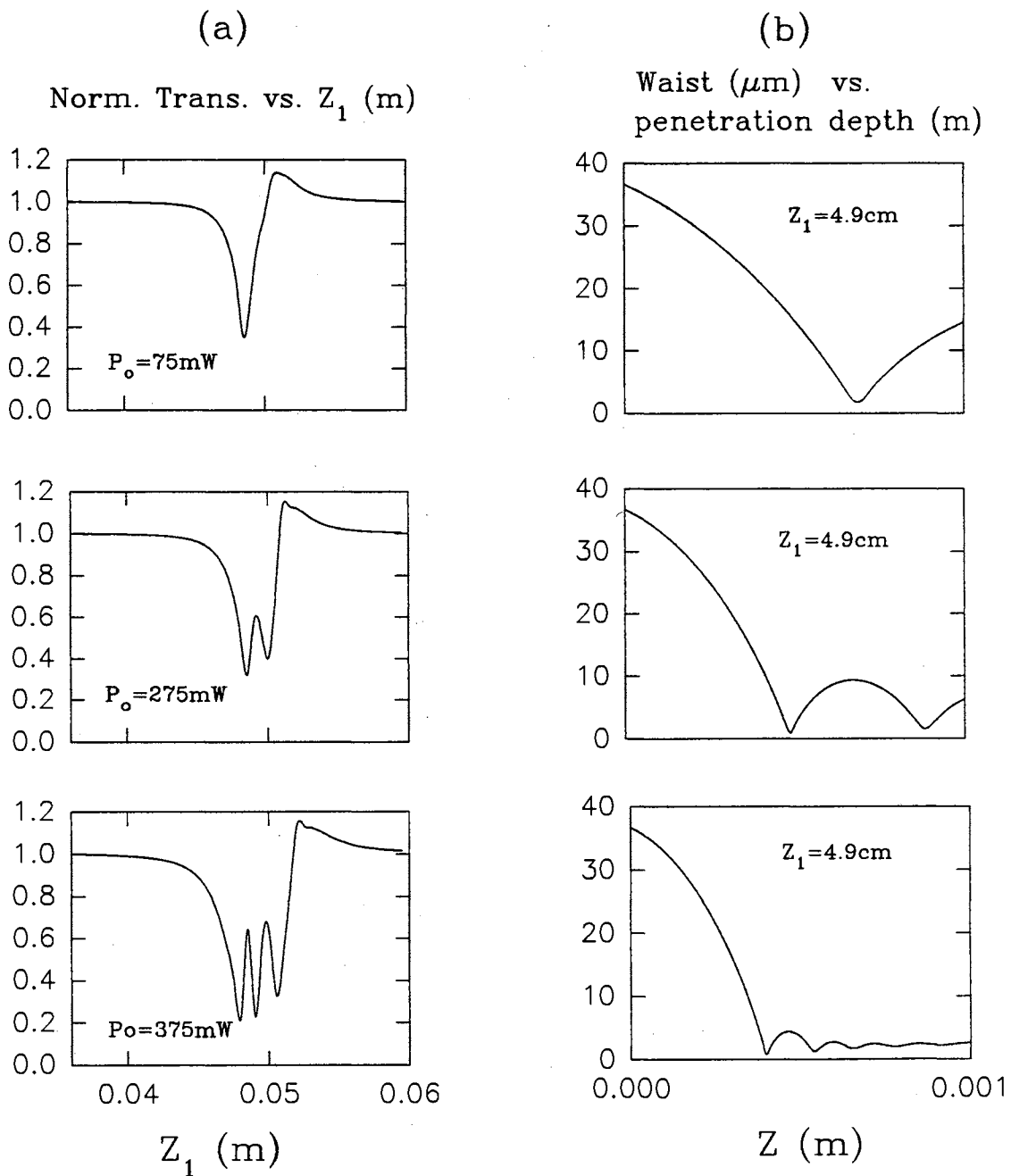


Figure 29. (a) Theoretical  $Z$  scans at three different powers; (b) theoretical change in waist size within the sample for each adjacent  $Z$  scan for a fixed sample position  $Z_1 = 4.9\text{cm}$ .

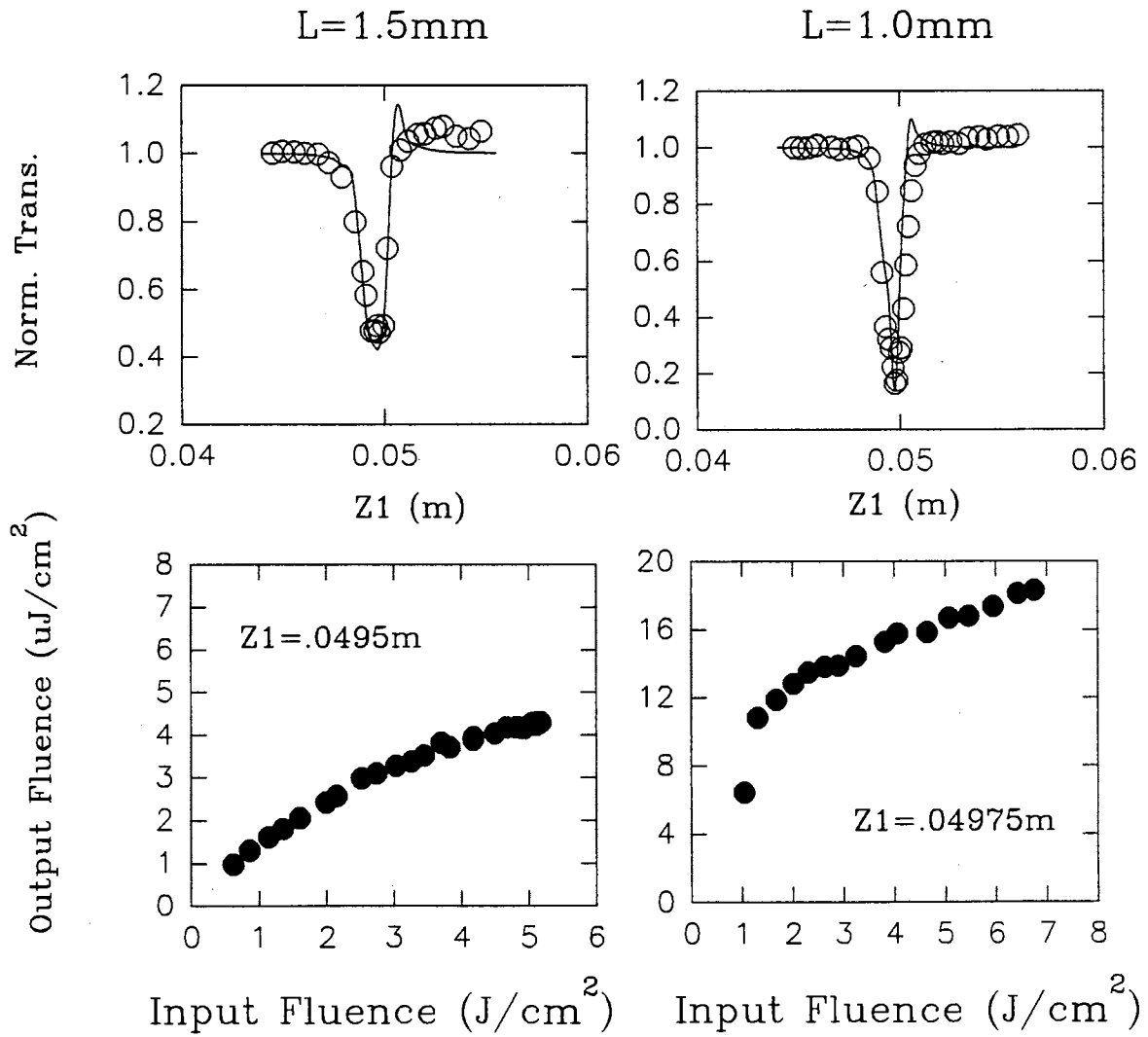


Figure 30. Results of nanosecond experiments: (a) Z scans, (b) output fluence versus input fluence ( $Z1$  fixed). Solid curves are theoretical fits.

## CHAPTER IV

### NONLINEAR TRANSMISSION IN CdS

#### Introduction

Much work has been done in CdS over the past few decades. More recently however has been the investigation of the thermal and electronic nonlinearities associated with the bistable behavior of both bulk and thin film CdS[3,82,83,1,84,85]. Our investigation is on a much slower time scale and involves a two beam geometry. Specifically, modulation of a HeNe probe beam has been observed in CdS by exciting the material with a CW argon ion source operating at a strongly absorbed wavelength. The surface effect resulting indicates the formation of a lens due to 1) the distortion of the front face and 2) a transverse gradient in the index of refraction. In addition to the induced positive lens a Fabry-Perot interferometer is recognized, due to thermal expansion, yielding a temporal variation in the transmittivity of the probe beam.

#### Experiment

The experimental setup for these measurements is shown in Figure 31. The exciting source is an argon ion laser operating at 514.5nm. At this wavelength the absorptance is  $\sim 4.5$ . The argon beam is completely absorbed and thus a 1mW HeNe laser is used to probe the response of the sample. This weak probe beam at a wavelength of 632.8nm lies well below the absorption edge and does not perturb the optical properties of the sample. Both beams operate continuously. A thin glass plate is used as a beam splitter to collinearize the two beams. A 5cm focal length lens focuses both beams perpendicular to the z-axis of the sample. The

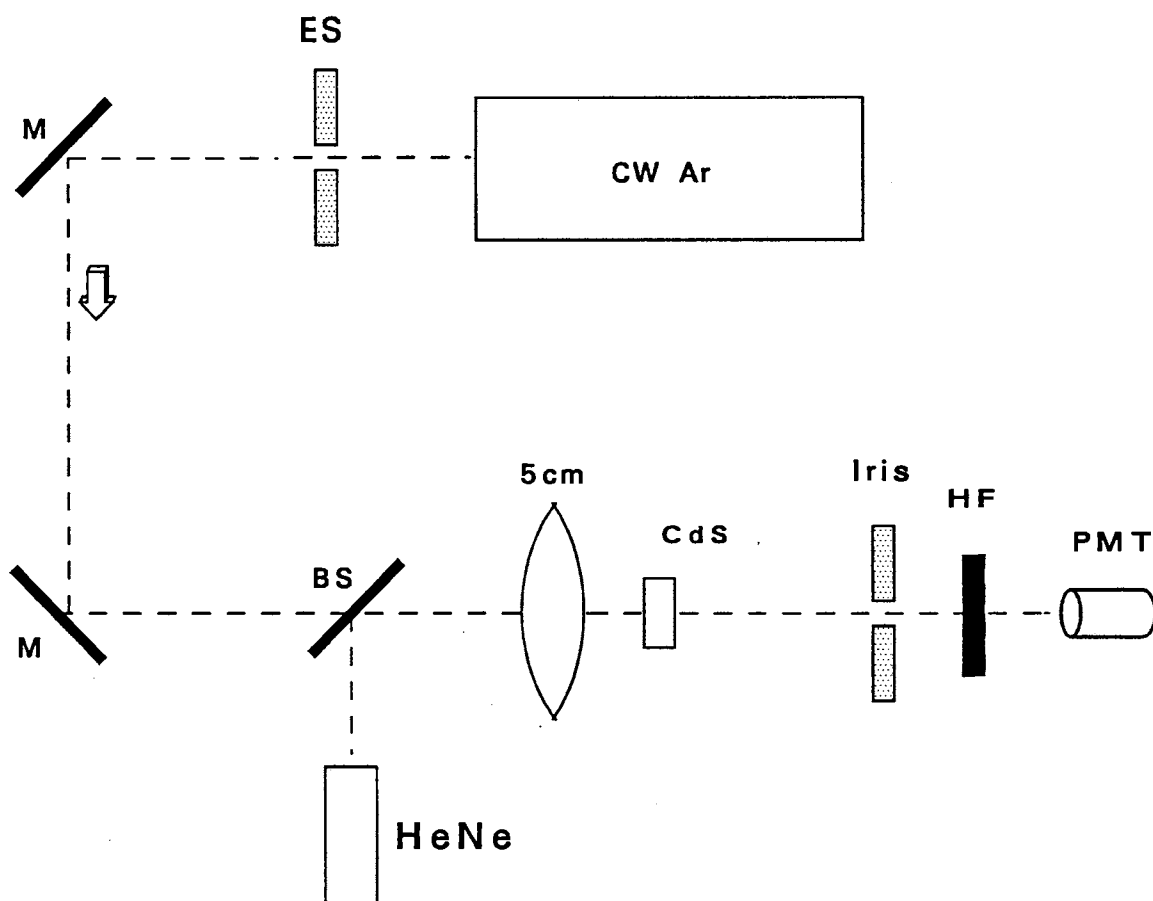


Figure 31. Experimental configuration for two beam transmission study in CdS. ES-electronic shutter, M-mirror, BS-beam splitter, HF-HeNe filter, PMT-photomultiplier tube.

time scale is on the order of 90 seconds. The transmission of the HeNe beam was recorded as a function of time for a fixed power of the Argon beam. Experimental results indicate that the strong absorption of the Argon beam at the surface of the material causes sufficient heating that thermal expansion results in a bulging of the front face. This end distortion establishes a positive lens as well as a time varying interferometer. Because the index of refraction varies with temperature a transverse gradient in the refractive index also acts to produce a positive lens. To account for the observed modulation of the probe beam, a model based on these mechanisms is offered.

### Theory

Because all the light beyond the iris is collected it is only necessary to calculate the transmittance beyond this point. The sample is partitioned into two sections. The front section is that section over which the exciting beam is completely absorbed. In this section thermal expansion takes place as well as a radial change in the index of refraction. This section is modeled as a thin lens and time varying interferometer. The rest of the sample is modeled as having a uniform index of refraction and fixed thickness. The input plane of the optical system is taken to be the principal plane of the focusing lens and the output plane of the system is the plane containing the iris. The approach is to 1) approximate the front section as a thin lens 2) use ray matrices to find the waist size of the probe beam at the iris 3) calculate the transmittance through the iris 4) and finally multiply this transmittance by the transmittivity of the sample governed by the expansion.

Heating of the sample results from the absorption of the argon ion laser beam. The change in temperature is governed by the heat flow equation,

$$\frac{1}{\eta} \frac{\partial T(\vec{r}, t)}{\partial t} = \nabla^2 T(\vec{r}, t) + 4\pi Q(\vec{r}, t) \quad (149)$$

where  $\eta$  is the thermal diffusivity and  $Q$  the forcing function. As in Chapter III the Green's function is [78],

$$G(\vec{r}, t; \vec{r}', t') = \frac{1}{4\pi(t-t')} \exp \left[ -\frac{|\vec{r} - \vec{r}'|^2}{4\eta(t-t')} \right] \quad (150)$$

and the change in temperature is then given by,

$$\Delta T(\vec{r}, t) = \int_0^t \int_0^\infty \int_0^{2\pi} \frac{\exp\left[-\frac{|\vec{r}-\vec{r}'|^2}{4\eta(t-t')}\right]}{(t-t')} Q(r') r' dr' d\phi' dt' \quad (151)$$

The forcing function is due to the absorption of light energy and is written as,

$$Q(r') = \frac{I(r')\alpha}{k_{th}} = \frac{2P\alpha}{\pi w_A^2 k_{th}} \exp\left(-2\frac{r'^2}{w_A^2}\right) \quad (152)$$

where  $k_{th}$  is the thermal conductivity,  $\alpha$  the coefficient of linear absorption for the argon laser,  $w_A$  the waist size of the argon beam inside the sample, and P its peak output power. The final result for the change in temperature is,

$$\Delta T(r, t) = \frac{P\alpha}{k_{th}} \left[ \ln\left(1 + \frac{t}{t_c}\right) - 2\frac{r^2}{w_A^2} \left(\frac{\frac{t}{t_c}}{1 + \frac{t}{t_c}}\right) \right] \quad (153)$$

where  $t_c = \frac{w_A^2}{8\eta}$ . Here we used a constant value for the absorption coefficient for both the Ar<sup>+</sup>-ion (514.5nm) beam and HeNe (632.8nm) beam. At the 632.8nm line the absorption is negligible and is neither effected by the increased temperature nor induced electron-hole density. The 514.5nm line is just below the band gap and as such the absorption is elevated slightly as the temperature is raised. We have used a constant optical density of five. Referring to the absorption spectra in Figure 34 we see that the absorption at  $\lambda = 514.5\text{nm}$  is tuned above the gap for  $\Delta T > 25\text{K}$ . Such a temperature change occurs very shortly after the beam is turned on thus justifying the use of a constant. (This will be addressed once more later.)

The change in length (bulging) at the front face due to thermal expansion is,

$$\Delta L = L_1 \alpha_{th} \Delta T \quad (154)$$

where  $\alpha_{th}$  is the linear coefficient of thermal expansion and  $L_1$  the region at the front end of the sample over which expansion takes place (taken to be the depth through which the intensity drops to  $e^{-5}$  of its peak value). The lens resulting from the bulging of the front face has a focal length given by[66],

$$f_1 = \frac{R}{2(n_o - 1)} \quad (155)$$

where  $R$  is the radius of curvature given by,

$$R = - \left( \frac{d^2 \Delta L}{dr^2} \right)^{-1} = \frac{k_{th} w_A^2}{8 P \alpha_{th} L_1} \left( \frac{1 + \frac{t}{t_c}}{\frac{t}{t_c}} \right) \quad (156)$$

and the index of refraction at the surface, excluding the radial variation, is assumed to be unchanged by the thermal expansion.

A second lens is formed due to the radial dependence on the index of refraction. The index of refraction is written as,

$$n = n_o + \frac{dn}{dT} \Delta T \approx n_o \left( 1 - \frac{r^2}{2b^2} \right) \quad (157)$$

where,

$$b^2 = \frac{n_o k_{th} w_A^2}{4 \frac{dn}{dT} P \alpha} \left( \frac{1 + \frac{t}{t_c}}{\frac{t}{t_c}} \right) \quad (158)$$

A thin lens approximation yields a focal length given by,

$$f_2 = \frac{b^2}{L_1} \quad (159)$$

Upon superimposing the two lenses one gets a single thin lens with a combined focal length given by,

$$f_{net} = \left( \frac{1}{f_1} + \frac{1}{f_2} \right)^{-1} = \frac{4 k_{th} w_A^2}{P \alpha L_1} \left( \frac{1 + \frac{t}{t_c}}{\frac{t}{t_c}} \right) \left( \frac{1}{n_o} \frac{dn}{dT} + 4 \alpha_{th} (n_o - 1) \right)^{-1} \quad (160)$$

Using ray matrices the waist size of the probe (HeNe) beam at the iris is calculated whereby the normalized transmittance through the iris is given by,

$$1 - \exp \left( -2 \frac{R_{iris}^2}{w_H^2} \right) \quad (161)$$

where  $R_{iris}$  is the radius of the iris and  $W_H$  is the waist size of the HeNe beam at the iris.

The transmittivity for the time varying Fabry-Perot interferometer is approximated by that of a parallel plate interferometer. Although the bulging of the front face must have some effect only the center portion of the beam is collected. The transmittivity for a parallel plate Fabry-Perot interferometer is,

$$T = \frac{1}{1 + \left( \frac{4R}{1-R} \right)^2 \sin^2 (\delta/2)} \quad (162)$$



where  $R$  is the reflectivity at the front and back interface and,

$$\delta = 2\pi \frac{n_o(L_o + L_1 + \Delta L)}{\lambda_H} \quad (163)$$

and  $\lambda_H$  is the wavelength of the HeNe laser. The following values for CdS were used[86]:  $n_o = 2.48$ ,  $\alpha_{th} = (4.2 \pm .1) \times 10^{-6} \text{mK}^{-1}$ ,  $k_{th} = (17.4 \pm 1) \text{Wm}^{-1}\text{K}^{-1}$ , and  $\eta = (9.05 \pm .78) \times 10^{-6} \text{m}^2 \text{sec}^{-1}$ .

### Results and Discussion

Experimental and theoretical results are shown in Figure 32 and Figure 33 respectively. The essential features to note are 1) the number of oscillations increases with power 2) the mean value decreases with increasing power and 3) the peak to peak amplitude decreases with increasing power. 1) may be understood by noting that the degree of expansion will increase with the amount of heat supplied over a given time scale. Hence the number of wavelengths over which the interferometer expands increases as the power increases, thus the number of oscillations increases. Features 2) and 3) are very dependent on the location of the sample. Here the sample is placed such that the two beams are focused into the sample, beyond the front face. The induced lens intercepts the HeNe beam as it is converging causing the beam to become diverging at the iris. From Eq.155, Eq.158 and Eq.159 both  $f_1$  and  $f_2$  decrease with increasing power. Note from Eq.160 and the material properties that these quantities make roughly equal contributions.  $f_1$  decreases with increasing power because the radius of curvature of the bulging decreases, increasing the angle of incidence and refracting the light even greater.  $f_2$  decreases with increasing power because the parabolic profile for the index of refraction becomes sharper, further refracting the light. As a result the net focal length for the induced positive lens decreases as the power increases causing the beam at the iris to become increasingly defocused. The energy density protruding the iris thus decreases with increasing power resulting in a drop in the mean value as well as a decrease in the peak to peak value. Had the two beams reached their focal point prior to penetrating the sample the light at the iris would have become

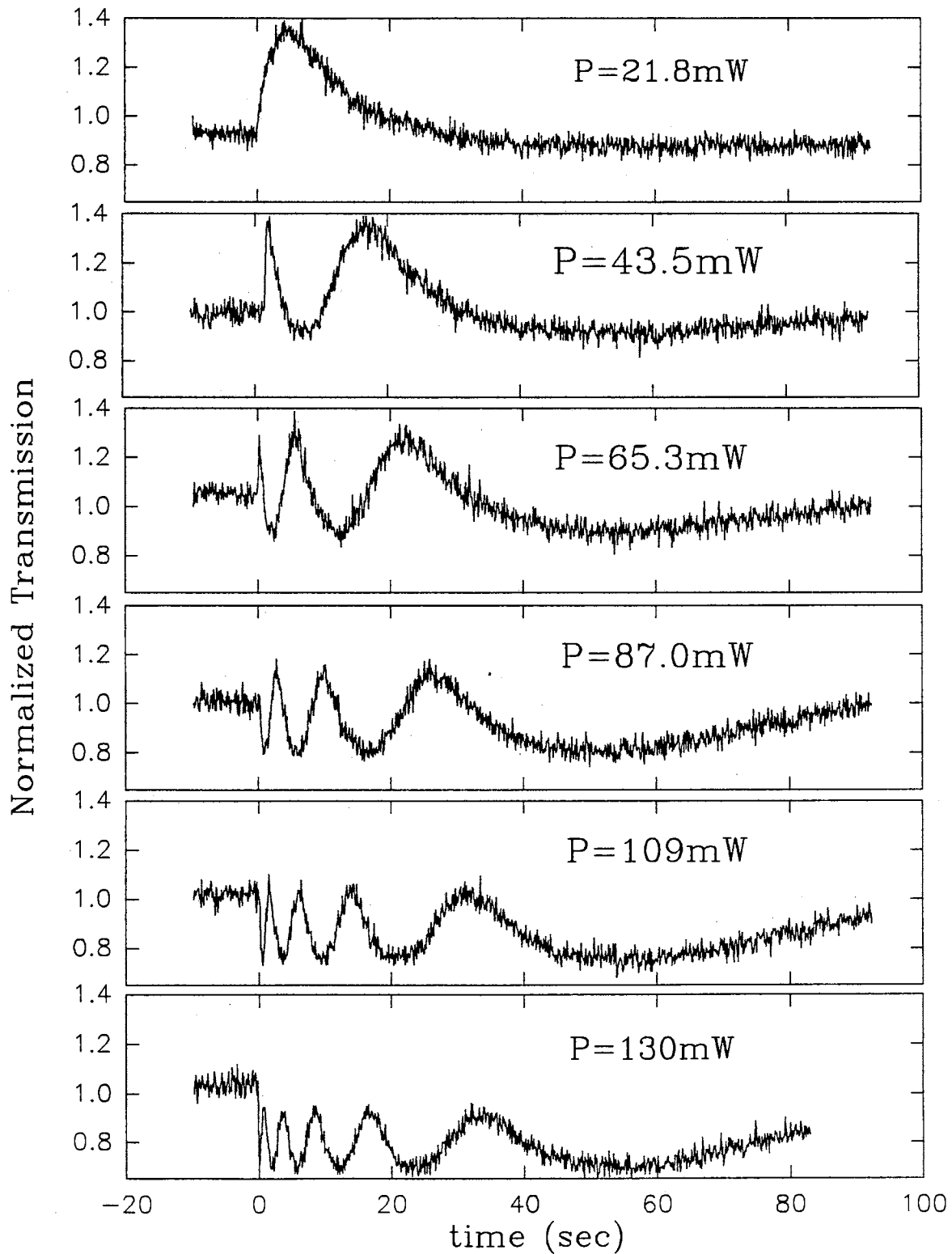


Figure 32. Experimental normalized transmission profiles as a function of time at six different powers.

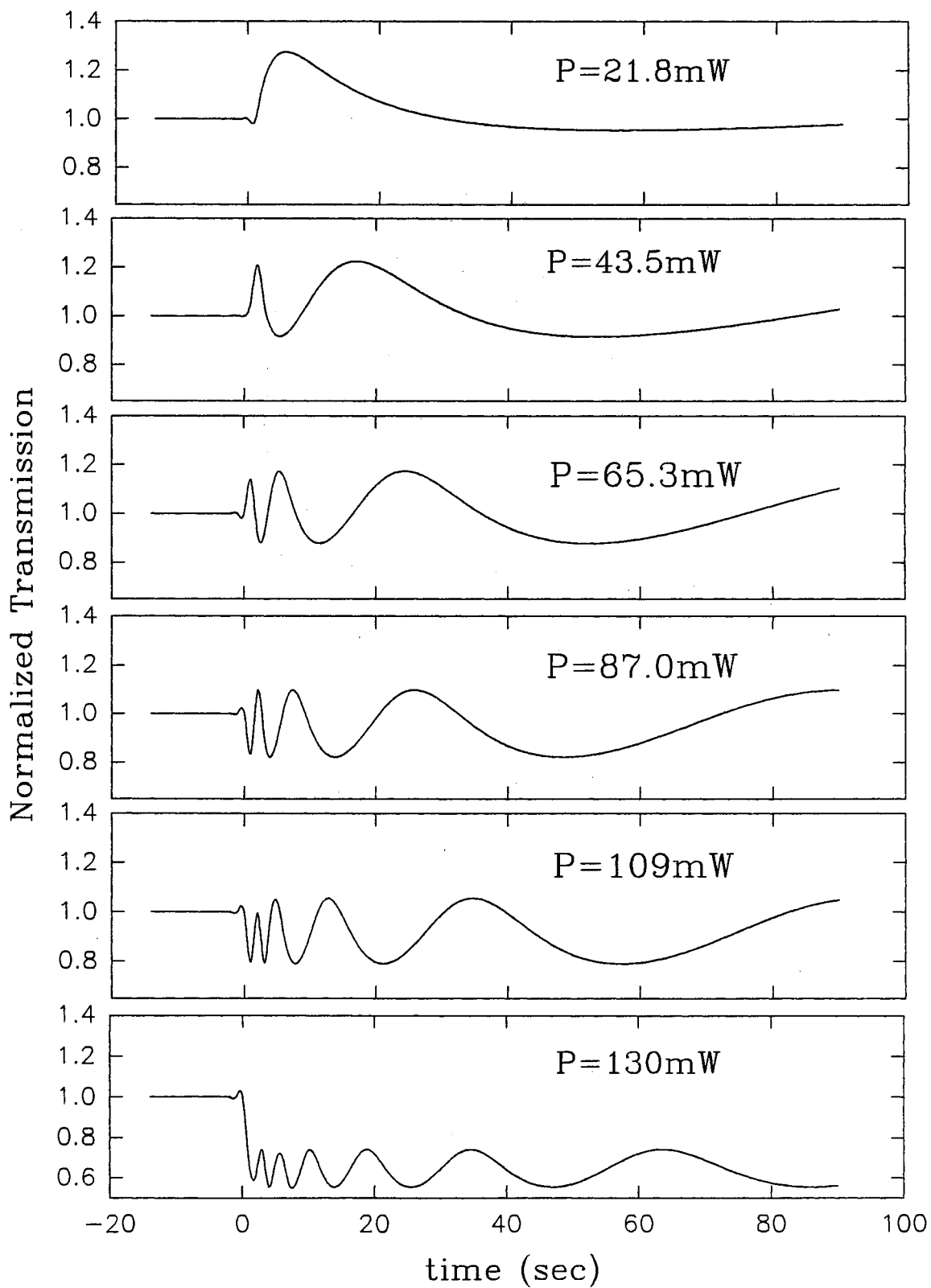


Figure 33. Theoretical normalized transmission profiles as a function of time at six different powers.

increasingly focused, yielding an increase in the amount of light protruding the iris.

A number of approximations have been invoked. Of those some of the most significant may perhaps be 1) that the model allows for unrestrained thermal expansion. Restraining forces prevent the bulging from expanding indefinitely, thus eventually some point of equilibrium is approached. 2) The thermal and optical properties were assumed independent of this expansion. 3) z-directed heat flow was neglected. Certainly the sample bulk beyond the first hypothetical layer is a good heat conductor and will act as a heat sink to some extent. As can be seen by comparing Figure 33 to Figure 32, these mechanisms perhaps gain greater significance at the higher powers. At the higher powers, the time dependence becomes increasingly less accurate.

In Figure 34 we show the absorption spectra for CdS. The theoretical curves (solid lines) are calculated as described in Chapter II, section Theory II.B. while the filled circles are experimental. In Figure 35 we show the refractive index spectra (top) and the refractive index as function of the change in temperature at the wavelength 514.5nm ( $N=10^{21}\text{m}^{-3}$ )(bottom). This illustrates the result of the resonant enhancement of the change in the refractive index due to band gap shrinkage. We have empirically fitted the refractive index change at 514.5nm by a natural logarithm, the result being,

$$\Delta n = 5.308 \ln \left( 1 + \frac{\Delta T}{18.48} \right) \times 10^{-4} \quad (164)$$

Because we are exciting the beam very near the band gap there is not a significant contribution from thermal band gap shrinkage. Consider the following. For temperature changes much beyond 100K the change in the refractive index with temperature approaches a value given by the slope of that portion of the curve, namely,

$$\left( \frac{\partial n}{\partial T} \right)_{on}^{\Delta T > 100K} \approx 2.78 \times 10^{-6} K^{-1} \quad (165)$$

which is  $\sim 5\%$  the background term ( $5.5 \times 10^{-5} K^{-1}$ ). For temperatures changes less than approximately 100K the on-resonant term is given by Eq.164. From Eq.153

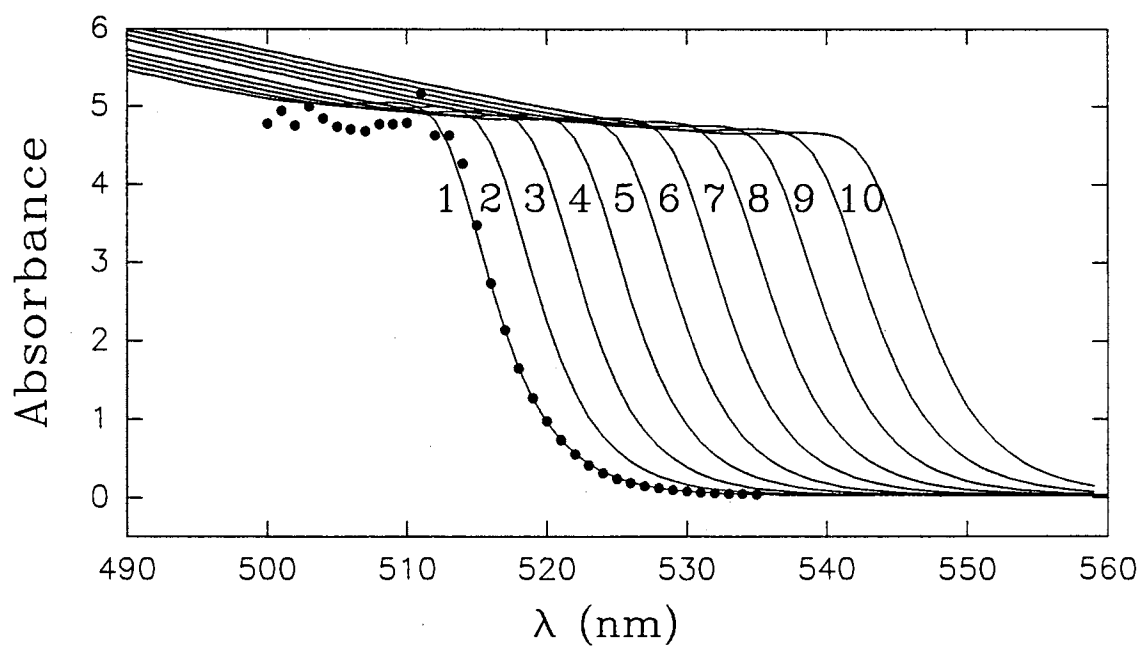


Figure 34. Absorption spectra for CdS. The closed circles are experimental results while the solid are theoretical. Curves 1 thru 10 correspond to temperatures  $290\text{K} + 0, 30, 60, 90, 120, 150, 180, 210, 240, 270$ .

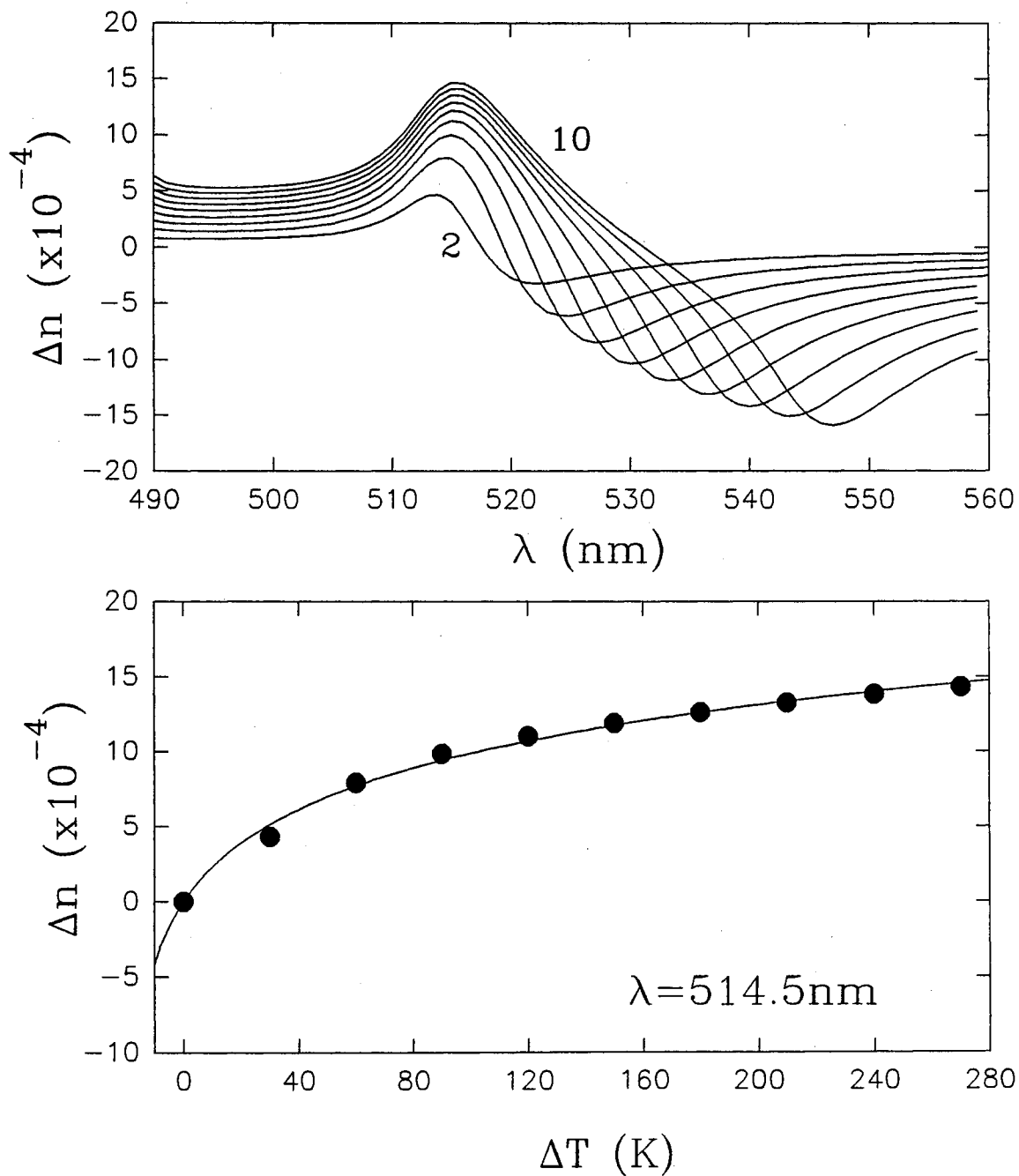


Figure 35. (a) Refractive index spectra at low e-h density for temperatures of 290K + 30, 60, 90, 120, 150, 180, 210, 240, 270 corresponding to curves 2 thru 10 respectively, (b) change in the refractive index as a function of the change in temperature at the wavelength 514.5nm.

we can estimate the time for the sample to reach 100K above room temperature. The change in temperature on-axis is given by,

$$\Delta T = \frac{P\alpha}{k_{th}} \ln \left( 1 + \frac{t}{t_c} \right) \quad (166)$$

and  $t_c = \frac{w\Delta}{8\eta}$ . The longest time occurs at the lowest power, so we will examine the case of  $P$  equal to 21.8mW. Using the previously defined values for the other material parameters and assuming a waist size of  $40\mu m$  the time necessary to elevate the sample 100K is  $\sim 1.4$ sec. Thus the on-resonant term is relatively short lived in comparison to the entire scan. This term would only reveal itself in the initial drop (see Figure 32) about  $t=0$ . No such "spike" is detected. In fact the largest change in the refractive index for changes in temperature less than 100K occurs at  $\Delta T = 0$  (or equivalently  $t=0$ ). Here the slope is given by a first order expansion of Eq.164 giving,

$$\left( \frac{\partial n}{\partial T} \right)_{on}^{\Delta T=0K} = 2.87 \times 10^{-5} K^{-1}$$

which is approximately 50% the background contribution, of which is certainly not insignificant. However the temporal resolution of our experiment at  $t=0$  is limited by the speed of the electronic shutter, which is roughly 10msec. In this time the change in temperature is approximately 55K. At this point the on-resonant term is,

$$\left( \frac{\partial n}{\partial T} \right)_{on}^{\Delta T=55K} = 0.722 \times 10^{-5} K^{-1}$$

which is approximately 13% the background term. Thus any significant on-resonant contribution is so short lived relative to the experiment that we are justified in assuming a constant  $dn/dT$ , that is,

$$\frac{dn}{dT} \approx \left( \frac{\partial n}{\partial T} \right)_{off}$$

### Conclusion

The model served to verify the proposed mechanisms responsible for the observed modulation of the probe beam. The model allows for the dependence of

the sample location to be simulated. Experimentally it is very difficult to measure the exact location of the sample relative to where both the argon and HeNe beams come to focus. The model predicts that the two beams must have been focused into the sample by approximately 1mm. With the formulation worked out in Chapter II we were able to identify both an on-resonant enhancement of the refractive index as well as off-resonant (background) contribution. We were able to qualitatively justify the negation of the on-resonant term, due to a shifting of the band gap, because at the onset of excitation wavelength is already nearly above the gap. Any significant contribution from the resonant term occurs within a time span comparable to the resolution of the experiment. Lastly it is seen in our formulation that the contributions to the lensing from a change in the refractive index and bulging at the surface are approximately equal.



## CHAPTER V

### SUMMARY AND FUTURE WORK

The optical bistability experiments of chapter II in bulk ZnSe illustrated absorptive switching from microseconds to seconds with incident powers of  $\sim 600\text{mW}$  to  $\sim 300\text{mW}$  respectively. Transverse structures were also measured and revealed, at low powers, the development of ring and hole type structures. The evolution of these structures results from switching, or thermal waves as a result of heat diffusion transverse to the incident beam. We have theoretically simulated such transverse waves on all time scales. The model suggest that the single hole and ring type structures result at low powers, however at the higher powers multiple ring patterns occur. By plotting the intensity throughout the bulk of the sample as the output is switching one may clearly identify a myriad of structures. As the system evolves the multiple rings move outwards transverse to the beam, resembling switching waves. The far field beam pattern would then presumably manifest multiple ring patterns moving outward giving the image of a wave. Our model is based on thermal band gap shrinkage. This is the necessary feedback mechanism of which any bistable system requires. We have included electronic effects as it is the radiationless recombination of induced e-h pairs responsible for the elevation of the lattice temperature. The three governing variables are thus the temperature, e-h density, and electric field strength (intensity). Thus this problem is essentially a heat and particle transport and light diffraction problem. We have employed an explicit finite difference technique to solve the resulting 4-dimensional, coupled, nonlinear partial differential equations. In the case of the diffraction problem we have included a thermal change in the refractive index (phonon assisted, off-resonant) as well as a change in the refractive index due to a temperature tuning

of the band gap (on-resonant). The wavelength employed initially while the system is at room temperature lies at the Urbach tail. As the temperature rises a large resonant enhancement of the refractive index occurs due to a shifting the band edges. Eventually this wavelength is completely temperature tuned across the energy gap and the refractive index change approaches some final value. The effect of the resonant enhancement is theoretically determined to be significant.

Our model suggest that once the system has switched to the off-state the excitation has essentially become localized at the front surface. This occurs as follows. If the beam is focused near the rear of the sample this is where the intensity is greatest. As the temperature rises the absorption increases. As the absorption increases in the region prior to this back region less light reaches that portion of the sample and thus the heating rate decreases. Thus the region of greatest intensity, and thus greatest excitation, eventually moves forward (towards the incident beam). This has been coined as domain motion. Our model suggest this domain is not sharp until localized at the surface. Experimentally all samples eventually damage. By inspection using a microscope it appears all damage points are at the surface. Our model further suggest that once this excitation domain is localized at the surface thermal runaway ensues. The exact nature of the damage is unclear. The damage marks are visible to the naked eye, albeit opaque. The model suggest temperatures are reached in excess of the melting point ( $\sim 1700\text{K}$ ). Perhaps the material melts or maybe at such temperatures some chemical reaction occurs with the ambient (oxidation?). However in some samples, all from the same batch, the material does not immediately damage following switching. Here the material pulses for a period of time and then damages. This pulsing has been named regenerative pulsations and initially was detected in hybrid systems. Later this phenomenon was measured in intrinsic, however a dispersively bistable systems. Rarely has regenerative pulsations been encountered in intrinsic absorptive bistable systems. Our model for such a phenomenon is based on the previously stated mechanism, however we further suggest an increase in the thermal conductivity at the surface. Because the absorptive switching is very similar in all samples the implication is

that the mechanism is the same and as such should apply to the case of regenerative pulsations with an additional mechanism to reverse the switching process (negative feedback). The switching is stimulated by a heating of the sample, that is the heating rate exceeds the cooling rate. (The ambipolar diffusion of the e-h pairs is seen to be negligible.) Thus to reverse the system and stimulate pulsing some mechanism is necessary to allow the cooling rate to exceed the heating rate. Initially it was felt that the diffraction of the beam would give rise to a changing intensity throughout the sample such that the motion of the excitation domain would propagate towards the front portion of the sample until finally the reduced intensity would be insufficient to combat the cooling and the domain would relax and the process would repeat itself. This is essentially the motivation for a 4-dimensional solution to the governing equations. We hoped by properly modeling the diffraction of the beam, with the inclusion of self-focusing, that such a result would exist. Our model however suggest that this never occurs and thus we had to investigate other means of an increased cooling rate (or a decreased heating rate). At the level of excitation in this system the material parameters are presumably nonconstant. The exact dependence on temperature and e-h density is however unclear. The problem is further complicated by the likelihood that this nonlinearity is present at the surface where little is known about these samples. We phenomenologically stipulated a decrease in the heating rate by a factor of twelve at the surface and the result was surprisingly similar to the experiment, at least for the sawtooth type pulsing structures. We have no quantitative argument for this stipulation. Thus the phenomenon of regenerative pulsations remains curious. Our ideas of this phenomenon are not as yet conclusions, but rather potential points of investigation. More work on this problem is certainly required.

We have also made measurements of Z-scans and optical limiting scans on a millisecond and nanosecond time scale in a lead oxide modified lead silicate glass. The popular Z-scan is a relatively simple experiment which allows one to identify self-focusing. The optical limiting scans possess the real application of an optical limiting, or clamping device (the electronic analog being the zener diode). The

motivation for this project began as an investigation to quantify the potential of these materials as optical limiters on a nanosecond time scale. The millisecond trials were carried out to further our understanding of the thermal lensing effect in these materials. On this time scale new forms of Z-scans were identified, namely a characteristic second dip. Generally one only sees a single minima. These materials however possessed a sufficient thermo-optic effect that beam undulations within the bulk gave rise to multiple minima in the Z-scan. The Z-scan in this case allowed such beam undulations to manifest themselves in a new way. Our model for these experiments was based on a thermo-optic effect, namely a thermal change in the refractive index. A parabolic approximation of the change in temperature was made, which was calculated using Green's function for the 2-d heat flow equation, giving a parabolic profile for the refractive index. Such an approximation was motivated so that gaussian optics could then be employed to propagate the beam. This is a common technique. The model worked successfully in predicting the Z-scans on both time scales, as well as fitting the temporal transmission profiles on the millisecond time scale. However the modeled failed when attempting to fit the optical limiting scans using the same parameters used to fit the respective Z-scans. This indicates that some improvement in the modeling is required. Perhaps the parabolic approximation could be improved, or relaxed, and some other form of propagating the beam should be invoked.

Lastly we have made measurements of the transmission properties using a two beam geometry in bulk CdS. This project was initiated to investigate the thermo-optic character of this material on a long time scale (seconds). The experiment essentially involves using a strongly absorbed wavelength to heat the material and subsequently change its refractive index and then measure the transmission of a collinear weakly absorbing probe beam. Here a CW Ar<sup>+</sup>-ion and HeNe laser were employed respectively. The experiment indicated a thermal lensing process to be present as well as a time varying Fabry-Perot effect. The transmitted HeNe beam is measured beyond an iris. The thermal lensing manifested itself by an initial drop in the transmission as a result of defocusing at the iris. Such thermal

lensing was successfully modeled by accounting for the radially dependent bulging at the surface, forming a lens, and the thermo-optic change in the refractive index as a result of a radially dependent temperature change. The thermo-optic effect was considered to have both a background, off-resonant, contribution as well as an on-resonant contribution. The conclusion was that the on-resonant contribution (resonant enhancement) was due to thermal band gap shrinkage however was so short lived that could be neglected. The argon laser line (514.5nm) is so close to the band gap at room temperature that it becomes temperature tuned above the gap within  $\sim 1$ sec in this experiment. Thus a constant background thermo-optic coefficient was sufficient to properly model the experimental results. The Fabry-Perot effect was seen as time varying oscillations in the transmission. The "wavelength" of these oscillations dilated in time, indicated the approach to equilibrium. The oscillations were sufficiently characterized by modeling the change in the optical path length. The sample expands due to the elevation in lattice temperature and the refractive index changes as described before. This change in the optical path length gives rise to time varying interference within the cavity. Any future work on these results should probably involve the investigation of 1) heat flow along the optical axis. This was neglected in our model. 2) The effect of the bulging on the interference structure within the cavity. 3) The effect the induced e-h density has on the thermal and optical properties of the material. Here a high density of e-h pairs is expected and the role of such a plasma is as of yet uninvestigated. 4) Lastly one might investigate the role of the expansion of the thermal and optical properties.

## BIBLIOGRAPHY

1. B. S. Wherrett, A. C. Walker, and F. A. P. Tooley, in *Optical Nonlinearities and Instabilities in Semiconductors*, edited by Hartmut Haug (Academic Press, Inc., 1988), pp.262-268.
2. M. Kretschmar, F. Henneberger, H. Rossmann, and I. Haddad, *Phys. Stat. sol. (b)* **143**, K71 (1987).
3. M. Lambsdorff, C. Dornfeld, and C. Klingshirn, *Z. Phys. B- Condensed Matter* **64**, 409 (1986).
4. S. W. Koch, N. Peyghambarian, and H. M. Gibbs, *J. Appl. Phys.* **63**, R1 (1988).
5. S. W. Koch, H. E. Schmidt, and H. Haug, *J. Lumin.* **30**, 232 (1985).
6. S. W. Koch, in *Optical Nonlinearities and Instabilities in Semiconductors*, edited by Hartmut Haug (Academic Press, Inc., 1988), pp.276-282.
7. H. E. Schmidt, H. Haug, and S. W. Koch, *Appl. Phys. Lett.* **44**, 787 (1984).
8. Gibbs, H. M., in *Optical Bistability: Controlling Light with Light* (Academic Press, Inc., 1985), pp.71-82.
9. M. Lindberg, S. W. Koch, and H. Haug, *Phys. Rev. A* **33**, 407 (1986).
10. Sergei E. Esipov, *Superlattices and Microstructures* **11**, 119-124 (1992).
11. V. A. Stadnik, *Optics Comm.* **68**, 445-448 (1988).
12. V. A. Stadnik, *Sov. Phys. Solid State* **29**, 2059-2063 (1987).
13. S. E. Esipov and V. A. Stadnik, *Phys. Stat. Sol. (b)* **150**, 501-505 (1988).
14. Yu. D. Kalafati and Yu. A. Rzhanov, *Physica D* **49**, 177-181 (1991).
15. S. W. Koch and E. M. Wright, *Phys. Rev. A* **35**, 2542 (1987).
16. W. J. Firth and I. Galbraith, *IEEE J. Quantum Electron.* **QE-21**, 1399 (1985).
17. K. Jarasiunas and H. J. Gerritsen, *Appl. Phys. Lett.* **33**, 190 (1978).

18. Characterization/Specification sheet supplied along with the sample by Eagle-Pitcher Industries, Inc..
19. M. V. Urbach, *Phys. Stat. Sol.* **8**, 9-45 (1971).
20. M.D. Feit and J.A. Fleck, Jr., *J. Opt. Soc. Am. B* **5**, 633-640 (1988).
21. M.D. Feit and J.A. Fleck, Jr., *Appl. Phys. Lett.* **28**, 121-124 (1976).
22. E. A. Sziklas and A. E. Siegman, *Proc. of IEEE Letters*, 410-412, March 1974.
23. E. A. Sziklas and A. E. Siegman, *Appl. Opt.* **14**, 1874-1889 (1975).
24. J. V. Moloney, *Opt. Comm.* **41**, 379-382 (1982).
25. H. A. Haus, *Waves and Fields in Optoelectronics*, Prentice-Hall, Inc., New Jersey, 1984.
26. *Handbook of Mathematical Functions*, edited by Milton Abramowitz and Irene A. Stegun, Dover publications, Inc., New York, 1965.
27. R. L. Burden, J. D. Faires, and A. C. Reynolds, *Numerical Analysis*, 2<sup>nd</sup> Edition, PWS Publishers, Boston, Mass., 1981.
28. L. Lapidus and G. F. Pinder, *Numerical Solution of Partial Differential Equations in Science and Engineering*, John Wiley & Sons, Inc., 1982.
29. L. Bányai and S. W. Koch, *Z. Phys. B - Condensed Matter* **63**, 283-291 (1986).
30. R. J. Elliott, *Phys. Rev.* **108**, 1384 (1957).
31. V. Bargmann, *Mathematics* **38**, 961-966 (1952).
32. E. M. Wright, S. W. Koch, J. E. Ehrlich, C. T. Seaton, and G. I. Stegeman, *Appl. Phys. Lett.* **52**, 2127-2129 (1988).
33. M. Capizzi, S. Modesti, A. Frova, J. L. Staehli, M. Guzzi, and R. A. Logan, *Phys. Rev. B* **29**, 2028 (1984).
34. V. C. Aguilera-Navarro, G. A. Estévez, and Allyn Kostecki, *J. Appl. Phys.* **63**, 2848-2850 (1988).
35. J. V. Moloney, *IEEE J. Quantum Electron.* **QE-21**, 1393-1398 (1985).
36. W. D. St. John and J. P. Wicksted, *J. Appl. Phys.* **73**, 1993.
37. McCall, S. L., *Appl. Phys. Lett.* **32**, 284 (1978).
38. H. Ito, Y. Ogawa, and H. Inaba, *Electron. Lett.* **16**, 593 (1980).

39. Y. Okada, *Opt. Comm.* **34**, 153 (1980).
40. Y. Okada, *Proceedings of the Sixth European Conference on Optical Communication* (IEE, London, England), 246 (1980).
41. Y. Okada, *IEEE J. Quantum Electron.* **QE-16**, 770 (1980).
42. Sohler, W., *Appl. Phys. Lett.* **36**, 351 (1980).
43. H. M. Gibbs, J. L. Jewell, S. S. Tarng, A. C. Gossard, and W. Wiegmann, *IEEE J. Quantum Electron.* **QE-17**, 42 (1981).
44. J. L. Jewell, H. M. Gibbs, S. S. Tarng, A. C. Gossard, and W. Wiegmann, *Appl. Phys. Lett.* **40**, 291 (1982).
45. N. N. Rozanov, *Zh. Eksp. Teor. Fiz.* **80**, 96-108 (1981).
46. L. L. Golik, A. V. Grigor'yants, M. I. Elinson, and Yu. I. Balkarei, *Opt. Comm.* **46**, 51-56 (1983).
47. N. N. Rosanov, A. V. Fedorov, and G. V. Khodova, *Phys. Stat. Sol. (b)* **150**, 545-555 (1988).
48. Yu. I. Balkarei, A. V. Grigor'yants, and Yu. A. Rzhanov, *Sov. J. Quantum Electron.* **17**, 72-75 (1987).
49. Yu. A. Rzhanov and Yu. D. Kalafati, *Opt. Comm.* **70**, 161-165 (1989).
50. J. I. Pankove, *Optical Processes in Semiconductors*, Dover Publishers, Inc., New York, 1971.
51. K. W. Böer, *Survey of Semiconductor Physics*, Van Nostrand Reinhold, New York, 1990.
52. E. F. Steigmeier and B. Abeles, *Phys. Rev. A* **136**, 1149 (1964).
53. G. A. Slack, *Solid State Physics* **34**, edited by F. Seitz, D. Turnbull, and H. Ehrenreich, Academic Press, New York (1979).
54. J. W. Vandersande and C. Wood, *Contemp. Phys.* **27**, 117-144 (1986)
55. J. H. Marburger, *Prog. Quantum. Electron.* **4**, 35-110 (1975)
56. S. A. Akhmanov, R. V. Khokhlov, and A. P. Sukhorukov, *Laser Handbook*, F. T. Arecchi and E. O. Shulz-Dubois, eds. (North-Holland, Amsterdam, 1972), Chap. E3, pp. 1151-1228.
57. A. Feldman, D. Horowitz, and R. M. Waxler, *IEEE J. Quantum Electron.* **QE-9**, 1054-1061 (1973).



58. A. Feldman, D. Horowitz, and R. M. Waxler, *Appl. Phys. Lett.* **21**, 260-262 (1972).
59. Uy. P. Raizer, *J. Exp. Theor. Phys. (USSR)* **52**, 470-482 (1967).
60. R.Y. Chiao, E. Garmire, and C.H. Townes, *Phys. Rev. Lett.* **13**, 479-482 (1964).
61. E. L. Kerr, *Phys. Rev. A* **4**, (1971).
62. F.W. Dabby and J.R. Whinnery, *Appl. Phys. Lett.* **13**, 284-286 (1968).
63. Frederic M. Durville and Richard C. Powell, *Opt. Soc. Amer. B* **4**, 1934-1937 (1987).
64. J.D. Foster and L.M. Oserink, *J. Appl. Phys.* **41**, 3656-3663 (1970).
65. G.M. Zverev, E.A. Levchuk, E.K. Maldutis, and V.A. Pashkov, *Sov. Phys. JETP Lett.* **11**, 108-111 (1970).
66. Walter Koechner, *Solid State Laser Engineering* (Springer-Verlag, Berlin, 1988), Chap. 7, pp.350-401.
67. G.M. Zverev and V.A. Pashkov, *Sov. Phys. JETP* **30**, 616-621 (1970).
68. E.P. Riedel and G.D. Baldwin, *J. Appl. Phys.* **38**, 2720-2725 (1967).
69. G.D. Baldwin and E.P. Riedel, *J. Appl. Phys.* **38**, 2726-2737 (1967).
70. B. Taheri, A. Munoz F., W.D. St.John, J.P. Wicksted, R.C. Powell, D.H.Blackburn, and D.C. Cranmer, *J. Appl. Phys.* **71**, 3693-3700 (1992).
71. Amnon Yariv, *Quantum Electronics*, 3rd ed. (Wiley, New York, 1989), Chap. 6, pp. 106-135.
72. A.L. Dyshko, V.N. Lugovoi, and A.M. Prokhorov, *Sov. Phys. JETP* **34**, 1235-1241 (1972).
73. A.P. Dyshko, V.N. Lugovoi, and A.M. Prokhorov, *Sov. Phys. JETP Lett.* **6**, 146-149 (1967).
74. W.G. Wagner, H.A. Haus, and J.H. Marburger, *Phys. Rev.* **175**, 256-266 (1968).
75. Javier Alda and Glenn D. Boreman, *Appl. Opt.* **29**, 2944-2950 (1990).
76. David Metcalf, Pascal de giovanni, Jerzy Zachorowski, and Michele Leduc, *Appl. Opt.* **26**, 4508-4517 (1987).

77. M. Sheik-bahae, A. A. Said, D. J. Hagan, M. J. Soileau, and E. W. VanStryland, *Opt. Eng.* **30**, 1228-1235 (1991).
78. H.W. Wyld, *Mathematical Methods for Physics* (Benjamin/Cummings, Menlo Park, Calif., 1976), pp.319-326.
79. Herwig Kogelnik, *Appl. Opt.* **4**, 1562-1568 (1965).
80. 0 and z are more precisely z and z+z, where z is some small iteration in z.
81. W. D. St.John, B. Taheri, J. P. Wicksted, and R. C. Powell, *J. Opt. Soc. Am. B* **9**, 610-616 (1992).
82. C. Spiegelberg, J. Puls, and F. Henneberger, *Physica Status Solidi B* **159**, 353-361 (1990).
83. M. Wegener, C. Klingshirn, S. Koch, and L. Banyai, *Semiconductor Science and Technology* **1**, 366-375 (1986).
84. P. Peterson, *Opt. Eng.* **27**, 234-237 (1988).
85. J. Grohs, *Proc. SPIE 1127-Nonlinear Optical Materials II*, 39-48 (1989).
86. O. Madelung, M. Schult, and H. Weiss, eds., *Landolt-Börnstein Series III 17b*, Springer-Verlag, New York, 194-204 (1982).
87. H. Haug and S. W. Koch, *Quantum Theory of the Optical and Electronic Properties of Semiconductors*, World Scientific Publishing Co., Pte. Ltd., N.J. (1990).

## APPENDICES

## APPENDIX A

### PROGRAM FOR THEORY II.A., CHAPTER II

```
real *8 n0,hnewt,kth,l0,lam,kb,knot,taun,hw,  
laplzt,laplrt,intold,laprr,lapri,laplzn,laplrn,  
nehmax, 2 dtemp(50,700),alpha(50,700),elec(50,700),  
nnot, eleci(50,700),intens(50,700),tnew(50,700),  
neh(50,700)  
open(unit=1,file='data1.dat',status='new')  
open(unit=2,file='data2.dat',status='new')  
iwrite=0  
iss=2  
da=1.e-4  
jcool=0  
n0=2.8  
pin=.64  
dndt=9.e-6  
taun=40.e-9  
jjmax=0  
nehmax=0.  
310 format(1x,e15.3,1x,i1)  
diff=8.e-6  
hnewt=10.  
qeffmin=1./12.  
kth = 6.  
l0 = .001  
pi = 3.14  
alphath=7.e-6  
ao = 293.  
sig = 2.108  
eb = 2.61  
hw=2.61*1.6e-19  
ego = 2.67  
ex = .0644  
dedt = -.0008519  
kb = 1.38E-23 / 1.6E-19  
temp0 = 290.  
alpham = 5.e6
```

```

w01=1.7e-3
lam=476.5e-9
knot=2.*pi/lam
focal=.05
z01=pi*w01**2/lam
zsamp=focal-.17*.001
rad=((1.-zsamp/focal)**2+(zsamp/z01)**2)/,
(-1./n0/focal+zsamp/n0*(1./focal**2+1./z01**2))
w1=sqrt(lam/pi*((1.-zsamp/focal)**2+(zsamp/z01)**2)*n0*z01),
xintens=2.*pin/pi/w1**2
dr=3.e-6
imax=12
dz=.5/4.*dr**2*knot
jmax=10/dz
dxsq=1./(1./dz**2+1./dr**2)
if(iss.eq.1)then
dt=1./4./diff/(1./dr**2+1./dz**2)
else
dt=.8*taun
endif
print *,'dt=',dt*1e6,'usec dz=',dz*1e6,'um jmax=',jmax
do 300 tinit=-50.*dt,-dt,dt
write(1,310)tinit*1.e6,0
300 continue
kmax=1e6
alpha0=ao*exp(sig/kb/temp0*(eb+ex-ego))
do 71 j=1,jmax
do 72 i=1,imax
alpha(i,j)=alpha0
dtemp(i,j)=.0
tnew(i,j)=0.
neh(i,j)=0.
72 continue
71 continue
print *,'input waist=',w1
xi=2.*zsamp/knot/w01**2
gam=1.-zsamp/focal
x=gam/xi
enot=2./w01*sqrt(377.*pin/pi)
kkk=0
do 20 k=1,kmax
time=(k-1)*dt
pout=0
t=(k-1)*dt
kkk=kkk+1

```

```

do 30 j=1,jmax
if(j.eq.1)then
do 40 i=1,imax
r=(i-1)*dr
tpsi=2./sqrt((n0+1.)**2+(alpha(i,j)/2./knot)**2)
tphas=atan(alpha(i,j)/2./(n0+1.)/knot)
theta=r/w01
phas=-theta**2/xi-pi/2.+theta**2*x/xi**2/ 1 (1.+x**2)**1.5-atan(x)
psi=enot/xi/(1.+x**2)*exp(-theta**2/xi**2/ 1 (1.+x**2)**1.5)*tpsi
elec(i,1)=psi*cos(phas)
eleci(i,1)=psi*sin(phas)
intens(i,1)=psi**2/377.*n0
40 continue
endif
do 50 i=1,imax r=(i-1)*dr
if(k.eq.1)then
goto 111
else
if(i.eq.1)then
laplrm=4./dr**2*(neh(i+1,j)-neh(i,j))
laplrm=4./dr**2*(dtemp(i+1,j)-dtemp(i,j)) else
laplrm=(neh(i+1,j)+neh(i-1,j)-2.*neh(i,j))/dr**2+
1 1./(2.*r*dr)*(neh(i+1,j)-neh(i-1,j))
laplrm=(dtemp(i+1,j)+dtemp(i-1,j)-2.*dtemp(i,j))/dr**2+,
1./(2.*r*dr)*(dtemp(i+1,j)-dtemp(i-1,j))
endif
if(j.eq.1)then
laplzn=(neh(i,j+1)-neh(i,j))/dz**2
laplzt=(dtemp(i,j+1)-dtemp(i,j))/dz**2-hnewt*dtemp(i,j)/dz/kth else
laplzn=(neh(i,j+1)+neh(i,j-1)-2.*neh(i,j))/dz**2
laplzt=(dtemp(i,j+1)+dtemp(i,j-1)-2.*dtemp(i,j))/dz**2
endif
if(j.eq.jmax)then
laplzn=(neh(i,j-1)-neh(i,j))/dz**2
laplzt=(dtemp(i,j-1)-dtemp(i,j))/dz**2-hnewt*dtemp(i,j)/dz/kth
endif
if(j.eq.jcool)then
qeff=qeffmin
else
qeff=1.
endif
neh(i,j)=1./(1.+dt/taun)*(neh(i,j)+1.e-10*da*dt*(
1 laplrm+laplzn)+alpha(i,j)*intens(i,j)*dt/hw*1.e-10)
if(neh(i,j).gt.nehmax)then
iimax=i

```

```

jjmax=j
nehmax=neh(i,j)
endif
if(iss.eq.2)then
qt=neh(i,j)*eb*1.6e-19/taun/kth*1.e10
else
qt=qeff*alpha(i,j)*intens(i,j)/kth
endif
tnew(i,j)=dtemp(i,j)+dt*diff*(qt+laplzt+laplrt)
alpha(i,j)=ao*exp(sig/kb/(temp0+tnew(i,j))*
(eb+ex-ego-dedt*tnew(i,j)))
if(alpha(i,j).gt.alpham)then
alpha(i,j)=alpham
endif
111 endif
50 continue
30 continue
do 51 j=1,jmax
do 31 i=1,imax
dtemp(i,j)=tnew(i,j)
phi=knot*dz*dndt*dtemp(i,j)
if(i.eq.1)then
laprr=(elec(i+1,j)+elec(2,j)-2*elec(i,j))/dr**2
lapri=(elec(i+1,j)+elec(2,j)-2*elec(i,j))/dr**2
else
laprr=(elec(i+1,j)+elec(i-1,j)-2*elec(i,j))/dr**2+
1./r*(elec(i+1,j)-elec(i-1,j))/2./dr,
lapri=(elec(i+1,j)+elec(i-1,j)-2*elec(i,j))/dr**2+
1./r*(elec(i+1,j)-elec(i-1,j))/2./dr
endif
if(j.eq.1)then
elec(i,j+1)=elec(i,j)+dz/knot/n0/2.*lapri
elec(i,j+1)=elec(i,j)-dz/knot/n0/2.*laprr
else
elec(i,j+1)=elec(i,j-1)+dz/knot/n0*lapri
elec(i,j+1)=elec(i,j-1)-dz/knot/n0*laprr
endif
ab=exp(-.5*alpha(i,j)*dz)
elec(i,j+1)=(elec(i,j+1)*cos(phi)+elec(i,j+1)*sin(phi))*ab
elec(i,j+1)=(elec(i,j+1)*cos(phi)-elec(i,j+1)*sin(phi))*ab
intens(i,j+1)=(elec(i,j+1)**2+elec(i,j+1)**2)/377.*n0
31 continue
51 continue
do 52 i=1,imax
r=(i-1)*dr

```

```

pout=pout+pi*(intens(i,j)*r+intens(i+1,j)*(r+dr))*dr
52 continue
if(k.eq.1 .and. iwrite.eq.1)then
do 62 j=1,jmax+1,(jmax+1)/10
do 63 i=1,2*imax-1 ic=-imax+i
do 61 ism=1,2
if(ic.lt.1)then
if(ism.eq.1)then
write(2,911) ism+ic*2-2,(j-1)*dz/10,intens(-ic+2,j)
write(1,911) ism+ic*2-2,(j-1)*dz/10,dtemp(-ic+2,j)
else
write(2,911) ism*ic,(j-1)*dz/10,.5*(intens(-ic+2,j)+
1 intens(-ic+1,j))
write(1,911) ism*ic,(j-1)*dz/10,.5*(dtemp(-ic+2,j)+ * 1 dtemp(-ic+1,j))
endif
endif
else
if(ism.eq.1)then
write(2,911) ism+ic*2-2,(j-1)*dz/10,intens(ic,j)
write(1,911) ism+ic*2-2,(j-1)*dz/10,dtemp(ic,j)
else
write(2,911) ism*ic,(j-1)*dz/10,.5*(intens(ic,j)+
1 intens(ic+1,j))
write(1,911) ism*ic,(j-1)*dz/10,.5*(dtemp(ic,j)+ * 1 dtemp(ic+1,j))
endif
endif
endif
61 continue
63 continue
62 continue
endif
911 format(1x,i4,1x,e15.6,1x,e15.6)
912 format(1x,i3,1x,e15.6)
if(k.eq.1)then pold = pout
endif
tran= pout/pold
if(kkk.gt.1.e-6/dt .or. k.eq.1)then
kkk=0
slope=tran-tranold
tranold=tran
if(t.gt.1.e-3)then
goto 366
endif
write(1,200) time*1.e6,tran
200 format(1x,e15.6,1x,e15.6)
endif
20 continue

```



```
366 print *,'  
stop  
end
```

## APPENDIX B

### PROGRAM FOR THEORY II.B., CHAPTER II

```
real mo,me,mh,mr,kb,ne,nh,lambda,k1,k2,k3,k4,k5,
lam(100),alph(100),deln(100)
open(unit=1,file='data1.dat',status='new')
dgamn=2.5e-24
dedt=-7.5e-4
nmaxb=1000
nmaxc=4000
h=6.63E-34/1.6E-19
mo=9.11E-31
me=0.16*mo
mh=.6*mo
mr=1/(1/me+1/mh)
pi=3.14159
kb=1.38e-23/1.6e-19
etilda=me/mr
htilda=mh/mr
er=0.015
k1=4.8966851
k2=3.3105795
k3=73.6264033
k4=.133376
k5=-21.0508644
delt=0
ego=2.70+dedt*delt
temp=290+delt
ne=1.e21
nh=ne
ttilda=kb*temp/er
ao=44e-10
constie=4*ne*ao**3*(pi/ttilda/etilda)**1.5
constih=4*nh*ao**3*(pi/ttilda/htilda)**1.5
uetild=log(constie)+k1*log(k2*constie+k3)+k4*constie+k5
uhtild=log(constih)+k1*log(k2*constih+k3)+k4*constih+k5
ue=uetild*kb*temp+ego/2
uh=uhtild*kb*temp+ego/2
gam=er*(1.+dgamn*ne)
```

```

gamtil=gam/er
i=0
do 400 lambda=500,450,-1
i=i+1
lam(i)=lambda
call gsub(g,uetild,uhtild,etilda,htilda,ttilda,pi,ao)
if(g.lt.1)then
deg=-er/g
else
deg=er*((1-1/g)**2-1)
endif
eg=ego+deg
uetild=(ue-eg/2)/kb/temp
uhtild=(uh-eg/2)/kb/temp
wtildo=(h*3.e8/(lambda*1.e-9)-ego)/er
wtild=(er*wtildo-deg)/er
w=1/h*2*pi*(eg+wtild*er)
if(g.lt.1)then
bw=0.0
else
call bwsub(bw,nmaxb,g,wtild,gamtil)
endif
call cwsub(cw,nmaxc,g,wtild,pi,gamtil)
arg=.5*(wtild/ttilda-uetild-uhtild)
alpha=49.87e-15*w/er*TANH(arg)*(bw+cw)
alph(i)=alpha
print *,'lambda=',lambda,'a=',alpha
write (1,300) lambda,alpha
300 format(1x,e15.6,1x,e15.6)
400 continue
imax=i
do 660 i=1,imax
pvint=0
do 661 j=1,imax
if(j.eq.i)then
goto 661
endif
pvint=pvint+(alph(j)-alph(1))/((lam(j)/lam(i))**2-1)*1e-9
661 continue
deln(i)=pvint/2/pi**2 write(1,666) lam(i),alph(i),deln(i)
print *,'lam=',lam(i),'alpha=',alph(i),'deln=',deln(i)
660 continue
666 format(1x,e15.6,1x,e15.6,1x,e15.6)
stop
end

```

```

subroutine bwsub(bw,nmaxb,g,wtild,gamtil)
bw=0.0
do 1200 l=1,int(sqrt(g))
conlg=2*(g-l**2)*(2*l**2-g)/l**3/g**2
prod=1.0
do 800 n=1,nmaxb
if(n.eq.l)then
goto 800
endif
prodold=prod
prod=prod*n**2*(n**2*l**2-(g-l**2)**2)/(n**2-l**2)/,
(n**2*l**2-g**2)
800 continue
bw=bw+1/gamtil/cosh((wtild+(1/l-l/g)**2)/gamtil)*prod*conlg
1200 continue
return
end
subroutine cwsub(cw,nmaxc,g,wtild,pi,gamtil)
real int1,int2
cw=0.0
xmax=40.0
dx=0.02
do 1400 x=0.0,xmax,dx
prod1=1.0
prod2=1.0
do 2000 n=1,nmaxc
pold1=prod1 pold2=prod2
prod1=prod1*(1+(2*g*n**2-g**2)/((n**2-g)**2+n**2*g**2*x))
prod2=prod2*(1+(2*g*n**2-g**2)/((n**2-g)**2+n**2*g**2*(x+dx)))
2000 continue
2001 int1=sqrt(x)*prod1/(pi*gamtil*cosh((x-wtild)/gamtil))
int2=sqrt(x+dx)*prod2/(pi*gamtil*cosh((x+dx-wtild)/gamtil)) cwold=cw
cw=cw+.5*dx*(int1+int2)
1400 continue
1402 return
end
subroutine gsub(g,uetild,uhtild,etilda,htilda,ttilda,pi,ao)
real intg1,intg2,intg,intold
xmax=50
dx=.02
intg=0.0
do 2200 x=0.0,xmax,dx
x1=x
x2=x+dx
fex1=1/(1+exp(x1-uetild))

```

```
fhx1=1/(1+exp(x1-uhild))
fex2=1/(1+exp(x2-uetild))
fhx2=1/(1+exp(x2-uhild))
intg1=sqrt(x1)*(etilda**1.5*fex1*(1-fex1)+htilda**1.5*fhx1*(1-fhx1))
intg2=sqrt(x2)*(etilda**1.5*fex2*(1-fex2)+htilda**1.5*fhx2*(1-fhx2))
intold=intg
intg=intg+.5*dx*(intg1+intg2)
2200 continue
2201 screen=sqrt(1/ao**2*4/pi*sqrt(ttilda)*intg)
g=12/pi**2/ao/screen
return
end
```

VITA 

W. DOYLE ST. JOHN

Candidate for the Degree of

Doctor of Philosophy

Thesis: NONLINEAR TRANSMISSION STUDIES IN GLASSES AND SEMI-  
CONDUCTORS OF THERMAL AND ELECTRONIC ORIGIN

Major Field: Physics

Biographical:

Personal Data: Born in Austin, Texas, February 17, 1964, the son of Bill and Virginia St. John.

Education: Received Bachelor of Science Degree in Electrical Engineering from Tulsa University, Tulsa, Oklahoma, 1986; received Master of science Degree in Electrical Engineering from Oklahoma State University, Stillwater, Oklahoma, 1988; completed requirements for the Doctor of Philosophy Degree in Physics at Oklahoma State University, Stillwater, Oklahoma in May, 1993.